

Advances in Ionic Thermoelectrics: From Materials to Devices

Shuai Sun, Meng Li, Xiao-Lei Shi,* and Zhi-Gang Chen*

As an extended member of the thermoelectric family, ionic thermoelectrics (i-TEs) exhibit exceptional Seebeck coefficients and applicable power factors, and as a result have triggered intensive interest as a promising energy conversion technique to harvest and exploit low-grade waste heat (<130 °C). The last decade has witnessed great progress in i-TE materials and devices; however, there are ongoing disputes about the inherent fundamentals and working mechanisms of i-TEs, and a comprehensive overview of this field is required urgently. In this review, the prominent i-TE effects, which set the ground for i-TE materials, or more precisely, thermo-electrochemical systems, are first elaborated. Then, TE performance, capacitance capability, and mechanical properties of such system-based i-TE materials, followed by a critical discussion on how to manipulate these factors toward a higher figure-of-merit, are examined. After that, the prevalent molding methods for assembling i-TE materials into applicable devices are summarized. To conclude, several evaluation criteria for i-TE devices are proposed to quantitatively illustrate the promise of practical applications. It is therefore clarified that, if the recent trend of developing i-TEs can continue, the waste heat recycling landscape will be significantly altered.

technology, which can literally convert ambient heat into high value-added electricity.^[2] Compared to its analogous heat-to-electricity technologies, TE takes the advantage of light weight, quietness, zero pollution emission, and an infinite lifetime (Figure 1b), making it ideal for self-powering applications that are equipped on human body or installed in rural areas.^[3] The performance of TE devices is mainly governed by the dimensionless figure-of-merit of their constituent TE materials, defined as $ZT = S^2\sigma T/\kappa$, where T refers to absolute temperature, S , σ , and κ are the Seebeck coefficient, electrical conductivity, and thermal conductivity, respectively.^[4] Practically, “ Z ” reflects the premise of TE materials being used for power generation, namely as a thermoelectric generator, while “ T ” regulates the working temperature under which heat transfer is valid.^[5] As can be seen in Figure 1c, TE materials with high

1. Introduction

Due to relentless exhaustion of fossil fuels and more frequent climate disasters than ever before, human society has been facing with unprecedented energy crisis since stepping into the 21st century. This has drawn tremendous attention from both academia and industries on energy conversion techniques, which can produce electric energy from exploiting renewable power sources, as shown in Figure 1a.^[1] Recently, increasing interest has been focused on thermoelectric (TE)

heat transfer property and a Z of $>10^{-3} \text{ K}^{-1}$ (corresponds to $ZT > 0.3$ at room temperature) are suitable for making temperature sensors; in comparison, TE materials with a much higher Z of 10^{-2} K^{-1} (corresponds to $ZT > 3$ at room temperature) and low heat transfer property are preferable for making wearable devices.

On the attainment of satisfactory Z value, a large S , which is proportional to the magnitude of thermovoltage per temperature difference (ΔT), is highly desirable. However, the S of conventional electronic thermoelectric (e-TE) materials is limited to an order of 10^1 – $10^2 \mu\text{V K}^{-1}$ due to relatively low electronic enthalpy of inorganic materials, i.e., the S of electron gas is merely $\approx 87.5 \mu\text{V K}^{-1}$ at room temperature.^[6] Considering a small ΔT of 20 °C as that between human skin and ambient environment, more than 100 inorganic TE legs are required to work comparably with a 1.5 V solid battery via calculation, which indicates that e-TE materials are unsuitable for low-grade (<130 °C) applications. As most of waste heat is emitted from low-grade sources such as industrial plants and vehicle exhaust, traditional e-TE devices are in niche market. As another form of charge carrier, ions can induce a much larger S in an order of a few mV K^{-1} due to higher ionic enthalpy than electronic enthalpy.^[7] As a result, an ionic thermoelectric (i-TE) device needs only ≈ 8 legs to generate a 1.5 V voltage at a ΔT of 20 °C, indicating that i-TE device is feasible for microminiaturization and can be incorporated with wearable devices and electronic skins. Other advantages of i-TEs over e-TEs include i) good flexibility stemming from the normally organic matrix,

S. Sun, Z.-G. Chen
Centre for Future Materials
University of Southern Queensland
Springfield Central, Queensland 4300, Australia
E-mail: zhigang.chen@usq.edu.au

M. Li, X.-L. Shi, Z.-G. Chen
School of Chemistry and Physics
Queensland University of Technology
Brisbane, QLD 4000, Australia
E-mail: xiaolei.shi@qut.edu.au

 The ORCID identification number(s) for the author(s) of this article can be found under <https://doi.org/10.1002/aenm.202203692>.

© 2023 The Authors. Advanced Energy Materials published by Wiley-VCH GmbH. This is an open access article under the terms of the Creative Commons Attribution-NonCommercial-NoDerivs License, which permits use and distribution in any medium, provided the original work is properly cited, the use is non-commercial and no modifications or adaptations are made.

DOI: 10.1002/aenm.202203692

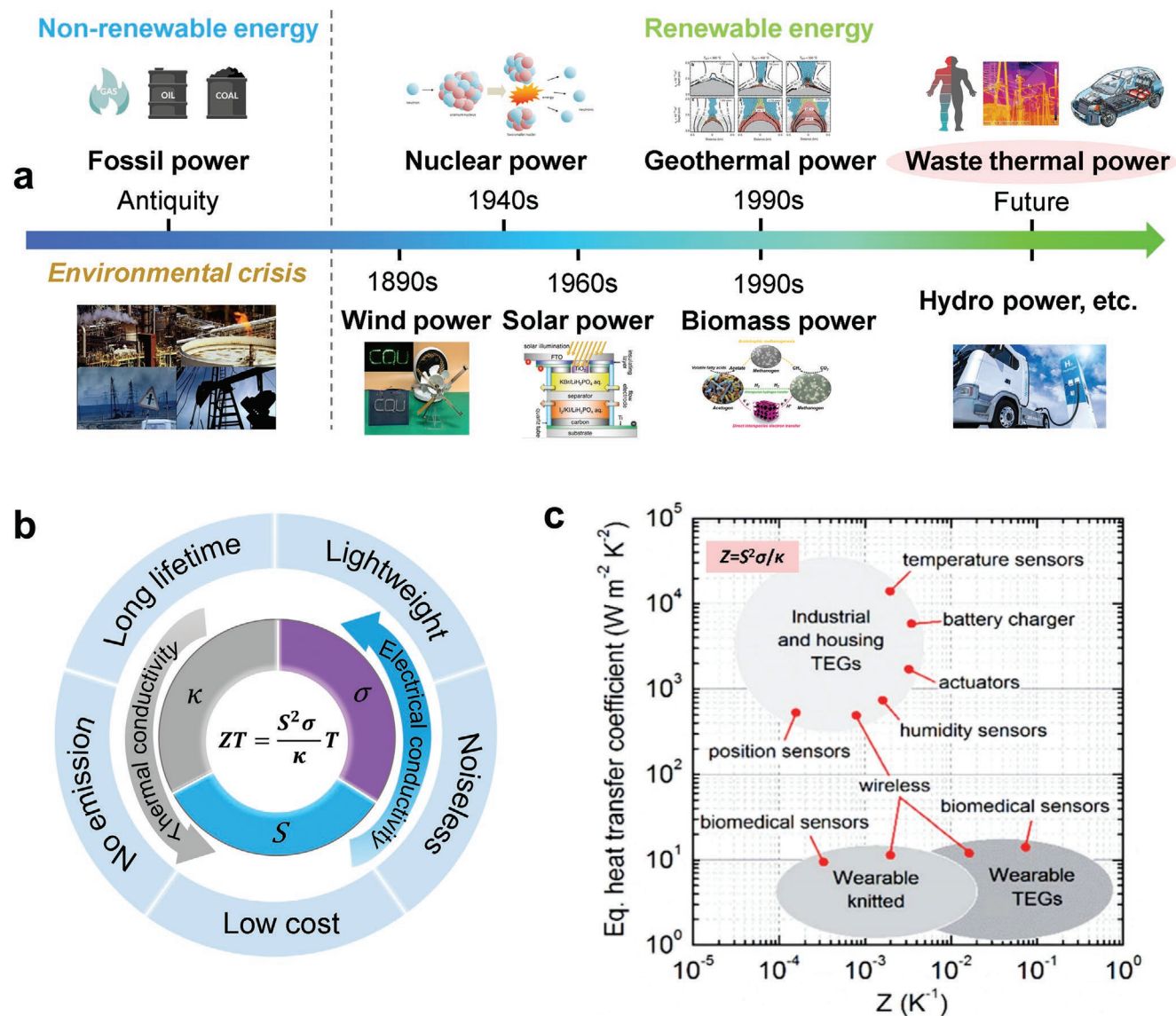


Figure 1. a) Evolution of energy utilization in industrialization process. Reproduced with permission.^[8] Copyright 2015, Springer Nature. Reproduced with permission.^[9] Copyright 2019, Elsevier. Reproduced with permission.^[1a] Copyright 2020, Springer Nature. Reproduced with permission.^[10] Copyright 2018, American Chemical Society. b) Superiorities and terminologies of thermoelectrics. c) Roadmap toward applications of TE devices. Reproduced with permission.^[5] Copyright 2017, Royal Society of Chemistry.

ii) scalability due to facile fabrication process, and iii) low-cost and earth-abundance of raw materials.

Benefited from the colossal S which is reckoned as the most prominent parameter of TE materials, i-TE systems have been continuously developed. In the pioneering stage of i-TEs, material systems are focused on ionic solutions, including aqueous of acid (e.g., HNO_3),^[11] base (e.g., NaOH),^[12] salt (e.g., LiCl),^[13] and ionic liquids (ILs) (e.g., 1-ethyl-3-methylimidazolium dicyanamide ([EMIM:DCA])).^[14] As the i-TE technology steps forward for decades, diverse ongoing i-TE systems have been designed for acquiring exceptional S , e.g., 2.2 mV K^{-1} in redox liquid electrolytes,^[15] 19 mV K^{-1} in solid polyelectrolytes,^[16] -7.7 mV K^{-1} in n-type polymers,^[17] 16.2 mV K^{-1} in p-type polymers,^[18] 25.4 mV K^{-1} in polymer ionogels,^[19] 14.8 mV K^{-1} in

nanoparticle ionogels,^[20] 17 mV K^{-1} in IL embedded gelatins,^[21] 24 mV K^{-1} in IL embedded celluloses,^[12] and -18 mV K^{-1} in electronic/ionic combined systems.^[22] There is also a trend of structure optimization for increasing S , which will be discussed in detail later.

Such progressive and short-term developments, however, have also led to controversies surrounding the understanding of the underlying mechanisms of i-TE materials and specified applications of i-TE devices, making future i-TE research far beyond simply envisaging for a higher S or ZT . This is the motivation behind this review, which is divided into six sections. In Section 2, the fundamentals and related theories are elucidated. In Section 3, the composition, physical state, and charge carrier feature of i-TE materials are summarized. In Section 4, the

key properties of i-TE materials are overviewed, including TE performance, capacitance capability, and mechanical flexibility. In Section 5, the factors influencing TE performance and optimization approaches are discussed. In Section 6, the existing molding methods to make i-TE materials into feasible devices are iterated. In Section 7, the design strategies and practical performance of i-TE devices are examined. Perspective remarks on the outlook and challenges of this field are provided in the end. Interested readers are also referred to other reviews of thermoelectrochemistry.^[23]

2. Ionic Thermoelectric Mechanisms

In this section, we explain the fundamental thermodiffusion and thermogalvanic effects, which result in i-TE phenomenon. To understand how i-TE effects can generate electric potential

difference, several phenomenological models are examined. Heat transfer principles of i-TE materials are discussed from the perspective of the latest progress. Some existing disputes about i-TE conversion are presented as an open point of view in the end.

2.1. Fundamental Effects

Despite that both e-TE and i-TE materials can be functionalized to convert heat into electricity, their mechanisms are different. As shown in Figure 2a, in e-TE materials, electrons (holes) as charge carriers are driven by an electromotive force under an applied ΔT , which is known as the Seebeck effect.^[24] Electrons in higher energy state populates from hot side to cold side, generating an electric potential difference along the opposite direction to temperature gradient, given the negative

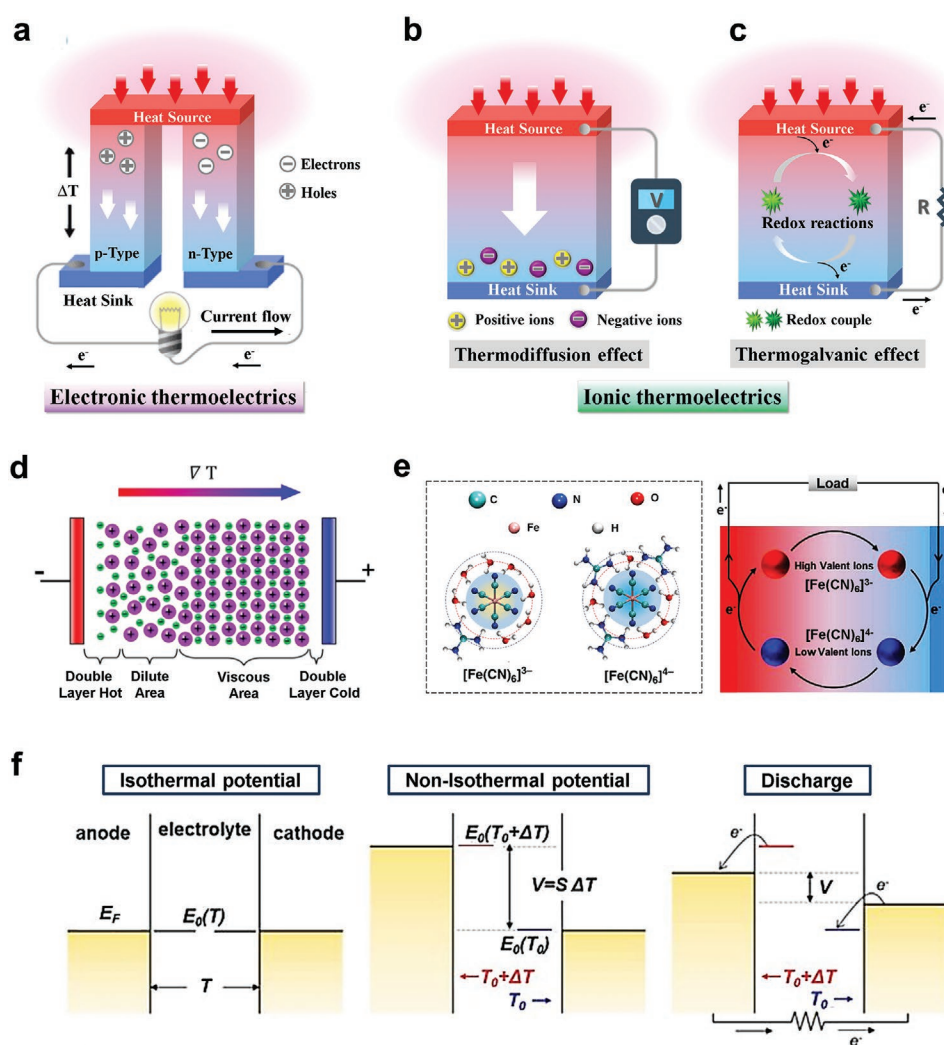


Figure 2. Schematic diagram of a) a group of p-type and n-type electronic thermoelectric (e-TE) materials, b) a thermodiffusive ionic thermoelectric (i-TE) material, and c) a thermogalvanic i-TE material. d) Internal structure of a thermodiffusive i-TE material in working mode. Reproduced with permission.^[29] Copyright 2021, Wiley-VCH. e) Coordination structure and working mechanism of $\text{Fe}(\text{CN})_6^{3-}/\text{Fe}(\text{CN})_6^{4-}$ redox couple working in i-TEs. Reproduced with permission.^[34] Copyright 2018, Springer Nature. f) The electric potential evolution in a thermogalvanic i-TE material. Reproduced with permission.^[35] Copyright 2017, Elsevier.

sign of electrons. Whereas for i-TE materials, the generation of electric potential is rooted in two distinguished origins: thermodiffusion effect^[25] and thermogalvanic effect,^[26] as shown in Figure 2b,c.

2.1.1. Thermodiffusion Effect

Thermodiffusion effect derives from the Soret effect, which was first observed by Soret and Ludwig in the 19th century.^[27] As illustrated in Figure 2b, in a thermodiffusive i-TE material subjected to a ΔT , the ion concentration is different at two electrode surfaces because of migration of ions from hot side to cold side. Considering the electronic neutrality, cationic and anionic ions coexist in i-TE materials. However, ions are normally featured with different migration speed (diffusion rate) due to distinctive size, activation energy and Coulomb force.^[27] The dissimilar diffusion rate between cations and anions result in an imbalance of their respective ion concentration. According to the Gouy–Chapman–Stern theory, a double-layer area near the electrolyte/electrode interface will be formed, which consists of a Helmholtz layer and a diffusion layer, as illustrated in Figure 2d.^[28] The ion concentration difference induces a viscous area near one electrode and a dilute area near the other, which can generate different chemical potential in their respective Helmholtz layers.^[29] The chemical potential difference between two Helmholtz layers conversely triggers an electric potential difference between two electrodes.

I-TE materials based on the Soret effect are in analogy to e-TE materials based on the Seebeck effect, because both can generate a thermovoltage related to charger transfer enthalpy.^[30] However, there are several apparent differences. i) An electron carries only unit charge, while an ion can carry much more charge depending on its overall valence state. ii) The transport of electrons should obey Fermi–Dirac statistical functional which is restricted within a small energy window,^[31] while the transport of ions does not. iii) Electrons as major carriers contribute to electrical conductance solely in e-TE materials, while cations and anions exist simultaneously in i-TE materials; and most importantly. iv) Electrons can be cycled through external circuit, but ions agglomerate at electrodes, therefore, in i-TE materials, convection of electrolytes or connecting to capacitor are needed.^[32]

2.1.2. Thermogalvanic Effect

The thermogalvanic effect is the second fundamental i-TE effect, which is defined based on thermally driven redox reactions,^[33] as shown in Figure 2c. It can be seen that a thermogalvanic i-TE material contains at least one redox couples, which are oxidized at anode and reduced at cathode. The inclusive redox reaction can be expressed as $Ox + ne^- \rightleftharpoons Red$, with a reaction rate related to local temperature. Figure 2e illustrates the internal structure of an i-TE material working based on the thermogalvanic effect, with assuming that hot electrode is cathode and cold electrode is anode. When a ΔT is applied, continuous redox reactions endow hot and cold electrodes with dissimilar chemical potential, leading to an electric potential difference.

Notably, unlike e-TE materials or thermodiffusive i-TE materials, enthalpy changes discontinuously in thermogalvanic i-TE materials, so the magnitude of generated thermovoltage is solely determined by redox couple species. For instance, as shown in Figure 2e, $Fe(CN_6)^{3-}/Fe(CN_6)^{4-}$ based i-TE materials normally exhibit an S larger than 2 mV K^{-1} arising from the huge Eastman entropy due to resonant valence state of $Fe(CN_6)$ ions.^[34] Figure 2f schematically illustrates the chemical potential evolution in a thermogalvanic process. In which, thermogalvanic i-TE material is under an isothermal state, and the anode and cathode possess a balanced electric potential (E_0). Upon heating one of the electrodes, the equilibrium is destroyed, and the correspondent electric potential increases if an oxidation reaction occurs, or vice versa. After this system is connected to an external load, namely in a discharge process, electrons flow from anode to cathode through external circuit to balance electric potential difference.^[35]

2.2. Ionic Transport Characteristics

In most cases, i-TE materials can be seen as a colloidal suspension, which means the thermodiffusion behavior of ions cannot be merely described by the Brownian motion theory.^[36] Instead, colloid-based theories are adopted afterward, which is more appropriate for analyzing the kinetics and dynamics of i-TEs.^[23a]

2.2.1. Ion Transport with No External Force^[37]

Thermoelectric effects are basically carrier transport phenomena, the underlying transport fundamental is critically associated with S . In principle, the ion diffusion process occurs in every nonequilibrium moment with the appearance of dissipation. Onsager's theory was first used to describe the irreversible ion transport with a formal skeleton in 1931.^[38] With approximations, the ion flux density of a specific ion source is

$$J = -\mu k_B T \cdot \nabla c - c \mu Q^* \cdot \frac{\nabla T}{T} \quad (1)$$

where the first term refers to mass diffusion (Fick's law) and the second term refers to thermophoresis (Onsager cross-coupling),^[32a] Q^* is the "heat of transport", μ is ion mobility, and c is ion concentration.

However, the quantitative analysis of a nonequilibrium system is difficult. Assumption of equilibrium condition is usually needed to deal with ion transfer, as shown in Figure 3a. In this way, Equation (1) can be rewritten as^[39]

$$\begin{aligned} J &= J_D + J_T \\ &= -D \cdot \nabla c - D_T c \cdot \nabla T \\ &= -D \cdot \nabla c - Q^* \frac{D}{2k_B T^2} \left[1 + \left(\frac{\partial \ln \gamma_{a\pm}}{\partial \ln m} \right)_T \right]^{-1} c \cdot \nabla T \end{aligned} \quad (2)$$

where D is the Brownian motion coefficient, and D_T is the thermodiffusion coefficient. The first and second terms

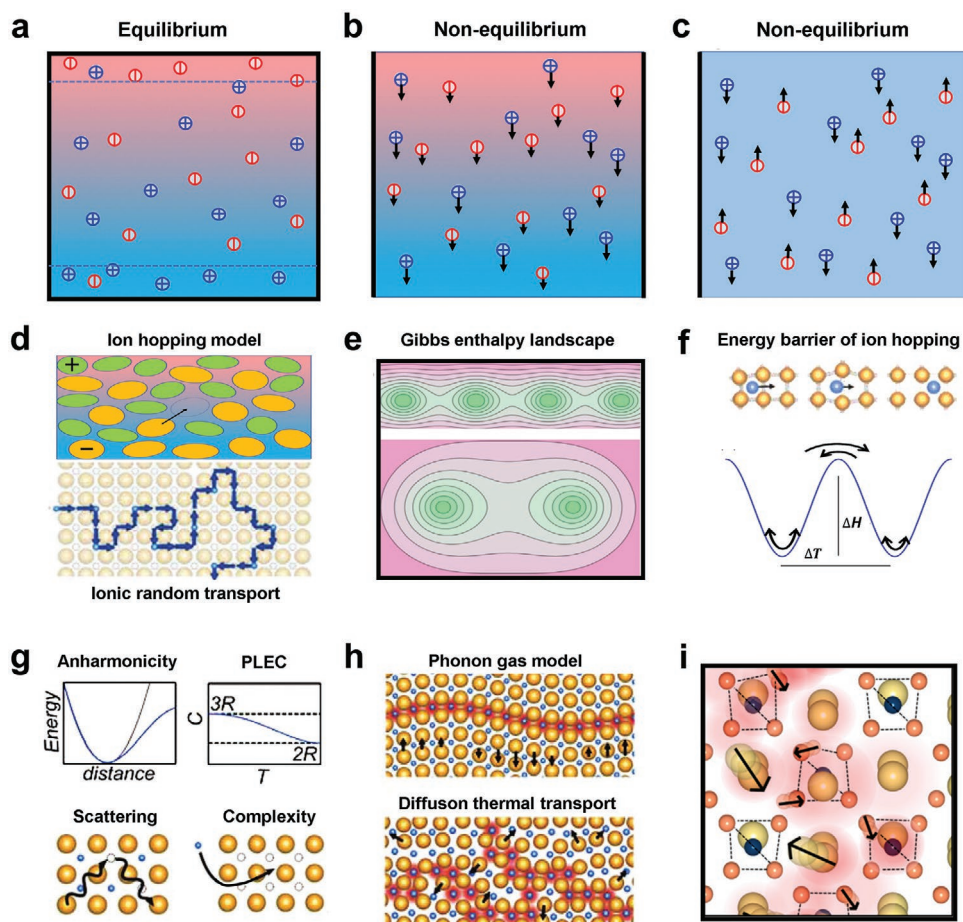


Figure 3. Schematic diagram of a) equilibrium state of isothermal i-TE systems, with no ion flows. Nonequilibrium state of isothermal i-TE systems, where cations and anions flow toward the b) same direction, and c) opposite directions. Reproduced with permission.^[40] Copyright 2020, American Physical Society. d) Ion hopping model indicating the formation of vacancy (top) and ionic random transport path (bottom). e) Gibbs enthalpy landscape where ion hops over the barrier to neighboring sites. f) Gibbs enthalpy during hopping dynamics, where the temperature on the left is higher than the right side, showing stronger thermal fluctuations and more frequent jumps to the right side. Reproduced with permission.^[63] Copyright 2021, American Physical Society. g) Underlying effects for low ion thermal conductivities. h) Long-range phonon-gas model (top) and local-scale diffuson model with correlated atomic displacements (black arrows), and heat transfer (red lines). Reproduced with permission.^[60b] Copyright 2022, Wiley-VCH. i) Heat transport between uncorrelated atomic vibrations in the diffuson model, where arrows show schematic eigenvectors. Reproduced with permission.^[60a] Copyright 2022, American Chemical Society.

are reflections of kinetic diffusion under the concentration gradient and thermal diffusion under the temperature gradient, respectively. Note that the latter term can be regarded as a product of c and thermodiffusive drift velocity $v = -D_T \nabla T$.^[23a]

2.2.2. Cross-Coupling Effects

Despite mass diffusion and thermophoresis effect have been considered in the above discussions, i-TE systems are practically more complicated where cross-coupling effects are of importance. In the nonequilibrium simulation, cations and anions allowing charge flow in both cooperation and confrontation approaches (Figure 3b,c).^[40] Turbulent flow is caused by specific neighboring vicinity, in which the collision and friction between free carriers and adjacent layers can occur. Ion currents drag themselves within layer surfaces, which bring either

positive or negative isotropy deviations.^[28] The quantification of such ion pair-interaction potential is difficult and determined by the inherent characteristic (volume, viscosity, permittivity, etc.) of individual i-TE species.^[41]

On the other hand, in the static equilibrium simulation, ions gradually accomplish accumulation driven by temperature difference. A counter electrical field will be generated to prohibit ion species transfer. Considering such cross-coupling situation, the drift of ion flux density is redefined as^[42]

$$J = J_D + J_T + J_E \approx -D \left(\nabla c + c \frac{Q^*}{k_B T^2} \nabla T - c \frac{qE}{k_B T} \right) \quad (3)$$

where $J_E = \frac{qD}{k_B T} cE$ is the ion flux density driven by the counter electric field, q is the unit ion charge, and E is the electric field intensity which is further described as^[43]

$$E = -\psi_0 \frac{\nabla T}{T} \quad (4)$$

where ψ_0 is the thermoelectric potential factor, determined by the i-TE system nature. Specifically, in a binary monovalent i-TE system, there is^[36b]

$$\psi_0 = \frac{Q_C^* - Q_A^*}{2e} \quad (5)$$

where Q_C^* and Q_A^* are the “heat of transport” of cation and anion species, respectively.

2.2.3. Derivation of Soret and Seebeck Coefficient

First, according to the Soret effect, the thermovoltage is mainly due to different thermodiffusion rates from cations to anions, which is rooted in their respective mobility. Under an equilibrium state with no external force, given $J = 0$, we have the definition of stationary ionic concentration gradient regarding Equation (2)

$$\nabla c = -\frac{D_T}{D} c \cdot \nabla T = -S_T c \cdot \nabla T \quad (6)$$

where $S_T = \frac{D_T}{D}$ is the Soret coefficient.^[23a] The essence of S_T is to indicate relative ion concentration gradient against temperature gradient $\left(\frac{\nabla c}{c} = -S_T \cdot \nabla T\right)$, leading to the derivation of S envisaging for thermodiffusive i-TEs as thermovoltage against temperature difference, namely $\Delta V = -S \cdot \Delta T$. Based on the classical thermodynamic model, S_T is related to Q^* , which is the driving force^[44]

$$S_T = \frac{Q^*}{k_B T^2} \quad (7)$$

Second, the key parameter differentiating i-TEs from e-TEs is the S , which determines the magnitude of thermovoltage under a certain ΔT . The Born model was also proposed in 1920 to define the ionic Seebeck coefficient^[45]

$$S = \frac{Q^*}{N_A |q| T} \quad (8)$$

where N_A is Avogadro's constant.

In addition, the Seebeck coefficient for dual-ion electrolytes can be expressed by combining the Q^* difference between the cation and anion species^[40]

$$S = \frac{w_+ Q_+^* - w_- Q_-^*}{eT} \quad (9)$$

where Q_{\pm}^* is the weight mean, and $w_{\pm} = \frac{n_{\pm}}{n_+ + n_-}$ is the weight factor of positive and negative ions. The value of $\hat{S}^* = \frac{Q^*}{T}$ is

defined as the Eastman entropy, which is a combination of the transported entropy and the partial molar entropy.^[46] Therefore in the microscopic scheme, the normally much larger S of i-TE materials than that of e-TE materials can be attributed to the difference in electronic Eastman entropy conceived in their respective thermoelectric process.^[47]

2.2.4. Heat of Transport

As the value of Q^* plays an important role in the i-TE Soret coefficient and Seebeck coefficient, its evaluation should be summarized case by case. In liquid solutions, the evaluation of Q^* consists of thermodynamic and hydrodynamic two aspects, which is in accordance with Equation (1).^[48] By assuming a most simple model, where charge interactions are restricted to electrostatics forces without dispersion, solvation, hydrogen bonds, etc., Q^* can be described based on the Stokes–Einstein friction law^[49]

$$Q^* = \tau \frac{q^2}{8\pi\epsilon a} \quad (10)$$

where $\tau = -\frac{d \ln \epsilon}{d \ln T}$ is the numerical factor for temperature-dependent correction, ϵ is the permittivity, a is the radius of spherical-regarded particles.

More recently, the Debye screening length λ was considered to the expression of Q^* . It was found the ratio of a to λ crucially determined the calculation of Q^* , where small size and large size ions are deduced respectively as^[36a,50]

$$Q^* = \left(\tau + (\tau + 1) \frac{a}{2\lambda} \right) \frac{q^2}{8\pi\epsilon a}, \quad (a < \lambda) \quad (11)$$

$$Q^* = (\tau + 1) \frac{\lambda^2}{a^2} \frac{q^2}{8\pi\epsilon a}, \quad (a > \lambda) \quad (12)$$

Regarding the solid-state matrix and gel-like systems, where strong interactions contribution need to be considered, hopping theory is introduced to describe the ionic transport behavior.^[40] As shown in Figure 3d, ion carriers as the effective components of the entire i-TE system, are trapped at given sites and hop between neighbors after activation. Thus, their transport routine is random, which is disagree with e-TE materials. The hopping enthalpy landscape of a transport channel is displayed in Figure 3e, and the diagrammatic sketch of hopping energy is shown in Figure 3f. During the hopping process, the Gibbs enthalpy is reflected by the height of the energy peak, and the Gibbs entropy is reflected by the width of the valley at the adjacent degenerate minima. Under certain ΔT , forward hops are faster than backward hops, which leads to unidirectional net thermodiffusion with a Q^* expression of^[51]

$$Q^* = \Delta H + k_B T - \frac{d\Delta G}{dc} T \frac{dc}{dT} \quad (13)$$

2.3. Fundamentals of Ion Thermo-Redox

Completely different from physical thermodiffusion based i-TE materials, the thermo-redox process is essentially a thermal-driven chemical reaction. Thus, the TE conversion fundamental is more complex, which cannot be analogized from the analysis of chemical potential. In this section, we describe the relevant contents of current density according to the redox kinetics. However, the expression of S is deduced based on redox thermodynamics.

2.3.1. Redox Kinetics

As a basic kinetic relationship in the field of electrochemistry, the Butler–Volmer equation gives the dynamic current density as^[52]

$$J = J_0 \left[\exp\left(\alpha_a \frac{nF}{RT} \eta\right) - \exp\left(-\alpha_c \frac{nF}{RT} \eta\right) \right] \quad (14)$$

where J_0 is the exchange current density, α_a and α_c are charge transfer coefficients along the anode and cathode direction respectively, and $\eta = E - E_{\text{eq}}$ is the activation overpotential.

While J is defined as the current per unit area on the electrode surface, an additional expression can be deduced by the volumetric reaction rate across the electrode/electrolyte interface, in charge balance condition^[53]

$$J \cdot A = nFR_V \quad (15)$$

where R_V is redox reaction rate (positive sign for the cathodic reaction), and A is electrode surface area.

2.3.2. Redox Thermodynamics

Unlike what happens in e-TE or thermodiffusive i-TE materials, a thermogalvanic i-TE material is free from electronic transport, and therefore is independent on the flux density of charge carriers. Instead, it is the enthalpy change during the redox process that determines the magnitude of generated thermovoltage. Irrespective of an oxidation or a reduction reaction, its redox reaction enthalpy (H) can be expressed using the Gibbs free energy (G) as^[54]

$$\Delta G = \Delta H - T\Delta\hat{S} \quad (16)$$

where \hat{S} is the redox reaction entropy. Based on the definition, the relationship between electric potential (E) at electrodes and G is^[55]

$$\Delta G = -nFE \quad (17)$$

where F is the Faraday constant, and n represents the number of electrons that are exchanged in the redox procedure. Combining Equations (16) and (17), E can be expressed as

$$E = \frac{T\Delta\hat{S} - \Delta H}{nF} \quad (18)$$

At this stage, we can define the ionic Seebeck coefficient of thermogalvanic i-TE materials as

$$S = \frac{dE}{dT} = \frac{\Delta\hat{S}}{nF} \quad (19)$$

where the dynamic value of nF can be evaluated from the kinetics analysis of Equations (14) and (15).

2.4. Heat Conductivity

I-TE materials are featured with low thermal conductivity values, which are commonly explained by the influences due to anharmonicity (phonon–phonon scattering),^[56] “phonon liquid electron crystal,”^[57] structural disorder (point-defects),^[58] and component complexity (phonon boundaries),^[59] as shown in Figure 3g. Rather than the conventional phonon-gas transport model, a dynamic diffuson model has been proposed very recently to contrapuntally explain the heat transport of i-TE materials based on the effective medium theory.^[60] As demonstrated in Figure 3h, phonons carry heat in a long-scale range via propagation (phonon-gas model), which is generally accepted in ordered crystallized TE materials.^[61] However, diffusons are recognized as the heat transport medium of i-TE materials. Instead of propagation, random diffuson happens on a local length scale. Atomic-level mass migration promotes diffuson squeeze to the adjacent vacancy, where thermal energy is carried (Figure 3i). Plenty experimental results in assistance with the diffuson model are verified. Moreover, unlike ion transfer which alters with the external environment (e.g., temperature), the ion vibrations contribute equally to heat transfer at a temperature >100 K.

More reasonably, the thermal conductivity of i-TE materials is attributed to a two-channel model, by parallel integration of the phonon-gas-type term and the diffuson-type term^[56b,60]

$$\kappa = \kappa_{\text{ph}} + \kappa_{\text{diff}} \quad (20)$$

$$\kappa_{\text{diff}} = \frac{1}{\pi} n^{\frac{1}{3}} k_B \int_0^{\omega} \frac{C(\omega) g(\omega)}{k_B} \frac{\omega d\omega}{3n} \quad (21)$$

where n is the atom number density, $g(\omega)$ is the diffuson vibrational density of states, and $C(\omega)$ is the heat capacity.

Regarding the attribution of κ_{ph} , the Mattheissen’s rule is normally used to determine the temperature-dependent phonon scattering rate^[62]

$$\tau^{-1} = \tau_p^{-1} + \tau_b^{-1} = C_1 \omega^2 T e^{-\frac{C_2}{T}} + A\omega \quad (22)$$

where C_1 , C_2 , and A are experimental constants capturing the phonon–phonon scattering (C_1 , C_2) and the boundary scattering (A), respectively.

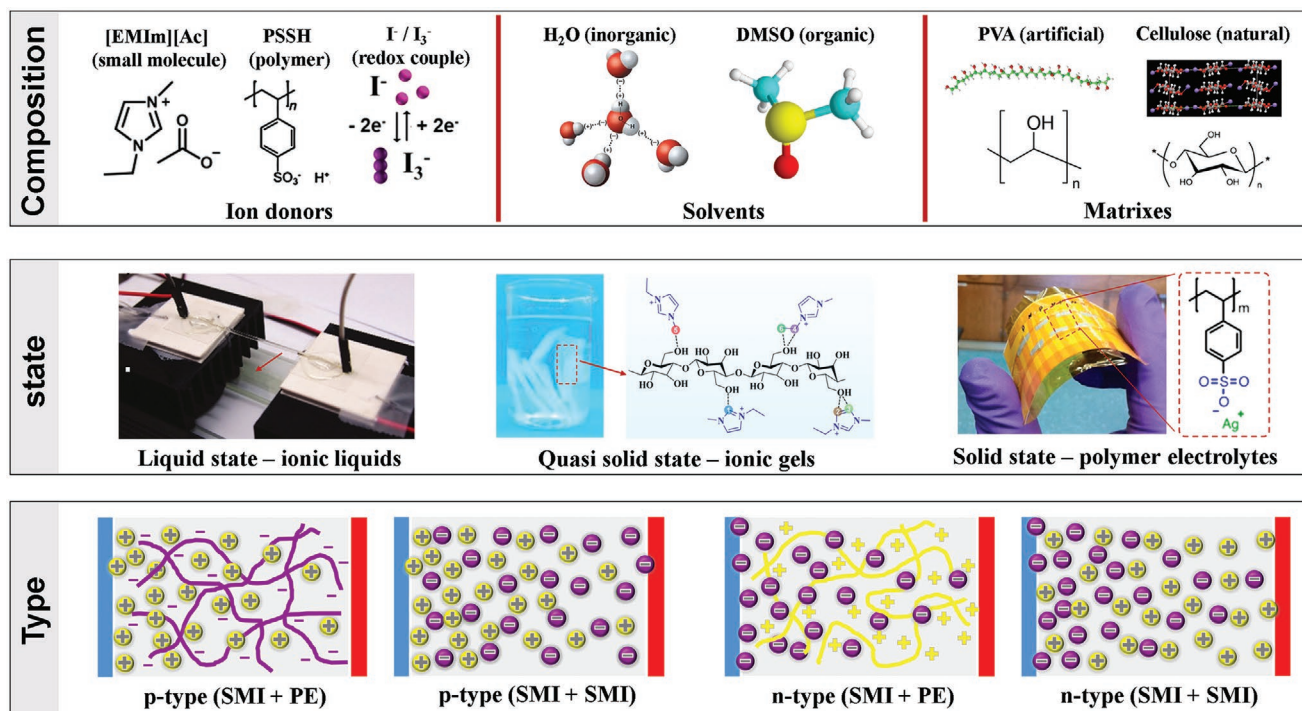


Figure 4. The classification of i-TE materials based on material composition, physical state, and dominant charge carrier type. Reproduced with permission.^[66] Copyright 2019, Cell Press. Reproduced with permission.^[12] Copyright 2019, Springer Nature. Reproduced with permission.^[67] Copyright 2019, Elsevier. Reproduced with permission.^[68] Copyright 2016, Wiley-VCH. Reproduced with permission.^[69] Copyright 2021, Wiley-VCH. Reproduced with permission.^[70] Copyright 2013, American Chemical Society.

2.5. Existing Disputes

There is a disputing opinion about the S of i-TE materials taking the electrode properties into account. Instead of an inherent nature of the materials, such a viewpoint proposes that the S value is determined by the assembly engineer of the whole device.^[64] Specifically, the theory of ionic adsorption infers that the thermovoltage arises from the ion adsorption on the electrode surfaces. The adsorption degree at unit temperature is suggested to judge the TE conversion capability instead of the Soret effect. Herein, we assign the electrode ionic adsorption effects to the capacitance property of i-TE device. Although the interchange of the electrode will influence the measured S value, it can be regarded as an apparent exhibition extent rather than the intrinsic TE conversion capacity of the material. Detailed discussions about how electrode materials influence device capacitance will be involved in this article hereafter.

Recently, researchers also questioned the rationality of using ZT value to comprehensively evaluate i-TE performance. Perspectives are presented that the S value is only determined by the Eastman entropy, whereas the ionic diffusion coefficient relies on the speed of steady-state establishment. Different from the present cognition of $ZT = S^2 \sigma T / \kappa$, a larger response time of i-TE equilibrium leads to instability in voltage formation, which is closely dependent on the temperature field evolution. As a result, a novel expression is accordingly given for i-TE materials, taking the magnitude of accumulated net charge (C) and the rate of electricity generation $\left(\frac{G_T}{\rho c}\right)$ into account^[65]

$$ZT = \frac{CS^2 G_T}{\kappa \rho c} T \quad (23)$$

where G_T is the interfacial thermal conductance, ρ is the material density, and c is the specific heat capacity.

3. I-TE Materials

In this section, we overview the common composition and physical state of i-TE materials, as shown in **Figure 4**. Diverse types of ionic charge carriers based on which the taxonomy of i-TE materials can be classified are also discussed. As compared in **Figure 5**, the unique physical and chemical properties of i-TE materials endow them with a wide range of application including thermal sensors, energy conversion, and energy storage, while e-TE materials are generally applied for thermal management, thermal sensor, and energy conversion.

3.1. Composition

Unlike e-TE materials which are normally in a single homogeneous phase, i-TE materials usually refer to a complicated system consisting of ions as function component, solvents to promote ion migration, and matrixes to support the material strength. If using liquid ion species, external packaging materials should also be applied to prevent evaporation, which are out of the scope of this review and will not be discussed exhaustively.

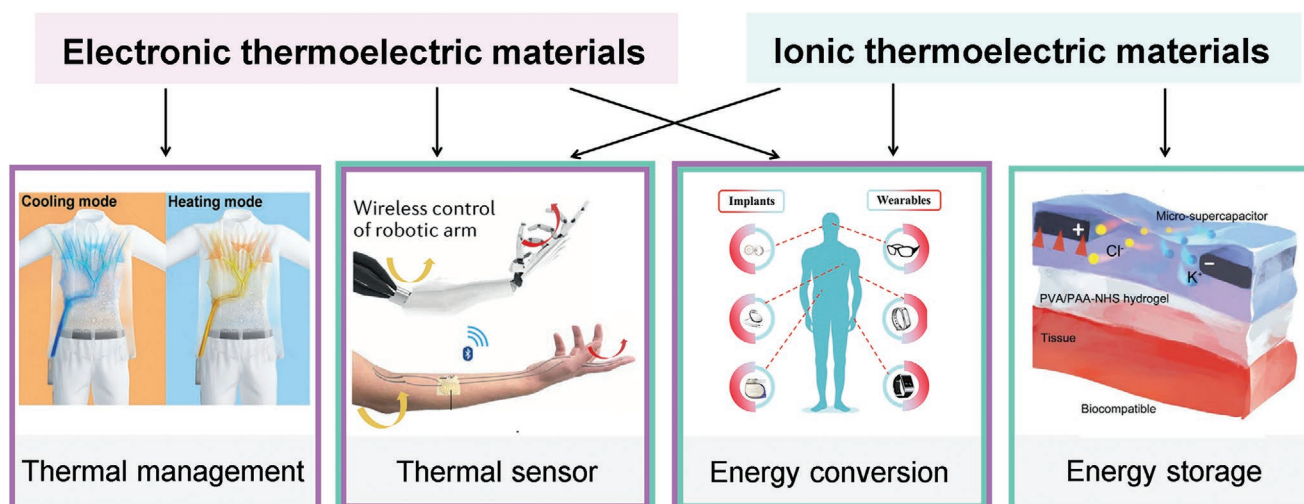


Figure 5. Distinctive application areas of e-TE and i-TE materials. Reproduced with permission.^[71] Copyright 2022, Wiley-VCH. Reproduced with permission.^[72] Copyright 2020, American Association for the Advancement of Science. Reproduced with permission.^[73] Copyright 2019, Wiley-VCH. Reproduced with permission.^[74] Copyright 2021, Wiley-VCH.

3.1.1. Ion Donor

Ion donors play a dominant role in generating thermovoltage. Potential sources of ions are provided by polar electrolytes, such as ILs, salt solution, and polyelectrolytes.^[12] ILs are a widely used type of electrolytes providing ion species for i-TE materials, which are in liquid state at room temperature.^[75] Due to the superiorities of low vapor pressure, low κ , wide operating temperature range, and desirable thermal and chemical stability, ILs have been increasingly used in i-TEs.^[76] **Table 1** summarizes the chemical structure, TE performance, and melting point (T_m) of ILs reported recently. As can be seen, ILs are feasible for both n-type and p-type (as per the sign of S) i-TE materials, with the magnitude of S ranging from hundreds of $\mu\text{V K}^{-1}$ to several mV K^{-1} .^[28,77] Analogous to ILs, acid/base/salt solutions are inorganic small-molecule i-TE ion donors. However, unlike room temperature ionizable ILs, most of the acids/bases/salts are solid crystals, where pre-preparation of solutions is demanded.

Organic polyelectrolyte is another type of i-TE ion donors. Organic polyelectrolyte has the advantages of cheap, widely available, formable, and self-standing over inorganic ILs.^[79] The general ion diffusion mobility in polyelectrolytes is normally lower than that in ILs, while conversely, the diffusion mobility difference between cations and anions is larger, making polyelectrolyte-based i-TE materials have a comparable S with that of IL-based i-TE materials. For instance, poly(sodium 4-styrenesulfonate) (PSSNa) exploits the concentration difference of PSS⁻ and Na⁺ for generating thermovoltage.^[80] Under a low-grade ΔT , PSS⁻, a type of covalently bonded macromolecule chain, can hardly migrate, while Na⁺ tends to populate on one of the electrodes than the other, resulting in a S of 4 mV K^{-1} . There are two working modes implemented by i-TE ion donors, as schematically illustrated in **Figure 6**. Figure 6a shows the case where cations and anions are all mobile (inclusive ILs and acid/base/salt solutions), which has a relatively small S .^[81] Figure 6b

shows the case of negatively charged backbone and itinerant protons, or vice versa (inclusive polyelectrolytes), which has a relatively large S .

Redox couple is a specific type of ion-donor mainly contributing to thermogalvanic effect.^[82] Unlike thermodiffusion based ion donors, outstanding ability of continuous generating energy can be realized by redox ion species, without by-product emissions and irreversible ion consumptions.^[83] $\text{Fe}(\text{CN})_6^{3-}/\text{Fe}(\text{CN})_6^{4-}$, $\text{Fe}^{3+}/\text{Fe}^{2+}$, I^{3-}/I^- , $\text{Sn}^{2+}/\text{Sn}^{4+}$, and $\text{Co}^{2+}/\text{Co}^{3+}$ are all reported redox couples adopted by in i-TE systems.^[23a,84] The S of the most common redox ion species has been measured or calculated.^[83c,85] $\text{Fe}(\text{CN})_6^{3-}/\text{Fe}(\text{CN})_6^{4-}$ is one of the efficient couples with a S of $\approx 2 \text{ mV K}^{-1}$.^[84d,86] More recently, combinations of dual redox couples (dibutanylferrrocene and iodine) with a synergistic effect were reported with a maximum S of 1.67 mV K^{-1} , raising from the formation of charge-transfer complexes.^[87] Another newly explored organic redox couple of thiolate/disulphide was reported with a S of -0.6 mV K^{-1} ,^[88] with great potential in avoiding electrochemical corrosions.

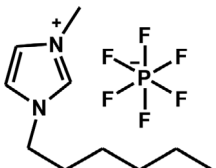
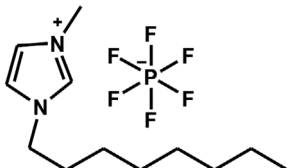
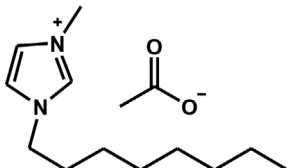
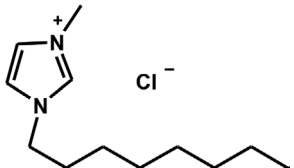
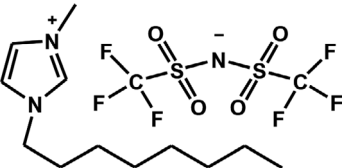
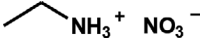
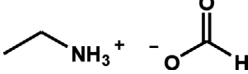
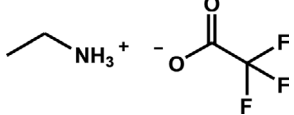
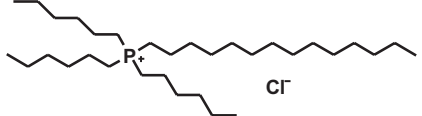
3.1.2. Solvent

Solvents are commonly applied as i-TE component to facilitate the dissociation and migration. Both inorganic solvents and organic solvents have been reported as i-TE additives. H₂O is the most widely accepted solvent which is biocompatible, environmentally friendly, and noncorrosive. However, H₂O has its weakness lying in high volatility, which results in material instability and requires packaging treatment.^[89] In addition, there are a variety of organic solvent reported with promise in forming i-TE materials. For instance, dimethyl sulfoxide (DMSO) was adopted to fabricate poly(3,4-ethylenedioxythiophene) PEDOT/IL i-TE thin films via 3D-printing process, which have outstanding mechanical properties and reasonable

Table 1. Chemical structures, TE parameters, and melting points of common ionic liquids (ILs).^[29,68,77,78]

| ILs | Chemical structure | σ [mS cm ⁻¹] | S [mV K ⁻¹] | T _m [°C] |
|---|--------------------|---------------------------------|-------------------------|---------------------|
| [EMIM:Ac] | | 3.7 | 2.22 | -20 |
| [EMIM:BF ₄] | | 15.7 | -0.19 | 15 |
| [EMIM:TFSI] | | 8.6 | -1.45 | -15 |
| [EMIM:CF ₃ SO ₃] | | 9.7 | -0.36 | -10 |
| [BMIM:TFSI] | | 0.4 | -0.94 | -16 |
| [BMIM:PF ₆] | | 1.4 | -0.62 | -8 |
| [BMIM:BF ₄] | | 4.5 | -0.61 | -75 |
| [HMIM:TFSI] | | 2.1 | -0.78 | -4 |
| [HMIM:I] | | 0.2 | 0.13 | <RT |

Table 1. Continued.

| ILs | Chemical structure | σ [mS cm ⁻¹] | S [mV K ⁻¹] | T_m [°C] |
|-------------------------|---|---------------------------------|---------------------------|------------|
| [HMIM:PF ₆] |  | 0.6 | -1.01 | -8 |
| [OMIM:PF ₆] |  | 0.3 | -1.07 | -82 |
| [OMIM:Ac] |  | 3.5 | 2.34 | N.A. |
| [OMIM:Cl] |  | 0.09 | 0.64 | N.A. |
| [OMIM:TFSI] |  | 1.2 | -0.38 | <RT |
| [EAN] |  | 25.2 | 0.68 | 12 |
| [EAF] |  | 16.3 | -1.40 | N.A. |
| [EATA] |  | 46.1 | 0.58 | N.A. |
| [P666,14:Cl] |  | 5.9 | 0.23 | N.A. |

TE performance.^[77a,90] The assembled TE generator enjoys a favorable working stability (power density retained above 85% compared with the original value of 6.8 $\mu\text{W cm}^{-2}$) under repeatedly stretching and cutting–repair cycles. Deep eutectic solvent of choline chloride (ChCl):ethylene glycol (EG), supported by 50% waterborne polyurethane (WPU), was also reported with a colossal S of 19.5 mV K⁻¹ at a 90% relative humidity environment and favorable mechanical stretchability of 216%.^[91]

3.1.3. Matrix

Matrixes serve as i-TE supports to work for ensuring formability, flexibility, and mechanical strength, covering artificial polyvinyl alcohol (PVA),^[92] polyvinylidene fluoride (PVDF),^[14] and natural cellulose,^[12] gelatin.^[21] For instance, inorganic additives blended PVA i-TE biomedical hydrogels are flexible, transparent, and cost-effective.^[92] Nanofibrillated cellulose (NFC) was also adopted as the matrix to prepare an i-TE paper,

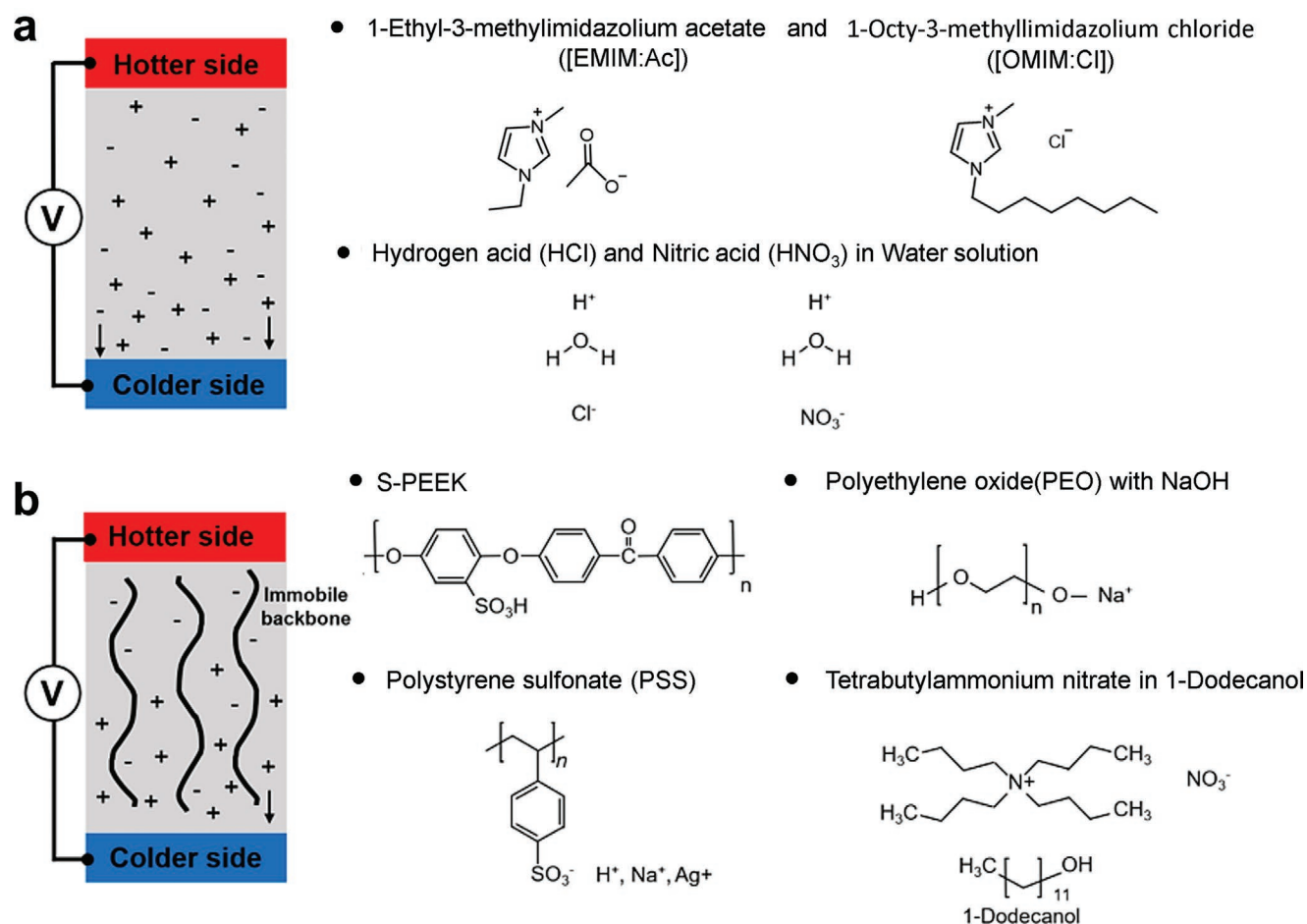


Figure 6. Working mechanism of ion donors of a) both cations and anions are mobile, and b) immobile polyelectrolyte backbone and mobile counter ions. Reproduced with permission.^[81] Copyright 2021, Elsevier.

which can stand a weight of 100 g with only 80 μm thickness, therefore is suitable for roll-to-roll processing.^[93] By introducing bacterial cellulose (BC) as skeleton support, advantages of high mechanical strength of 42 MPa, high crystallinity of 80%, and admirable ionic capacity of 99 wt% were endowed.^[69] Polyurethane (PU) reinforced i-TE gels favor a high ZT of 0.99 ± 0.3 , excellent elongation at a break of 300%, and self-healable competence.^[94] More recently, inorganic SiO_2 nanoparticles were reported as a matrix to support i-TE materials.^[20] An exceptional $S^2\sigma$ of $1040.4 \mu\text{W m}^{-1} \text{K}^{-2}$ at room temperature was achieved, which is one of the largest value reported in this field. Except for external matrix species, polyelectrolytes can stand for both the ion donor and the matrix single-handed. One should notice that partial insulative matrixes may hinder the ions transfer, where the specific gravity of matrixes should be optimized.

3.2. Physical State

I-TE materials can be classified with three physical states: liquid state, quasi-solid state, and solid state. Unlike e-TE materials, i-TE materials have been investigated in a com-

pletely liquid state, such as pure ILs, salt aqueous solutions, and salt organic solutions.^[95] For instance, 1-ethyl-3-methylimidazolium bis(trifluoromethylsulfonyl)imide ([EMIM][TFSI]) and 1-octyl-3-methylimidazolium hexafluorophosphate ([OMIM][PF₆]) sealed in a flexible silicone tube have been reported as a liquid i-TE material with the highest S of 1.446 mV K^{-1} .^[68] However, its κ is supposedly to be high because both heat transfer and heat convection contribute to thermal conduction.

Quasi-solid state i-TE materials (mainly refers to ionic hydrogels or ionogels), which exhibit larger S and lower σ than ILs, as compared in Table 2.^[77a,96] For instance, a poly(vinylidene fluoride-co-hexafluoropropylene) (PVDF-HFP)/[EMIM:DCA] ionogel was reported to exhibit a giant S of 26.1 mV K^{-1} , a high σ of 6.7 mS cm^{-1} , and a ZT of 0.75.^[14] Very recently, it was reported that inorganic SiO_2 nanoparticle incorporated [EMIM:DCA] ionogels exhibit a state-of-the-art ZT of 1.47 at room temperature. The corresponding S , σ , and κ are 14.8 mV K^{-1} , 475 mS cm^{-1} , and $0.21 \text{ W m}^{-1} \text{K}^{-1}$, respectively.^[20] Polymethylmethacrylate (PMMA)/single-wall carbon nanotube (SWCNT) is another typical quasi-solid composite gel, which can be incorporated with $\text{Sn}^{2+}/\text{Sn}^{4+}$ redox couples to render a high σ to 105 mS cm^{-1} and a maximum $S^2\sigma$ of

Table 2. Selective state-of-art i-TE materials.

| Matrixes | Ion donors | Type | σ [mS cm ⁻¹] | S [mV K ⁻¹] | S ² σ [μ W m ⁻¹ K ⁻²] | K [Wm ⁻¹ K ⁻¹] | ZT | Relative humidity [%] | Refs. |
|--|--|------|---------------------------------|-------------------------|---|---------------------------------------|-----------------------|-----------------------|-------|
| Salt solutions | | | | | | | | | |
| | TBAN-dodecanol | p | 0.01 | 7.2 | 0.06 | 0.17 | 1.08×10^{-4} | N.A. | [46a] |
| Polyelectrolytes | | | | | | | | | |
| | PSSH | p | 90.0 | 7.9 | 562.0 | 0.38 | 0.44 | 70 | [98] |
| | Nafion-Ag | p | ≈ 10.0 | 1.1 | 1.2 | 0.22 | 0.016 | ≈ 95 | [70] |
| | PSS-Ag | n | ≈ 16.0 | -2.1 | 7.1 | 0.40 | 0.053 | ≈ 95 | [70] |
| | PSSNa | p | 11.8 | 4.0 | 18.9 | 0.49 | 0.012 | 100 | [80] |
| | S-PEEK | p | 20.0 | 5.5 | 60.5 | N.A. | N.A. | 70 | [16] |
| | PDDAc | p | 19.0 | 18.0 | 615.6 | N.A. | N.A. | 70 | [16] |
| | Nafion | p | 19.0 | 3.6 | 24.6 | N.A. | N.A. | 70 | [16] |
| | Graphene oxide | p | 4.0 | 9.0 | 32.4 | 3.0 | 3.22×10^{-3} | N.A. | [100] |
| Gels | | | | | | | | | |
| PEO | NaOH | p | 0.08 | 11.1 | 1.0 | 0.22 | 1.35×10^{-3} | N.A. | [101] |
| Cellulose/PEO | NaOH | p | 20.0 | 24.0 | 1152.0 | 0.48 | 0.71 | N.A. | [12] |
| PVA | NaOH | n | 0.07 | -37.6 | 10.5 | 0.48 ± 0.03 | 0.065 | N.A. | [92] |
| PVDF-HFP | [EMIM:DCA] | p | 6.7 | 26.1 | 456.4 | 0.18 | 0.75 | 68–72 | [14] |
| WPU | [EMIM:DCA] | p | 8.4 | 34.5 | 999.8 | 0.23 | 1.30 | 90 | [102] |
| SiO ₂ | [EMIM:DCA] | p | 47.5 | 14.8 | 1040.4 | 0.21 | 1.47 | 72 | [20] |
| PVDF-HFP (ethanol treated) | [EMIM:DCA] | p | 17.6 | 25.4 | 1135.5 | 0.19 | 1.78 | 70–75 | [19] |
| BC | [EMIM:DCA] | p | 28.8 | 18.0 | 937.3 | 0.21 | 1.33 | N.A. | [69] |
| PU | [EMIM:DCA] | p | 12.8 | 25.6 | 838.9 | 0.24 | 0.99 | 70 | [94] |
| PEO | [EMIM:Ac] | p | 1.1 | 18.0 | 35.6 | N.A. | N.A. | 60 | [103] |
| PVDF-HFP/PEG | [EMIM:TFSI] | p | 0.8 | 14.0 | 15.7 | N.A. | N.A. | N.A. | [12] |
| WPU | [ChCl:EG] | p | 8.4 | 19.5 | 319.4 | 0.20 | 0.48 | 90 | [91] |
| PANI/PAAMPSA | H ₃ PO ₄ | p | 237.0 | 8.1 | 1555.0 | 0.45 | 1.04 | 90 | [104] |
| Graphene oxide | PSSH | p | 114.0 | 12.6 | 1809.9 | 0.64 | 0.85 | N.A. | [105] |
| PVA | NaI | p | 51.5 | 42.8 | 9434.0 | 0.54 | 5.18 | 50–70 | [97] |
| Polyacrylamide/ poly(sodium alginate) | LiCl | p | 10.0 | 10.5 | 109.7 | N.A. | N.A. | N.A. | [13b] |
| Redox-induced materials | | | | | | | | | |
| | [Fe(CN) ₆] ³⁻ /[Fe(CN) ₆] ⁴⁻ (guanidinium and urea modified) | p | ≈ 50.0 | 4.2 | 88.2 | ≈ 0.30 | 0.087 | N.A. | [34] |
| PMMA/SWCNT | Sn ²⁺ /Sn ⁴⁺ | p | 105.0 | 1.1 | 13.5 | N.A. | N.A. | N.A. | [84a] |
| PVA | Fe ²⁺ /Fe ³⁺ | p | ≈ 9.5 | 1.0 | 1.0 | 1.88 | 1.59×10^{-4} | N.A. | [84c] |
| PVA | [Fe(CN) ₆] ³⁻ /[Fe(CN) ₆] ⁴⁻ | n | ≈ 6.0 | -1.2 | 0.9 | 1.85 | 1.45×10^{-4} | N.A. | [84c] |
| Anisotropic PVA | [Fe(CN) ₆] ³⁻ /[Fe(CN) ₆] ⁴⁻ | p | 46.0 | 1.5 | 10.4 | 0.40 | 7.60×10^{-3} | N.A. | [106] |
| Gelatin/KCl | [Fe(CN) ₆] ³⁻ /[Fe(CN) ₆] ⁴⁻ | p | ≈ 5.0 | 17.0 | 144.5 | 0.15 | 0.29 | N.A. | [21] |
| Poly(N-isopropylacrylamide) | I ⁻ /I ³⁻ | n | 1.0 | -1.9 | 0.4 | -0.45 | 2.38×10^{-4} | N.A. | [67] |
| PVDF-HFP/3-methoxypropionitrile | [Co(bpy) ₃] ²⁺ /[Co(bpy) ₃] ³⁺ | p | N.A. | 2.2 | N.A. | 0.67 | N.A. | N.A. | [15] |
| i-TE/e-TE hybrid materials | | | | | | | | | |
| PEDOT:PSS | CuCl ₂ | n | 52.6 | -18.2 | 1700.0 | 0.34 | 1.54 | 80 | [22] |
| PEDOT:PSS | PSSH | p | 120.0 | 16.2 | 3149.3 | N.A. | N.A. | 90 | [18] |

$13.5 \pm 3.0 \mu\text{W m}^{-1} \text{K}^{-2}$ at room temperature.^[84a] A very inspiring result was reported in a PVA-NaI ionogel, where the ZT value can be calculated to be 5.18.^[97]

Both liquid and quasi-solid i-TE materials are facing the disadvantages of leakage and instability, leading to large scope of the development of solid i-TE materials, which are mainly based on unblended bulk polyelectrolytes, such as PVA, PSSNa, silver Nafion (Nafion-Ag), silver polystyrene-sulfonate (PSS-Ag), poly(4-styrenesulfonic acid) (PSSH), sulfonated polymer polyether-ether-ketone (S-PEEK), poly(vinylphosphonic acid-co-acrylic acid) (P(VPA-AA)), and poly(diallyldimethylammonium chloride) (PDDAC). Specifically, unipolar polymers of Nafion-Ag and PSS-Ag were first studied their ion conduction properties in 2016,^[70] which shows an exceptional positive S of 5 mV K^{-1} and a negative S of 1.5 mV K^{-1} , respectively. The PSSH film-assembled i-TE supercapacitors can generate a thermovoltage of 38 mV under a small ΔT of 5 K .^[98] Recently, a maximum S of 19 mV K^{-1} at 70% relative humidity was achieved in PDDAC-based i-TE solid thin films, which is attributed to the synergistic effect of Cl^- dissociation and thermodiffusion.^[16] However, solid i-TE materials also suffer from relatively low σ in a range of 10^{-5} – $10^{-2} \text{ S cm}^{-1}$ due to degraded ionic mobility, and therefore their ZT are commonly lower than those of quasi-solid i-TE materials.^[77a]

3.3. Conduction Nature

In e-TE materials, if no bipolar conduction occurring, the conduction nature is decided by the type of charge carriers. By contrast, in i-TE materials, the conduction nature is decided by active ion species. Overall, if anions cumulate near cold electrode and cations cumulate near hot electrode, the correspondent i-TE materials are of n-type conduction, while the opposite conduction represents p-type i-TE materials. There are four practical cases envisaged by an i-TE process, which results in n-type or p-type i-TE materials. First, mobile cations and immobile backbone, the i-TE materials are p-type. Second, mobile cations and anions, while cations have higher mobility than that of anions, the i-TE materials are p-type. Third, mobile anions and immobile backbone, the i-TE materials are n-type. Fourth, mobile cations and anions, while cations have lower mobility than that of anions, the i-TE materials are n-type (opposite to the second case).

It should be mentioned that the p–n conversion of i-TE materials can be achieved by tuning the cation/anion mobility and cation/anion confinement. For instance, a reverse of S from $+14$ to -4 mV K^{-1} can be realized by incorporating liquid neutral polyethylene glycol (PEG) into the polymer matrix.^[99] Piling up 18 pairs of these p-type and n-type i-TE materials electrically in series and thermally in parallel, a total effective S of 0.333 V K^{-1} can be obtained. The positive ferric/ferrous chloride/PVA complex thermogalvanic i-TE materials and negative potassium ferricyanide/ferrocyanide/PVA complex thermogalvanic i-TE materials shows the respective S being 1.02 and -1.21 mV K^{-1} .^[84c] An assembled i-TE device using 59 pairs of such n-type and p-type i-TE materials can generate a large open-circuit thermovoltage of 0.7 V within 15 s and a favorable output power

of 0.3 mW at the ΔT between human skin and ambient environment. Table 2 listed TE properties of partial in-progressed thermodiffusion-derived i-TE materials. As can be seen, i-TE gels exhibit relatively high TE performance where the maximum ZT value has reached 5.18.

4. Properties of I-TE Materials

In this section, we overview the TE properties and capacitance of i-TE materials, followed by discussing the mechanical properties and other favorable characteristics on the practical application viewpoint.

4.1. Measurement Method

Measurement methods for i-TE properties are totally different from those for e-TE properties, mainly due to the charge transfer hysteresis in i-TE materials.^[107] Specifically, the mass of a single ion is about three orders of magnitude higher than that of a single electron, making ion migration consume a relatively long time to reach equilibrium state.^[108] While e-TE properties are usually measured by transient methods, including the “four probe” method for measuring σ and S ,^[109] the measurement of i-TE σ and S are separately mainly via AC impedance method and homemade instruments as mainstream. The 3ω method is employed for measuring κ of both e-TE and i-TE materials at present.

The alternating current (AC) impedance simulation is the most widely used method for estimating σ of i-TE materials, by electrochemical workstation equipment. In principle, ions and electrons behavior different reaction time with the application of AC voltage.^[110] Electrons respond more quickly to the alternating current, while ions are much slower. As a result, the detachment between ionic impedance and electronic impedance can be realized via AC frequency scanning. During practical testing, AC impedance is a numerically varying value with a real part and an imaginary part, which is related to the applied frequency.^[111] The key difference between the AC impedance method and the “four probe” method are:^[70,90,98,105] i) AC impedance measures bulk resistance, whereas “four probes” method measures in-plane resistance, ii) AC impedance method measures an open-circuit system, while the “four probes” method is only applicable for closed-circuit system. Figure 7a–c exhibits the AC impedance results, plotted in the polar coordinates, namely, the Nyquist spectroscopy.^[112] Typically, the Nyquist plots of i-TE materials consist of two segments. The signal in the low-frequency region (close to the end of the abscissa) corresponds with the electronic impedance R_e , and the signal in the high-frequency region (close to the origin of the abscissa) is mainly related to the ionic impedance R_i (R_e and R_i can simultaneously exist in i-TE systems).^[113] The interpretations of Nyquist curves are based on the proper establishment of equivalent circuits. For instance, i-TE materials can be sorted as three classes via the inserted Maxwell’s equivalent fitting spectroscopy:^[92,102,112] i) as shown in Figure 7a, the i-TE polyelectrolyte PSSNa exhibits merely R_i characteristics, where a specific spike appears at the low-frequency region, ii) as shown in Figure 7b, complete electronic conductor PEDOT-Tos

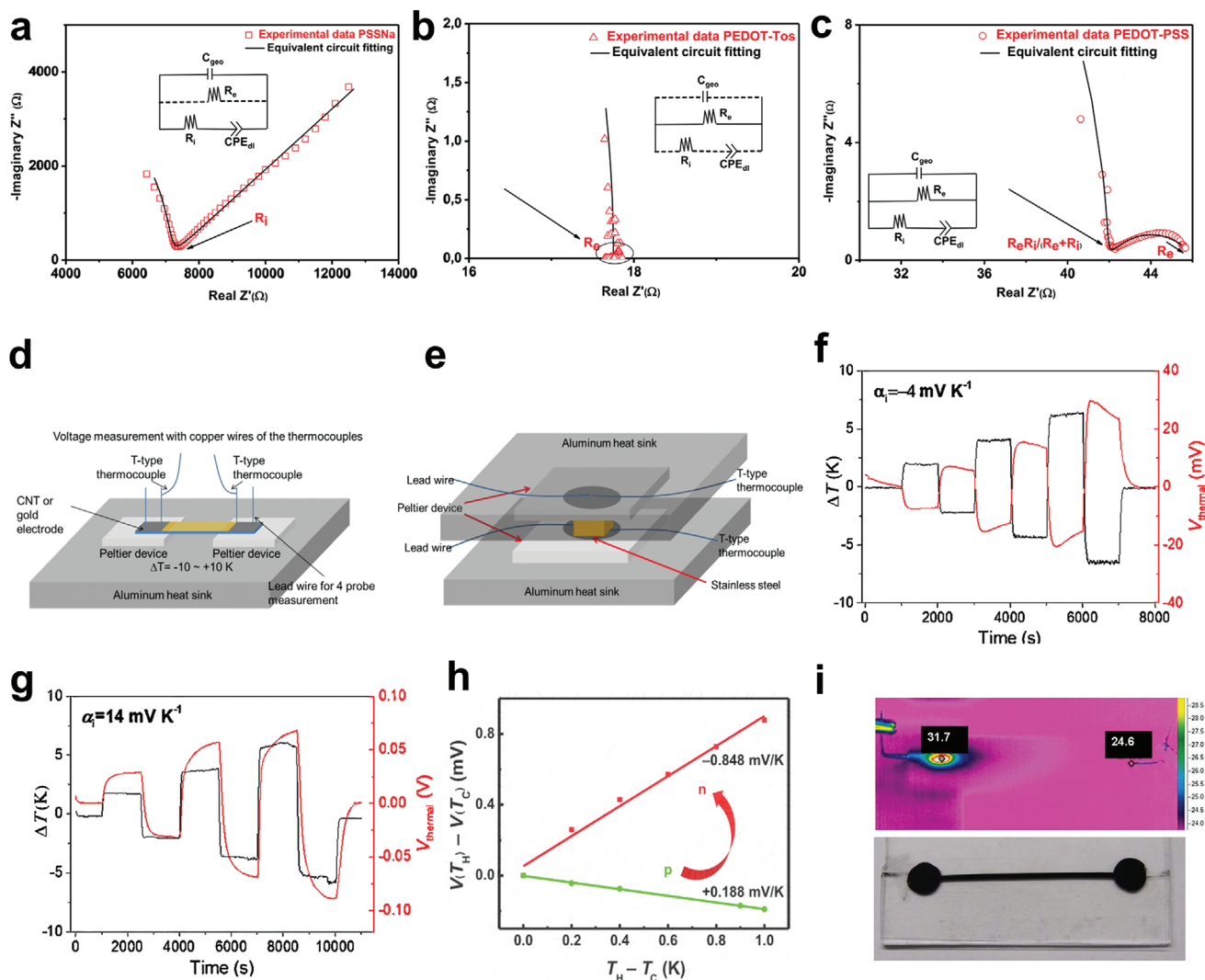


Figure 7. Measurement of i-TE properties. The Nyquist plot of a) sodium polystyrene sulfonate (PSSNa), b) PEDOT-Tos, and c) PEDOT-PSS. Reproduced with permission.^[112] Copyright 2015, Wiley-VCH. Illustration of the ionic Seebeck measurement setups along the d) in-plane direction, and e) out-of-plane direction. Reproduced with permission.^[98] Copyright 2016, Wiley-VCH. Plot of thermovoltage versus ΔT for f) n-type i-TE gels of 1-ethyl-3-methylimidazolium bis(trifluoromethylsulfonyl)imide/poly(vinylidene fluoride-co-hexafluoropropylene) ([EMIM:TFSI]/PVDF-HFP), and g) p-type i-TE gels of 1-ethyl-3-methylimidazolium bis(trifluoromethylsulfonyl)imide/poly(vinylidene fluoride-co-hexafluoropropylene)/polyethylene glycol ([EMIM:TFSI]/PVDF-HFP/PEG). Reproduced with permission.^[99] Copyright 2019, Springer Nature. h) Thermopower of 0.1 mM NaOH aqueous solution (green) and fully swollen NaOH/polyvinyl alcohol (PVA) hydrogels after air-drying at room temperature (red). Reproduced with permission.^[92] Copyright 2021, American Association for the Advancement of Science. i) IR photo and digital image of the 1-ethyl-3-methyl imidazolium bis[(trifluoromethyl) sulfonyl]imide ([EMIm][Tf₂N]) IL converter after heating at one end. Reproduced with permission.^[68] Copyright 2016, Wiley-VCH.

exhibits merely R_e characteristics, where all of the fitted points distributed at the high-frequency region, iii) as shown in Figure 7c, PEDOT-PSS exhibits both R_i and R_e characteristics, where a depressed semicircle at lower frequency and a segment of a macro semicircle within the higher frequency region can be observed from the fitting curve. The first intercept on the real axis represents R_e as tagged, whereas the second intercept in the high-frequency area represents the parallel combination of R_e and R_i , i.e., $[R_e \cdot R_i / (R_e + R_i)]$.

The experimental set-ups for measuring S along in-plane direction and out-of-plane direction are schematically displayed in Figure 7d,e.^[98,99,114] As can be seen, the temperature controls

employ Peltier devices attached to aluminum heat sinks, while the detections of temperature are recorded by thermocouples or thermal images, and the thermovoltages are collected by an electrochemical workstation or a source measure unit.^[68,78,91] Figure 7f,g plots the typical measurement results that are recorded by such instruments for both p-type and n-type i-TE materials.^[99] Two points are worth mentioning. First, a certain time is required for the establishment of steady-state.^[115] Second, the thermovoltage response to ΔT is proportional reproducible, implying the reliability of homemade instruments. Figure 7h shows the direct plots of thermovoltage versus ΔT , which behave excellent linear correlations. The positive and negative

slopes indicate n-type and p-type conductance, and the absolute value of slope is numerically equal to the magnitude of S .^[92,99]

For measuring κ , both the differential 3ω method^[101] and the laser flash apparatus method^[12] have been employed. Besides, κ values of i-TE materials have also been estimated based on the effective medium theory suitable for composites when the κ of every individual component is known.^[99] The calculation formula is described as follows regardless convections: $\kappa_T = \kappa_1 \cdot \Phi_1 + \kappa_2 \cdot \Phi_2$ (Φ refers to the weight ratio, and the subscripts T, 1, and 2 are on behalf of the total composite, component 1, and component 2 respectively). Owing to the presence of large amounts of organics and solvents within i-TE materials, the heat transmit abilities are generally of a relatively low grade. Besides, the κ of i-TE materials is at a low-grade level due to the absence of a long-range crystalline region as well. For instance, the infrared imaging of 1-ethyl-3-methyl imidazolium bis[(trifluoromethyl) sulfonyl]imide ([EMIm][Tf₂N]) in Figure 7i intuitively demonstrates the thermal resistance effect.^[68] As a result, the establishment of effective ΔT is feasible between two ends of the i-TE materials.

4.2. TE Performance

Although the performance of both e-TE and i-TE materials can be evaluated via ZT , their underlying microscopic characteristics are different. As can be seen in Figure 8a, the TE parameters of both e-TE and i-TE materials vary as the function of the density of charge carriers.^[102,116] In e-TE materials, the S value is negatively related to the carrier concentration, while the σ value is positively related to the carrier concentration. By contrast, κ is relatively independent on carrier concentration due to con-

taining a considerable fraction of lattice thermal conductivity κ_l . Consequently, carrier concentration must be optimized to maximize ZT .^[117] However, detailed summarization of analogous performance trend forecasts corresponding to i-TE materials has not been reported till now. Whereas in i-TE materials, there is no explicit trade-off between the S and the σ . It is acceptable to speculate that the ionic σ keeps consistently increasing/decreasing with the carrier densities, which is similar to the σ of e-TE materials. By contrast, the variation of S on carrier concentration in i-TE materials is rather complicated, because the S of i-TE materials can be rationalized via both thermodiffusion and thermogalvanic effects. In most circumstances, the S of i-TE materials is intrinsically triggered by ion migrations and redox couple thermoreactions. Therefore, higher carrier concentration promotes the boost of gathered charges, leading to higher thermovoltage.^[81,102] The permitted simultaneous optimization of S and σ offers potential breakthroughs for the $S^2\sigma$ enhancement in i-TE materials.

The inherently decoupled S and σ in i-TE materials provide exceptional potentials for increasing ZT , which, however, also result in the drawback that thermovoltage gradually decays after ion diffusion reaches saturation. As illustrated in Figure 8b, in the condition of depositing to an external circuit, electric current flows through immediately closed circuit via electrodes. As electron transport is continuously motivated from one electrode to the other, a countered electric potential forms and gradually congests, leading to the decaying trend of thermovoltage.^[91] If incorporating i-TE materials with e-TE materials, the S can approach to the exclusive S due to e-TE effect, which otherwise approaches to zero.^[101,112]

Figure 8c compares the S of thermodiffusive i-TE materials, thermogalvanic i-TE materials, inorganic e-TE materials,

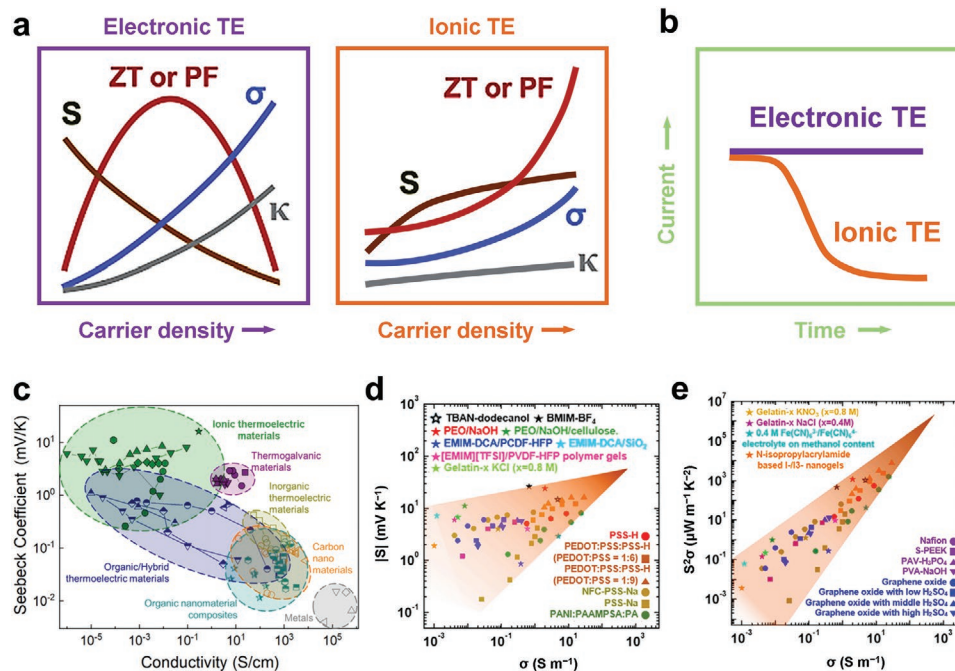


Figure 8. a) Dependence of TE properties on carrier density. b) Relationship between external circuit current and time under a constant ΔT . c) Summary of the S values as a function of σ values for different types of TE materials, Reproduced with permission.^[23a] Copyright 2021, American Chemical Society. Plots of d) $|S|$ and e) $S^2\sigma$ as a function of σ for i-TE materials. Reproduced with permission.^[81] Copyright 2021, Elsevier.

organic/hybrid TE materials, carbon nanomaterials, organic nanomaterial composites, and metals.^[23a] As can be seen, thermodiffusive i-TE materials exhibit the maximum S but a relatively lower σ . Additionally, thermogalvanic i-TE materials exhibit a second largest S with a comparable σ to that of organic/hybrid TE materials. Figure 8d,e further compares the S , σ , and $S^2\sigma$ of the reported i-TE materials.^[81] It is interesting to note that these data statistically converge at the $|S|$ of 10^2 mV K^{-1} and the $S^2\sigma$ of $\mu\text{W m}^{-1} \text{ K}^{-2}$, which implies the superior performance of i-TE materials.

4.3. Capacitance Performance

Another outstanding benefit of i-TE materials is to serve for energy storage applications, which plays an important role in renewable power generation, smart grids, internet of things.^[118] The capacitance performance of i-TE materials determines its potential as supercapacitors, which is incapable for e-TE materials.^[32a,119] As shown in Figure 9a, ion carriers migrate to the electrode surface under ΔT , which failed in continuously passing through external circuit. As a result, ions accumulate to generate an electric potential difference to work as a capacitor, as depicted in Figure 9b. Specifically, a single charging/discharging cycle contains four-stage process, where the corresponding voltage and ΔT are shown in Figure 9c. In the 1st stage, a certain ΔT is applied between the two electrodes so that

ions accumulate gradually to generate an increasing thermo-voltage. In the 2nd stage, a closed loop is built with an external resistor as the constant ΔT is maintained. The generated voltage in the preceding stage decays to $\approx 0 \text{ V}$ gradually by discharging. As the accumulated ion amounts have attained maximum concentration, the balanced voltage keeps at $\approx 0 \text{ V}$ afterward. In the 3rd stage, the ΔT is removed, and the external circuit is disconnected. As a result, the accumulated ions diffuse back to evenly distribute within the i-TE material. In the 4th stage, the external circuit is reconnected, and the electrons flow back to an electrically neutral state. An opposite-direction current compared with the 2nd stage is thus released, which leads to zero voltage.

Figure 9d shows the transformative evolution of voltage during a full charging/discharging cycle. The close loop indicate the repeatability of such a cycle, enabling i-TE materials with potential to be applied as long-term supercapacitors.^[92] The voltage decay in the 2nd stage is closely related to the resistance of the external load (Figure 9e). As the external resistance (R) increases, the voltage decay becomes slower. To explain such a phenomenon, the discharge time constant τ is defined, expressed as $\tau = RC$ (C is the capacitance of the i-TE capacitor).^[102] A higher τ arises from an increased R , which is equal to a slower voltage decay. The instantaneous decayed voltage is combined by a fast relaxation and a slow relaxation ($V_t = V_1 \cdot e^{-t/\tau_1} + V_2 \cdot e^{-t/\tau_2}$, where τ_1 is the fast relaxation time constant, V_1 is the fast relaxation initial voltage, τ_2 is the slow relaxation time constant, and V_2 is the slow relaxation initial

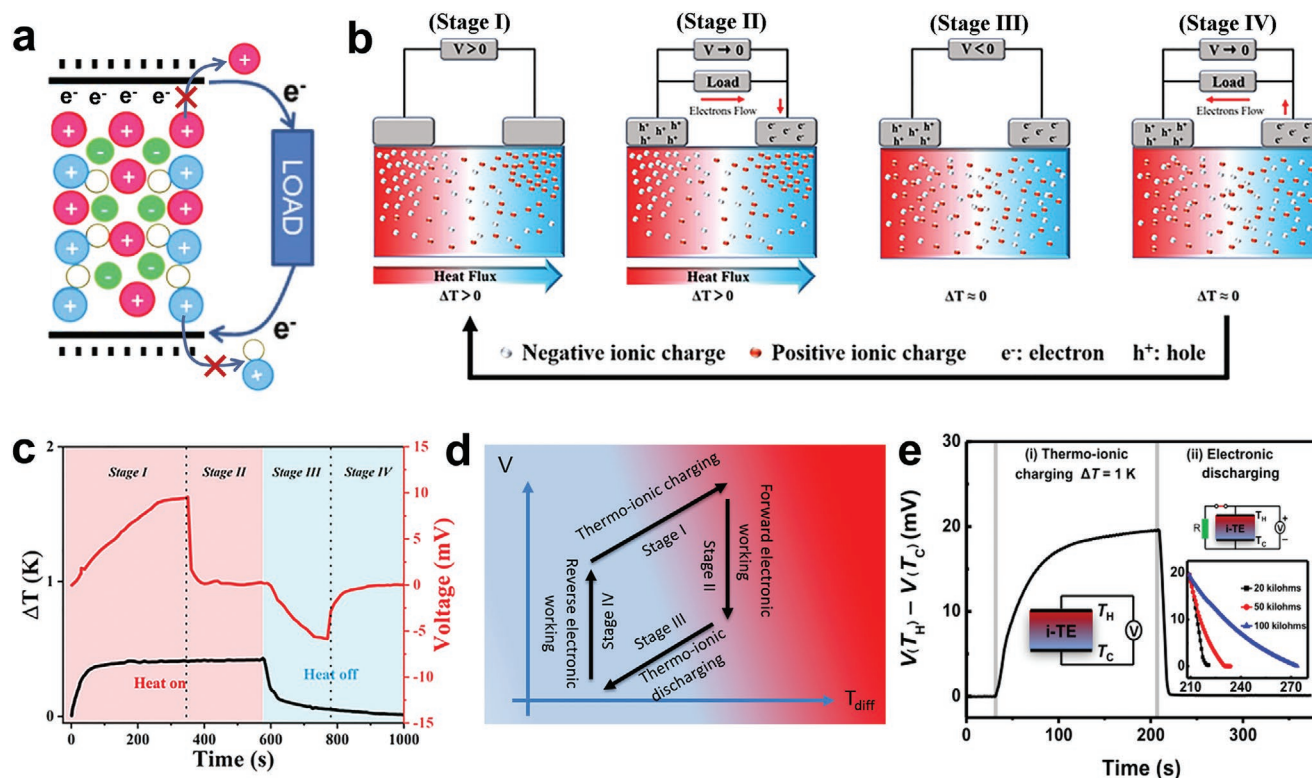


Figure 9. Schematic illustration of a) working mechanism of i-TE capacitance, and b) four stages of an i-TE capacitance cycle. c) Change of voltage and ΔT during the four-stage cycle. Reproduced with permission.^[94] Copyright 2021, American Chemical Society. d) Schematic voltage- ΔT cycle during the four-stage charge-discharge process. Reproduced with permission.^[14] Copyright 2019, Wiley-VCH. e) Charge-discharge process during stage I and II of a PVA hydrogel with external resistances of 20, 50, and 100 k Ω . Reproduced with permission.^[92] Copyright 2021, American Association for the Advancement of Science.

voltage). The decisive fast relaxation is related to the dielectric capacitive mode decay behavior. The slow relaxation originated from the decay between the electrodes and the i-TE materials.^[91]

The capacitance competence of an i-TE material is an intrinsic parameter of the whole system, which is primarily influenced by the design strategy. For instance, a solid supercapacitor with PSSH as electrolyte and polyaniline (PANI) deposited carbon nanotubes (CNTs) as electrodes was fabricated, achieving a considerable voltage of 38 mV and an advanced areal capacitance of 1200 F m⁻² when the driving force is barely a low-grade ΔT of 5 K.^[98] The supercapacitor was promised to work within a potential window range from 0 to 0.8 V. Moreover, a superior Columbic efficiency and stable capacitance are confirmed as well. Another instance is polyethylene oxide (PEO)/NaOH-based i-TE capacitor, which exhibits an extrapolated energy-storing density of 9.4 Wh kg⁻¹ at a ΔT of 10 K.^[101] For comparison, the homologous energy density of Li-polymer capacitors is ≈ 200 Wh kg⁻¹. By equaling the e-TE capacity to that of an identical extracapacitor connected with an e-TE material, an i-TE paper supercapacitor composed of PSSNa and NFC

performs three orders higher energy storage than Bi₂Te₃ at the same condition (the ΔT of 10 K).^[93]

4.4. Mechanical Performance

Mechanical properties, such as flexibility and stretchability, are important for i-TEs.^[120] Currently, i-TE materials with satisfactory mechanical properties have been intensively reported. For instance, a stretchability higher than 30% and Young's modulus higher than 0.60 MPa are demanded to meet the performance requirements of human skin.^[106,121] The PU/30 wt% IL ionogel with a mechanical stretchability of 300%, a tensile strength of 1.61 MPa, and a Young's modulus of 0.79 MPa were reported to be qualified as human skin devices.^[94] Figure 10a–c is optical photos of the i-TE ionogels, which visually display the stretchability and flexibility. As can be seen, well-designed ionogels and hydrogels can be twisted repeatedly (Figure 10a).^[102] High tensile strength can simultaneously enable the lift of a bucket of oil (Figure 10b).^[106] Besides, superior flexibility was reported to maintain (Figure 10c) even on the iced surface (-20 °C

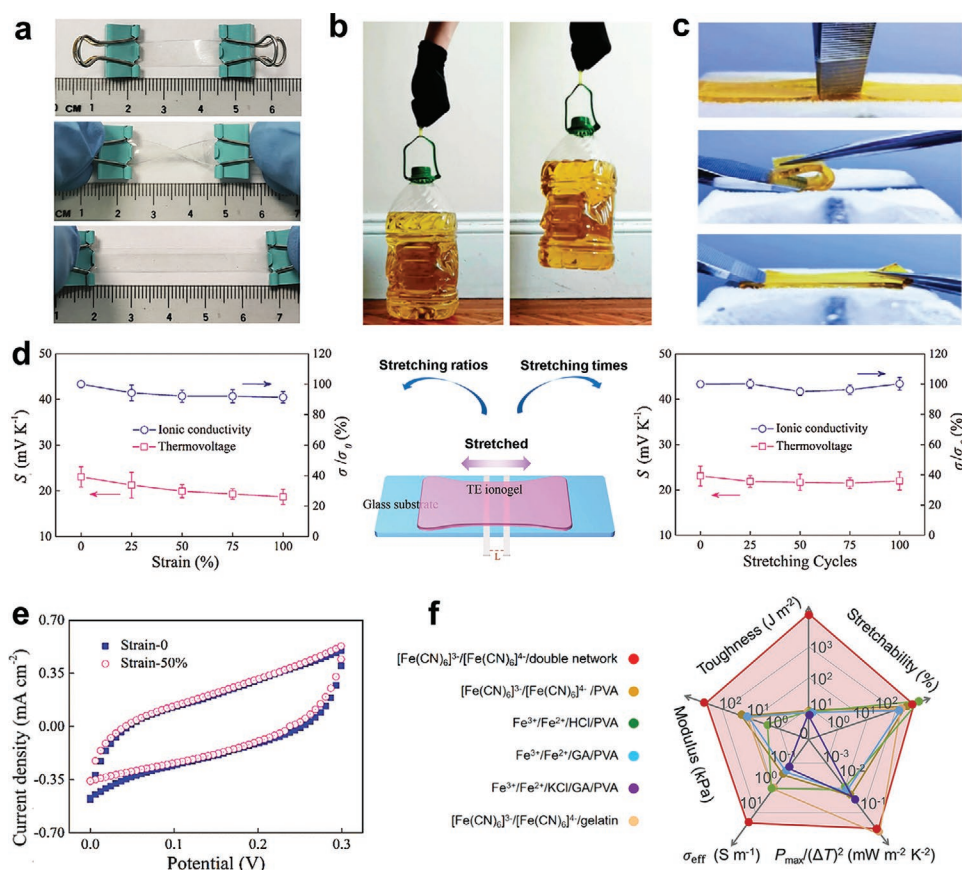


Figure 10. a) Photographs showing the stretched, relaxed, and twisted states of a waterborne polyurethane (WPU)/1-ethyl-3-methylimidazolium dicyanamide ([EMIM:DCA])-40% i-TE ionogel. Reproduced with permission.^[102] Copyright 2020, Wiley-VCH. b) A 4 mm width \times 2 mm thickness Fe(CN)₆³⁻/Fe(CN)₆⁴⁻/PVA i-TE hydrogel film can lift a 3200 g-weight bottle of oil. Reproduced with permission.^[106] Copyright 2022, American Chemical Society. c) Pressed, bent, and stretched states on an -20 °C iced surface of a synthesized i-TE organohydrogel. Reproduced with permission.^[121a] Copyright 2021, Wiley-VCH. d) Thermovoltage and relative ionic conductivity as functions of stretching ratios and stretching times of a WPU/[EMIM:DCA]-40% i-TE ionogels. e) CV curves at the original and 50% stretched states of a WPU/[EMIM:DCA]-40% i-TE ionogel. Reproduced with permission.^[102] Copyright 2020, Wiley-VCH. f) Comparison of Fe(CN)₆³⁻/Fe(CN)₆⁴⁻/PVA-based, Fe³⁺/Fe²⁺/PVA-based, high power density Fe(CN)₆³⁻/Fe(CN)₆⁴⁻/gelatin-based, and high mechanical toughness Fe(CN)₆³⁻/Fe(CN)₆⁴⁻/double network-based i-TE materials. Reproduced with permission.^[124] Copyright 2018, Cell Press.

atmosphere) for ionogels.^[121a] For polymer-based i-TE materials, their withstand temperature is mainly determined by the specific glass transition temperature (t_g).^[122] Recently, i-TE gels comprising polymer matrix (WPU) and ILs ([EMIM:DCA]) was reported with a high ZT value of 1.3 ± 0.2 with desirable stable during tensile deformation.^[102] Figure 10d presents the S and the relative conductivity (σ/σ_0 , where σ_0 represents the original σ without any stretching) of the i-TE ionogels. Specifically, the S value decreased from 23.1 to 18.7 mV K⁻¹ (81% maintained) while the relative conductivity was retained above 91% when the stretching ratio reached 100%. Moreover, both the S and the σ/σ_0 showed no obvious fluctuation during the repeatedly stretching and releasing of 100 times. The CV curves measured in the relax state and 50% stretched state are roughly overlapping as well, as illustrated in Figure 10e, indicating the potential of i-TE device serving in deformed environments.^[123]

However, current strategies to optimize mechanical properties mainly focus on modifying the matrix content, which usually in turn ruins TE properties. To overcome such a trade-off, double chemically cross-linked networks are introduced to i-TE materials. The improved cross-linking extent can boost the i-TE mechanical properties without increasing matrix contents. As shown in Figure 10f, a combination of 217% stretchability, 1.19 MPa tensile strength, 2770 J m⁻² toughness, and 0.61 mW m⁻² K⁻² output power density were reported in a Fe(CN)₆³⁻/Fe(CN)₆⁴⁻/double-network cross-linked copolymer ionogels.^[106] The consequently assembled device

works reliably even after slicing, which is meaningful to prevent the liquid-component leakage issues. Another breakthrough has been accomplished by a ternary-blend material of i) conjugated polymer of PANI, ii) nonconjugated anionic polyelectrolyte of poly(2-acrylamido-2-methyl-1-propanesulfonic acid) (PAAMPSA), and iii) phytic acid (PA).^[104] The obtained hybrid i-TE ionogel was intrinsically flexible in all directions with a stretching factor of up to $\approx 750\%$. Besides, the S was nearly unchanged after 30 cycles at 50% strain (from 7.2 to 6.8 mV K⁻¹).

4.5. Other Preferable Properties

I-TE materials favor other properties depending on working environment. First, self-healing behaviors have been reported in i-TE ionogels, which is of great benefit to promoting the service life and reducing maintenance intervals. Reversible bond plays an important role in self-healing materials. The self-healing abilities can be achieved by the dynamic breaking and reform of conjugate bond stackings, electrostatic attractions, hydrogen bonds.^[94,125] As illustrated in Figure 11a, freestanding ternary hybrids of PANI, PAAMPSA, and PA conceive the reversibility of electrostatic interactions and hydrogen bonds. The shaped composite film exhibits autonomous self-recovery ability without any external motivation such as pressure, wave, or heat. After a cutting and self-healing loop,

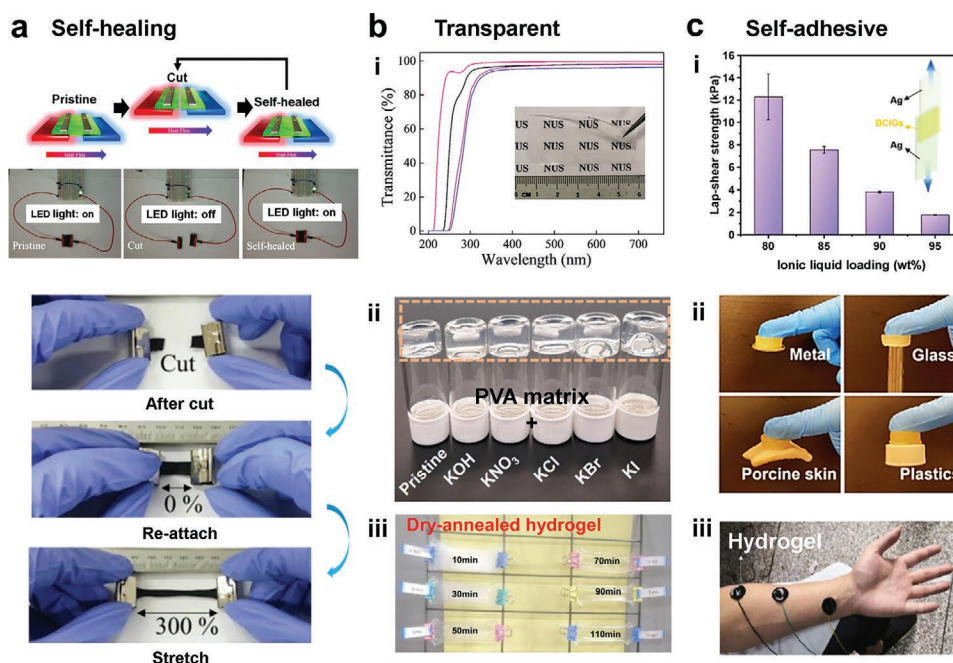


Figure 11. a) Photographs showing the self-healing behavior of polyaniline (PANI), poly(2-acrylamido-2-methyl-1-propanesulfonic acid) (PAAMPSA), and phytic acid (PA) ternary TE hybrid films. Reproduced with permission.^[104] Copyright 2020, Royal Society of Chemistry. b) i) The UV-vis transmittance spectrum of a WPU/[EMIM:DCA] i-TE ionogel film, ii) Photographs of PVA hydrogels containing KI, KBr, KCl, KNO₃, KOH, and pristine, iii) the pictures NaOH/PVA ionogels after freeze-thawing 24 h and dry-annealing 10, 30, 50, 70, 90, 110 min. Reproduced with permission.^[102] Copyright 2020, Wiley-VCH. Reproduced with permission.^[97] Copyright 2022, American Chemical Society. Reproduced with permission.^[92] Copyright 2021, American Association for the Advancement of Science. c) i) Lap-shear strengths of Ag plates by bacterial cellulose (BC)/[EMIM:DCA] i-TE ionogels, ii) photographs of poly(3,4-ethylenedioxythiophene) (PEDOT)/sulfonated lignin (LS)/polyacrylamide (PAM) hydrogels adhered to human arm. Reproduced with permission.^[69] Copyright 2021, Wiley-VCH. Reproduced with permission.^[127b] Copyright 2021, Royal Society of Chemistry. Reproduced with permission.^[128] Copyright 2020, Springer Nature.

σ of such i-TE hybrids can be recovered.^[104] Recently, self-healing, solution-processable, and 3D-printable i-TE generator has become a hotspot in this field. The constituent material is mixed composite of poly(3,4-ethylenedioxythiophene):poly(styrene sulfonate) PEDOT:PSS, healing agent nonionic surfactant (Triton X-100), and TE performance booster (DMSO). In the process of self-healing, the nonionic surfactant is interacted with PEDOT:PSS chains, which helps to fill the cutting cracks and reduce free volumes. Meanwhile, hydrogen bonds originating from ethylene-oxide groups of Triton X-100 endow the self-healing properties. More than 85% of the pristine power output can be reserved after ten times cutting and reattaching loops.^[90]

Second, different from traditional alloys with metallic glossy appearance (inorganic e-TE materials) and dark colored appearance conjugated polymer (organic e-TE materials), i-TE materials can be designed with a transparent appearance through blending transparent ion-donors (such as ILs or salts) and transparent matrixes (such as gelatin or amorphous polymer).^[126] As illustrated in Figure 11b, transparency of over 95% in the visible light range of a WPU/[EMIM:DCA] ionogel film can be achieved.^[102] PVA hydrogels containing KI, KBr, KCl, KNO₃, KOH also exhibit visually admiring transparency.^[97] Further regulation of transparency can be realized by controlling the crystallinity degree. For instance, i-TE hydrogels postprocessed

by freeze-thawing 24 h and dry-annealing 10, 30, 50, 70, 90, 110 min were reported with greatly increased transparency (see Figure 11b).^[92] This phenomenon is related to the crystallinity differences after post-treatments. Moreover, good compatibility between the components also contributes to increased transparency due to suppressed photon scattering.^[69]

Third, self-adhesive properties have also been reported. As shown in Figure 11c, ionogels composed of BC and [EMIM:DCA] are used as the adhesion to bond two layers of Ag plates.^[69] As the [EMIM:DCA] loading improves, the interfacial shear strength drops due to the lubricating effect of ILs. In another report, conducting hydrogels are modified to bond a wide variety of substrates, including metal, glass, porcine skin, and plastics.^[127] For practical application, a PEDOT-incorporated hydrogel has been pasted on the skin to detect the heart-beat signals.^[128]

5. I-TE Performance Optimization

In this section, we examine state-of-the-art strategies to optimize i-TE performance, which can be sorted as two classes: incorporation and structural optimization, as shown in Figure 12. Due to the integrated system nature of i-TE materials, the various factors should also be examined, including

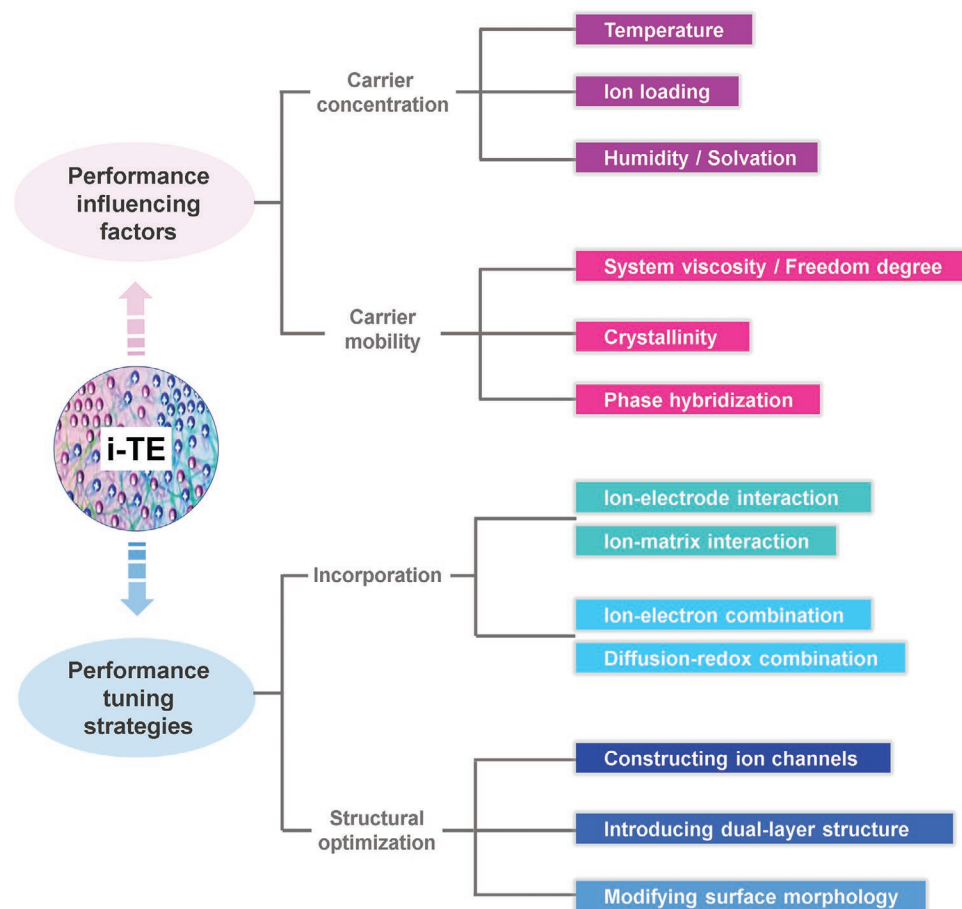


Figure 12. Flow chart of i-TE performance influencing factors and tuning strategies.

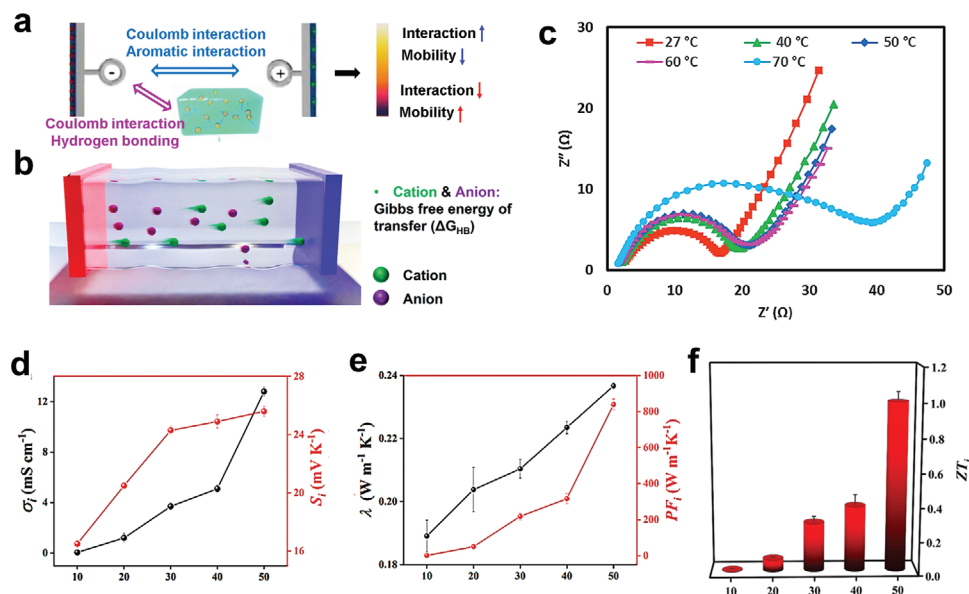


Figure 13. Schematic illustration of a) ion-electrode interactions, and b) ion-matrix interactions. Reproduced with permission.^[97] Copyright 2022, American Chemical Society. c) Nyquist impedance spectra of PEGDMA-[N₂₂₂₈]Br ionogel at 27, 40, 50, 60, and 70 °C. Reproduced with permission.^[132] Copyright 2019, Elsevier. Variations of d) σ and S , e) κ and PF, and f) ZT values of PU-[EMIM:DCA] i-TE ionogels as a function of ionic loadings. Reproduced with permission.^[94] Copyright 2021, American Chemical Society.

temperature, ion loading, and humidity, which are supposedly to have equal impact on anions and cations.^[2a,129]

5.1. Performance Influence Factors

Temperature mainly influences TE properties in two aspects: first, the statistical distribution of charge carriers and phonons, and therefore electrical and thermal properties are temperature dependent; second, the overall TE performance is based on the product of Z and T .^[130] As shown in **Figure 13a**, there are two dominant fettering forces of ions in i-TE materials: i) forces between ions and the electrodes via Coulomb interactions and aromatic interactions, and ii) forces between ions and the matrix that are basically composed of Coulomb interactions and hydrogen bonding. The migration of ion species therefore lies in overcoming these forces, i.e., a large enough ΔG to overgo the ion migration energy barrier, which usually decreases with increasing temperature (see **Figure 13b**). This has been profoundly confirmed by experiments,^[12,84c,131] for instance, in polyethylene glycol dimethacrylate (PEGDMA)/N,N,N-triethyl octyl ammonium bromide ([N₂₂₂₈]Br) i-TE ionogels (**Figure 13c**), a rise in temperature leads to decrease in resistance. The σ at room temperature was calculated to be 45.3 mS cm⁻¹, which linearly increases to a maximum of 74 mS cm⁻¹ at 70 °C.^[132]

Ion loading comprehensively influences i-TE properties, in analogy to e-TE materials. As plotted in **Figure 13d-f**, the σ , S , and κ of a PU/[EMIM:DCA] i-TE ionogel vary simultaneously with increasing ion concentration, leading to a $S^2\sigma$ of 850 W m⁻¹ K⁻¹ and a ZT of 0.99.^[94] Generally, an increasing ion concentration results in higher σ . However, an increased silver ion concentration was reported to cause obvious σ declines for Ag-Nafion polyelectrolytes.^[70] This is because the significantly decreased ion mobility arising from ion-ion scattering

contradicts the positive effects of increasing carrier concentration. While in the aspect of ionic S , a Debye-Hückel prediction based on the electrostatic interactions between ions provides theoretical reference, which derives a linear relationship between the Eastman entropy of transport and the square root of the ion loading.^[133] An experimental verification that agrees with such speculation has been reported, where the S decreases linearly with \sqrt{c} for tetradodecylammonium nitrate/octanol solutions.^[46a]

Humidity has primary impacts on kinetic transfer rate, which mainly influences i-TE materials working in generating mode, while is less important for i-TE materials working as capacitors.^[134] Under humid ambient environment, the linear-log plots of humidity versus σ and S are plotted in **Figure 14a,b**.^[81] As can be seen, the humidity- σ plots have unanimous trend although differing in orders of magnitude. By contrast, $|S|$ show both positive and negative correlations, which coincides with the water percolation channel theory. In 2018, via comparing $|S|$ of three different types of solid-state polyelectrolytes, the percolated pathway model of nonliquid i-TE materials was raised.^[16] As illustrated in **Figure 14c(i)**, interconnected water ion channels cannot be entirely established at low concentrations. While under sufficient humidity, two different situations are determined by the direction of water diffusion. If the water molecules and ions diffuse along the opposite direction, $|S|$ will be weakened with increasing relative humidity (**Figure 14c(ii)**). In this circumstance, the molar entropy of water transfer in the external environment is larger than that in internals, e.g., Nafion polymer membranes. On the flip side, if the water molecules and ions diffuse along a consistent direction, the S is escalated, such as in the S-PEEK film (**Figure 14c(iii)**).^[16,135]

It is hence promising to maintain high humidity for a better i-TE performance. Inspiration may come from a recent work, in which a self-humidifying bilayer cover sheet was devised by

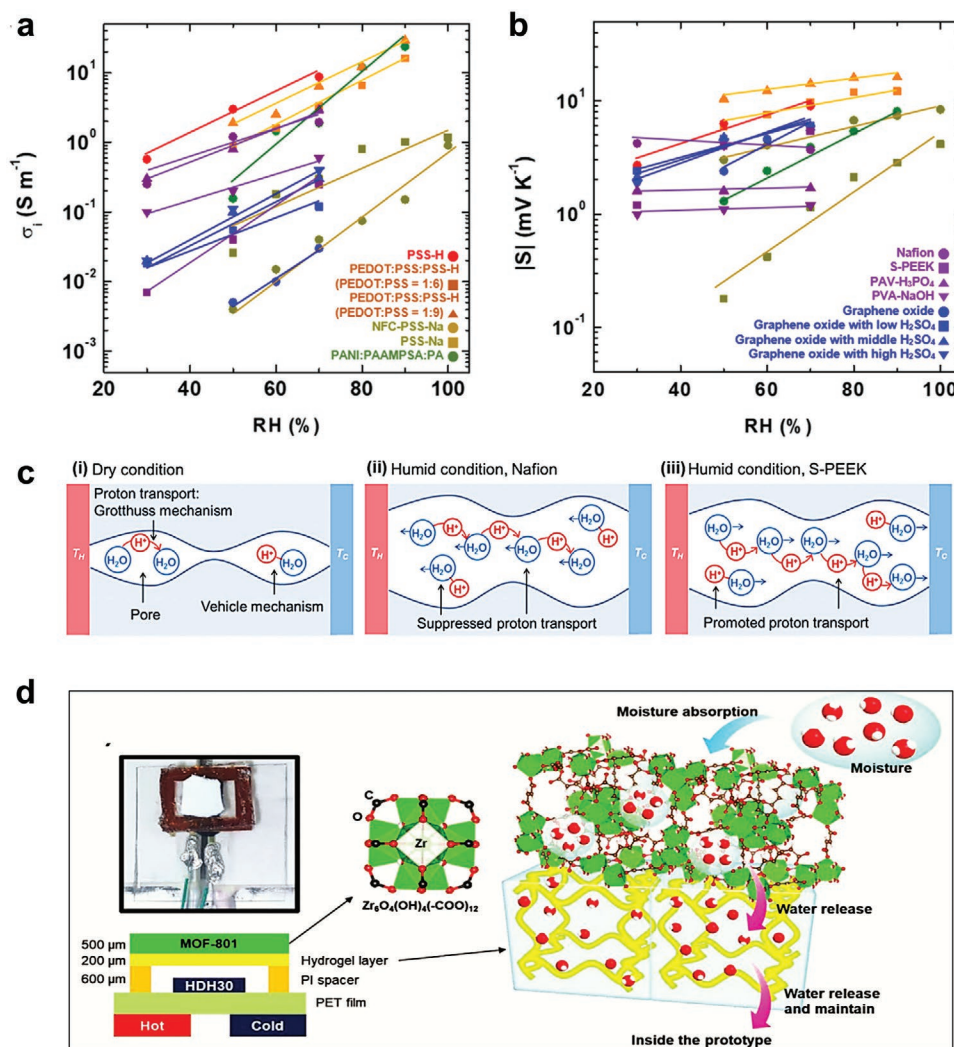


Figure 14. Humidity-dependent a) σ and b) S of the selected i-TE materials. Reproduced with permission.^[81] Copyright 2021, Elsevier. c) Schematic illustration of ion transport in dry and humid environments. Reproduced with permission.^[16] Copyright 2018, Elsevier. d) Photo and structural diagram of a self-humidifying bilayer sheet. Reproduced with permission.^[18] Copyright 2019, Wiley-VCH.

applying metal organic framework (MOF-801[®]) as the outer layer and hydrogel as the inner layer (Figure 14d).^[18] The MOF layer absorbs the moisture from the ambient and then delivers it to the hydrogel layer. Thus the humidity of the attached cavity was maintained where the i-TE materials are deposited.^[136] As a result, a humidity of 90% over 72 h can be provided, which is essential to fabricate stable and high-performance i-TE systems.

Viscosity is also related to i-TE performance, where low viscosity usually results in high ion mobility, or vice versa. Referring to Table 1, due to long side-chain alkyl groups increasing viscosity, ILs with [TFSI]⁻ show descending absolute S values of [EMIM:TFSI] > [BMIM:TFSI] > [HMIM:TFSI] > [OMIM:TFSI].^[69] By contrast, EG has the lowest viscosity and show ultrahigh σ due to the promoted ion mobility.^[91] Another factor needs to be taken into account is that viscosity is related with ion freedom. For instance, materials with high dielectric constant possess stronger charge bounding capability, which greatly decreases σ .^[92] Figure 15a shows the mesoporous structure with porous networks made of BC nanofibers. When ILs

flow through BC matrix, the swelling effect occurs, and the interval pores are expanded (Figure 15b). The schematic diagram in Figure 15c demonstrates the evolution of the gradient structures with a surface layer and an inner layer. As the IL loadings increase, corresponding pore diameters expand to greater spacing. Whereas in [EMIM:DCA] ILs, the surface layer is composed of the [DCA]⁻ by connecting to the hydroxyl of the BC matrix (Figure 15d). The small pore diameter prohibits the movement of cations, in analogy to what happens in Helmholtz electric double layer. With increasing pore diameter, the inner layer zone is disengaged to generate higher σ where ions or ion clusters can pass through near freely. The shrinking and the swelling states of BC/[EMIM:DCA] ionogels are referred to Figure 15e(i),(ii).^[69]

Crystallinity is another influence factor for especially polymer-based i-TE materials, which can be rationally modified through material engineering.^[137] On the one hand, strategies of annealing, cross-linking, and reducing the soft segment chain proportion can effectively regulate crystallinity.^[92,94] On the

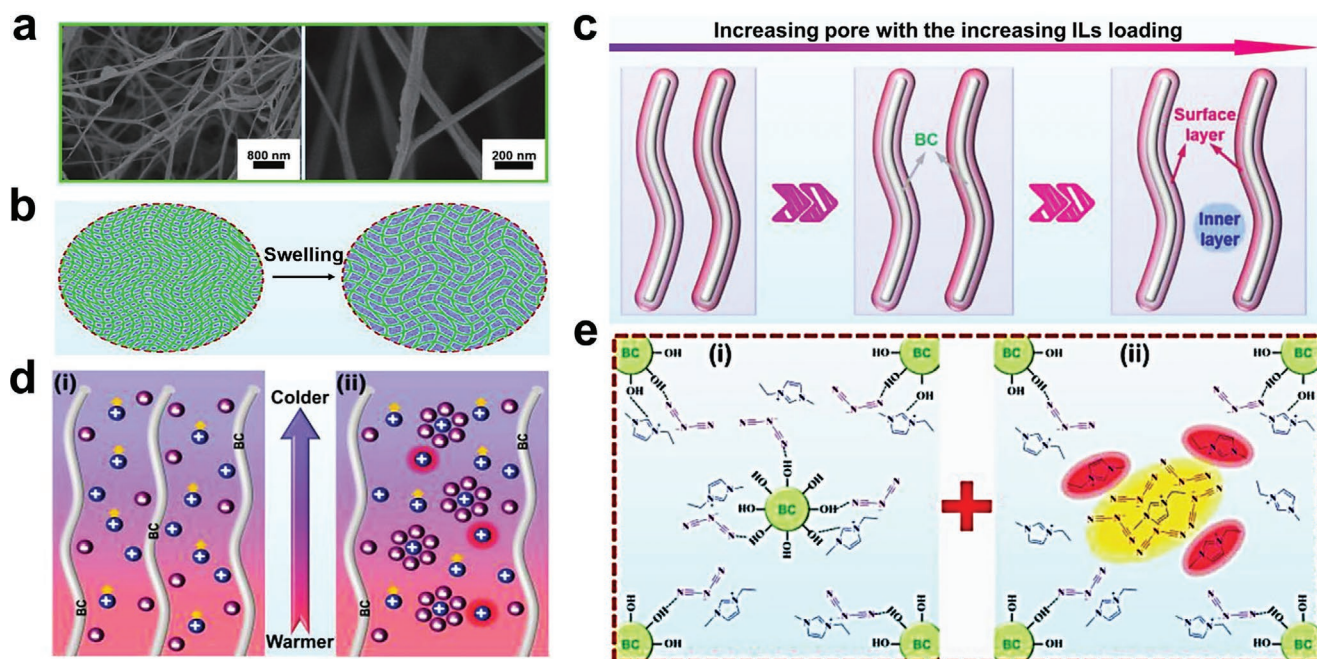


Figure 15. a) Scanning electron microscopy images of BC. b) Schematic illustration of the BC swelling with the increasing ILs loading. c) Structure evolution of the pores in BC with the increasing ILs loading. d) The ion diffusion of BC before and after swelling. e) Chemical structures of BC-[EMIM:DCA] ionogels under shrinking (left) and swelling (right) states. Reproduced with permission.^[69] Copyright 2021, Wiley-VCH.

other hand, the addition of antisolvent further refines the crystalline grain size. As shown in **Figure 16a**, grain refinement can be achieved by mixing an antisolvent into the acetone solution of the PVDF-HFP/[EMIM:DCA] i-TE system before the gelation step.^[19] The addition of ethanol, methanol, and isopropanol dramatically increases σ , which is yet observed in cosolvents of DMSO and DMF. Scanning electron microscopy (SEM) images in **Figure 16b,c** compare the morphology of the pristine PVDF-HFP/[EMIM:DCA]-50% ($m_{[EMIM:DCA]}:m_{[PVDF-HFP]} = 1:1$) ionogels and the PVDF-HFP/[EMIM:DCA]-50% ionogels post-treated with 10 wt% ethanol antisolvent. Obviously, antisolvent treatment results in network structures, which provide connecting points near which the grain size is refined. **Figure 16d** demonstrates the detailed procedure of how the addition of antisolvent refines grain size. i) The polymer chains are under stretched coil-like conformations in the original good solvent (acetone). ii) After evaporating acetone, large size pores are formed due to connection of the stretching conformational polymers, which are filled with ILs. iii) The stretched PVDF-HFP chains entangle into bundles due to the dipole-dipole interaction. Therefore, the thick polymer bunches fold into large grains at the network connection points. iv) Conversely, the stretched polymer chains contract gradually as the antisolvent addition. The formation of the thick polymer bundles is hindered as well. v) As a result, wispy solid networks are assembled by the contracted polymer chains. vi) Grain refinement is fulfilled.

Phase hybridization is an extensively adopted strategy for conducting polymer materials, which shows efficacy in tuning their thermal properties.^[138] As shown in **Figure 17a**, the κ of polymers and polymer composites depend on the phonon transport along continuous pathways.^[139] The existence of hetero-interfaces will scatter phonon transport pathways and there-

fore prohibit thermal transport. Although phonon scattering can happen within a homogeneous phase, such that between the crystalline segment and amorphous segment in semicrystalline polymers, it mainly arises from the phase boundaries in multiphase materials.^[140] As exhibited in **Figure 17b**, phase boundaries, inclusions, and pores can effectively scatter long-wavelength phonons, and a certain fraction of mid-wavelength phonons and short-wavelength phonons depending on their density-of-state.^[141] Nanoscale grain boundaries that tend to exist within the homogeneous phases mainly scatter mid-wavelength phonons, as well as short-wavelength phonons. Whereas point defects due to doping, atomic substitution, or vacancies contribute barely to short-wavelength phonon scatterings. **Figure 17c** provides the SEM images of BC/[EMIM:DCA], BC/[EMIM:TFSI], and BC/[EMIM:BF₄] ionogels. Obviously, micrometer-scale phase separation can be observed and certified, where a minimum κ of 0.186 W m⁻¹ K⁻¹ was obtained.^[69]

As i-TE materials are commonly multi-phase compounds with low κ (see **Table 2**), the optimization of κ has received less attentions. Since i-TE materials cover liquid, quasi solid, and solid multistates, where heat conduction mechanisms are completely different. Specifically, heterogeneous material composition, phase compatibility, fluid convection, and bulk conduction, can synergistically contribute to the κ of i-TE materials.^[142] The thermal performance regulation is deeply complex for i-TE materials, which has not been studied maturely till now.

5.2. Incorporation Approach

Modifying interaction relations has shown efficacy in optimizing i-TE performance. In what follows, four kinds of

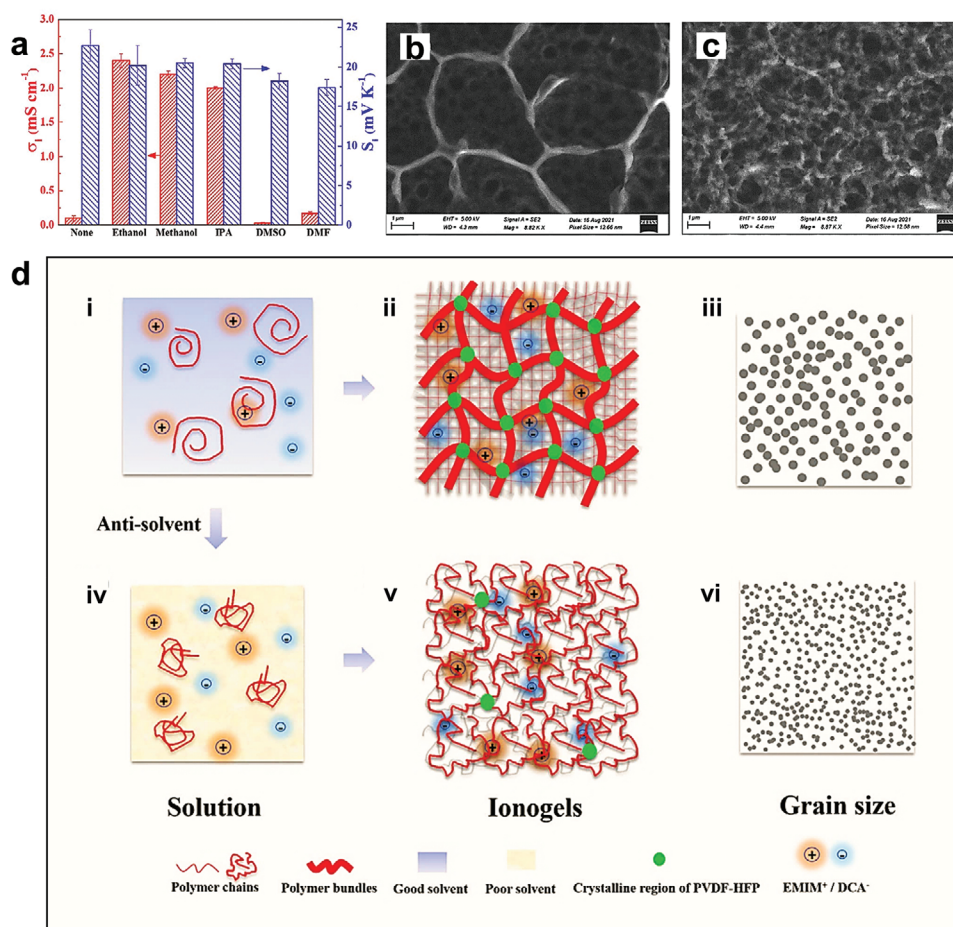


Figure 16. a) S and σ of the poly(vinylidene fluoride-co-hexafluoropropylene) (PVDF-HFP)/[EMIM:DCA]-50% ionogels prepared by adding different antisolvents prior to the ionogel formation. SEM image of the xerogel of b) pristine PVDF-HFP/[EMIM:DCA]-50%, and c) PVDF-HFP/[EMIM:DCA]-50% prepared by adding 10 wt% ethanol. d) Schematic illustration of the crystal formations and the polymer networks of pristine PVDF-HFP/[EMIM:DCA] ionogels and antisolvent treated PVDF-HFP/[EMIM:DCA] ionogels. Reproduced with permission.^[19] Copyright 2022, Wiley-VCH.

incorporation strategies are introduced, namely, ion–electrode interaction, ion–matrix interaction, ion–electron combination, and diffusion–redox combination.

5.2.1. Ion–Electrode Interaction

Given the straightforward correlation between i-TE S and concentration gradient difference from anions to cations under equilibrium, the adsorption–desorption of ions on the electrode surface plays an important role in generating thermovoltage.^[143] As shown in **Figure 18a**, modification of ILs leads to both n-type and p-type i-TE materials with gold sheets as electrodes.^[78] As summarized in **Figure 18b**, with common A4 paper adopted as the substrate, ILs of [OMIM:Ac], [EMIM:Ac], and [OMIM:Cl] behave p-type conductance, while [EMIM:BF₄], [EMIM:TFSI], and [OMIM:PF₆] exhibit n-type conductance despite of the trivial S . A schematic diagram of the adsorption–desorption effects is displayed in **Figure 18c**: [BF₄]⁻, [TFSI]⁻, and [PF₆]⁻ are unwieldy anions due to the large radius of F atoms. Thus, the intensive steric hindrance effect is beneficial to the anions desorption from the electrodes.^[144] As a result, cations

accumulate in priority around the cold electrode to raise positive S . On the contrary, anions of [Ac]⁻ and [Cl]⁻ are functional to coordinate with gold electrodes. The binding effect induces more anion aggregations on the electrode surface under equilibrium. In this regard, negative S can be generated. By connecting the n-type and p-type units in sequence, a 20-armed device supplies a voltage of 0.8 V at a ΔT of 35 °C (**Figure 18d**). These results confirm that the ion–electrode interaction can not only determine the conductance nature, but also change the magnitude of S . Additionally, according to the same i-TE material, the employment of different electrode materials strongly impacts the S .^[68]

5.2.2. Ion–Matrix Interaction

Ion–matrix interactions have been extensively adopted in optimizing i-TE performance, including the ion–dipole interaction,^[94] the ion–coordination interaction,^[92] and the hydrogen-bonding interaction.^[69] Specifically, ion–matrix interactions can be realized through three pathways.

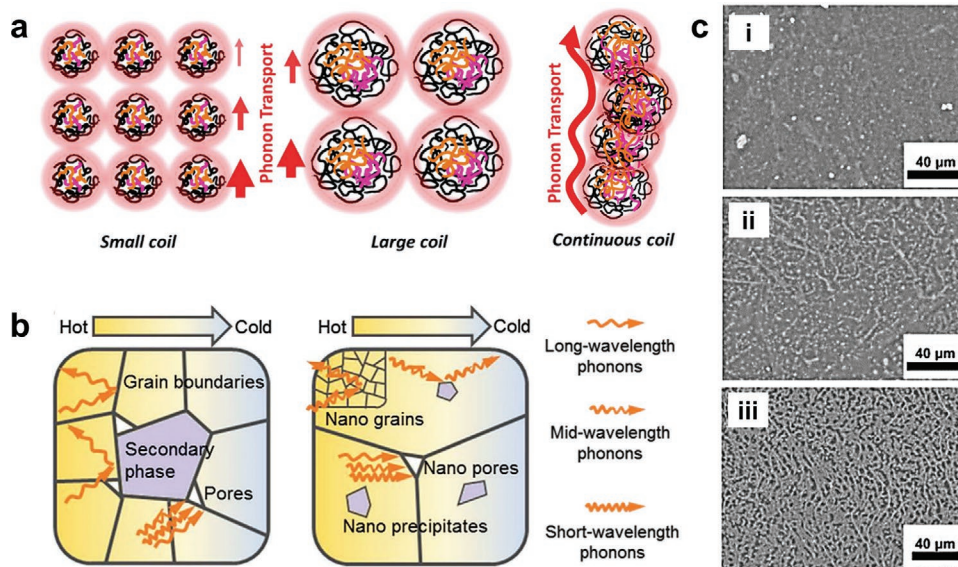


Figure 17. a) Phonon transport envisaging for small, large, and continuous coil polymers. Reproduced with permission.^[139] Copyright 2018, Elsevier. b) Comparison of phonon scattering centers between heterogeneous phases and homogeneous phases. Reproduced with permission.^[141] Copyright 2020, Wiley-VCH. c) SEM of (i) BC/[EMIM:DCA], (ii) BC/[EMIM:TFSI], and (iii) BC/[EMIM:BF₄] ionogels with the same IL loading of 90%. Reproduced with permission.^[69] Copyright 2021, Wiley-VCH.

i) Increase the concentration difference between anions and cations. In a PU/[EMIM:DCA] i-TE ionogel where the modified PU chains are functionalized with cationic imidazole side groups, the cationic imidazole groups attract and immobilize [EMIM]⁺ cations due to the ion–dipole interaction.^[94] As a re-

sult, a higher thermal diffusion efficiency of [DCA]⁻ anions can be obtained to generate an impressive S of 34.5 mV K⁻¹, which is 4.4-fold to pure [EMIM:DCA].

ii) Strengthen the ion dissociations. For instance, with adding inorganic salts (NaOH or NaCl) into PVA matrix films,

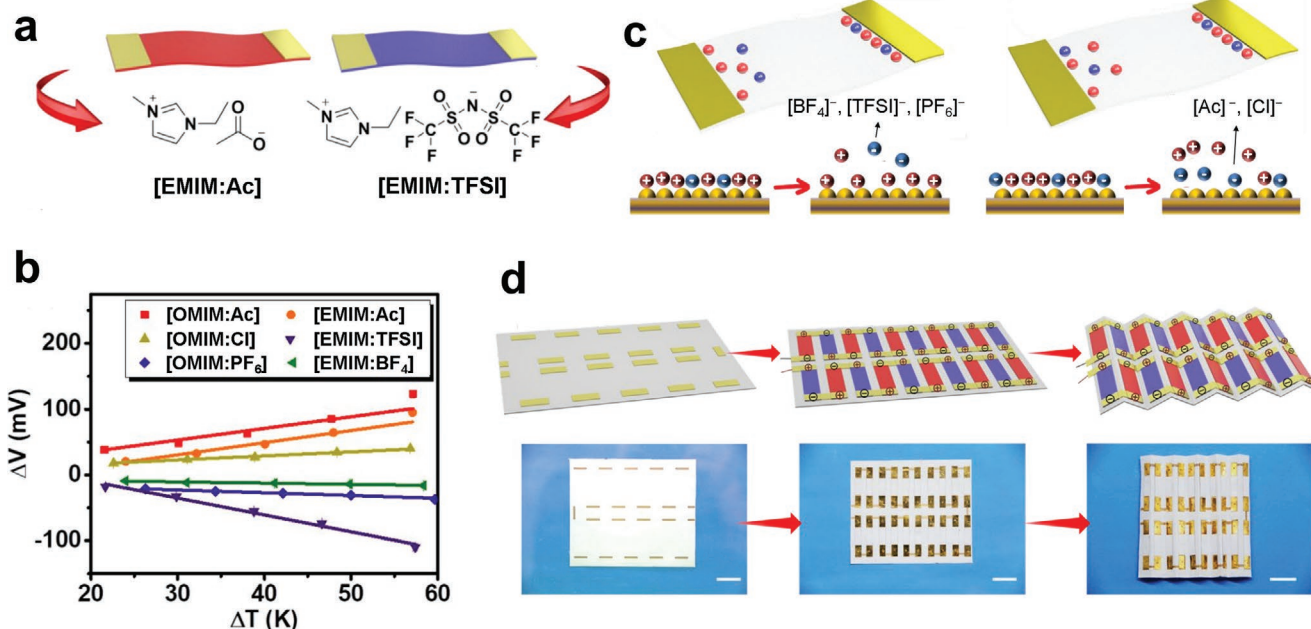


Figure 18. a) Schematic diagram of i-TE modules consisting of gold electrodes, A4 paper matrix, and ILs. b) Thermovoltage of the i-TE modules employing six different kinds of ILs. c) Schematic diagram of the adsorption–desorption effects on both p-type and n-type modules. d) Fabrication and foldability of a 20-armed i-TE device by in-order connection of the p-type and n-type modules. Reproduced with permission.^[78] Copyright 2020, American Chemical Society.

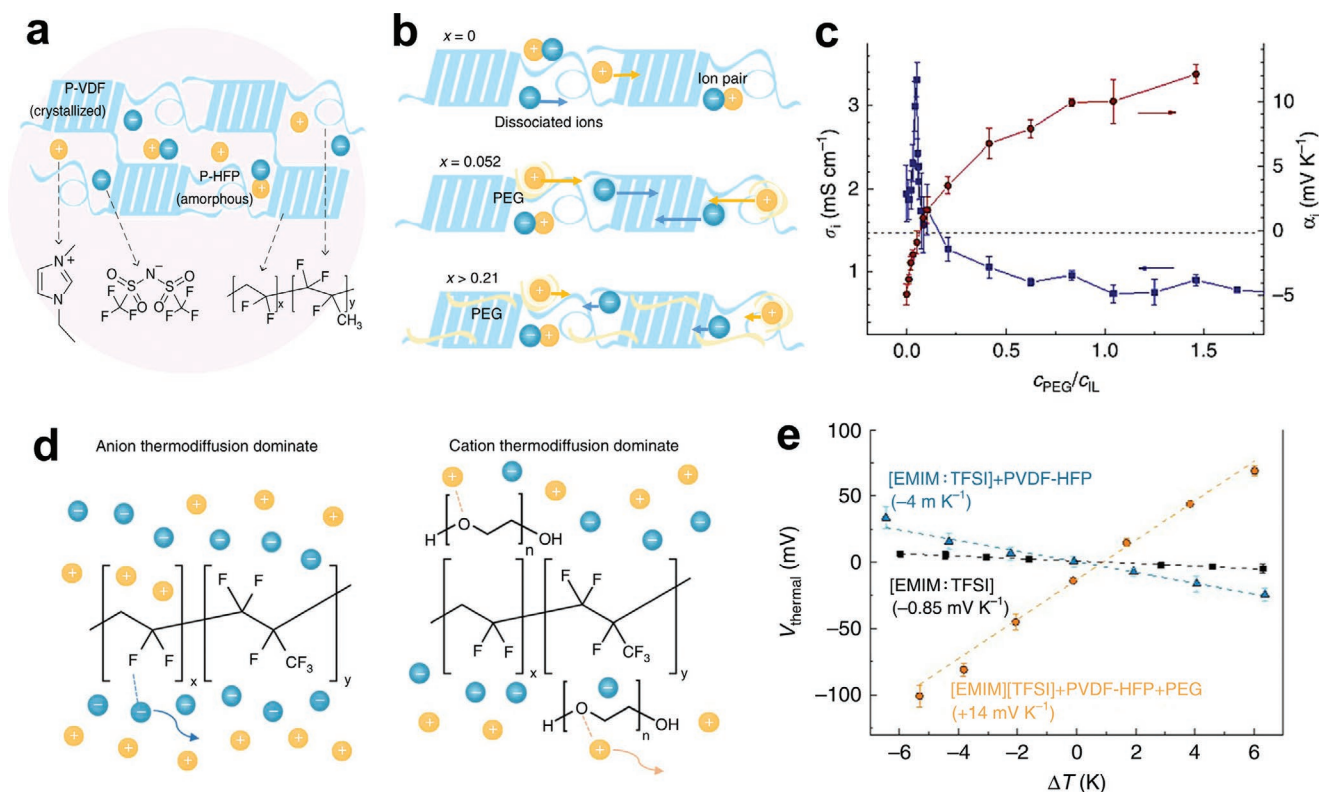


Figure 19. a) Composition and corresponding chemical structures of [EMIM:TFSI]/PVDF-HFP i-TE gels. b) Schematic diagram of the interaction between [EMIM:TFSI], PVDF-HFP, and polyethylene glycol (PEG). c) σ and S of [EMIM:TFSI]/PVDF-HFP/PEG as a function of the molar concentration ratio of $c_{\text{PEG}}/c_{\text{IL}}$. d) Schematic diagram of the ion transfer before and after PEG addition. e) V_{thermal} of pure [EMIM:TFSI], [EMIM:TFSI]/PVDF-HFP, and [EMIM:TFSI]/PVDF-HFP/PEG as a function of ΔT . Reproduced with permission.¹⁹⁹ Copyright 2019, Springer Nature.

the abundant hydroxyl groups of PVA coordinate with inorganic salt cations. Such coordination promotes the dissociation of the anion–cation pairs and improves the σ .^[92,145] Hydrogen bonding between PVA and the cations can greatly intensify the concentration gradient of anions in another PVA/NaI i-TE system, in which a record-high ionic S of 52.9 mV K⁻¹ was achieved and the ZT value can be calculated to be 5.18.^[97]

iii) Achieve p–n conversions. Several works highlighted the p–n conversions in i-TE materials mainly due to ion–matrix interactions.^[67,99,102] Figure 19a displays the material composition of a [EMIM:TFSI]/PVDF-HFP i-TE gel via chemical structures.^[99] As illustrated in Figure 19b, the addition of PEG promotes the dissociation of ILs due to ion-PEG coordination, leading to continuous raise of PEG fraction, which in turn hinders ion transport. As a result, the σ value increases first and decreases afterward, as shown in Figure 19c. As demonstrated in Figure 19d, the matrix of PVDF-HFP interacts with [TFSI]⁻ to provide anion pathways, resulting in negative S . With increase of PEG fraction, PEG interacts with [EMIM]⁺ via hydrogen bonding to provide cation pathways. Besides, the [TFSI]⁻ can be isolated from the PVDF-HFP chains by PEG, synergistically resulting in positive S (Figure 19e). Consequently, an 18-armed [EMIM:TFSI]/PVDF-HFP i-TE device exhibits an outstanding S of 0.333 V K⁻¹.

5.2.3. Ion–Electron Combination

The main shortcoming of i-TE materials is the insufficient σ . Therefore, a strategy of doping e-TE materials (which possess much higher σ) can be expected to compensate for the insufficient i-TE σ .^[146] As quantitative prediction of the σ of such an ion–electron combined system is still in controversies, here, we provide a brief discussion at the conceptual level.^[22] Taking a ternary hybrid i-TE material composed of PANI, PAAMPSPA, and PA system as an example (Figure 20a). PANI is a p-type conducting polymer e-TE material employing holes as carriers that have been widely known.^[147] PAAMPSPA is a polyelectrolyte i-TE material that is structured with H⁺ protons and SO₃²⁻ functional groups. PA is an inorganic acid that can replenish ionic carriers in the whole system. The combination of the three species thus reaches a maximum σ of 23.7 mS cm⁻¹, which is much higher than the individual σ of each phase.^[104] Another strategy has been reported for the embedding arrangement of graphene oxide (GO) in a PSSH solid electrolyte (Figure 20b–d).^[105] By repeatedly dropping–evaporating water solvent, GO tends to align in the way as per Figure 20b, leading to the establishment of continuous channels to foster the vehicular behavior of proton carriers (Figure 20c). As a result, the σ is remarkably increased to ≈ 115 mS cm⁻¹ and its ionic ZT value exceeded twice higher of 0.85 (namely, PSSH containing 3 wt% GO) compared with pure PSSH (Figure 20d). Besides, similar

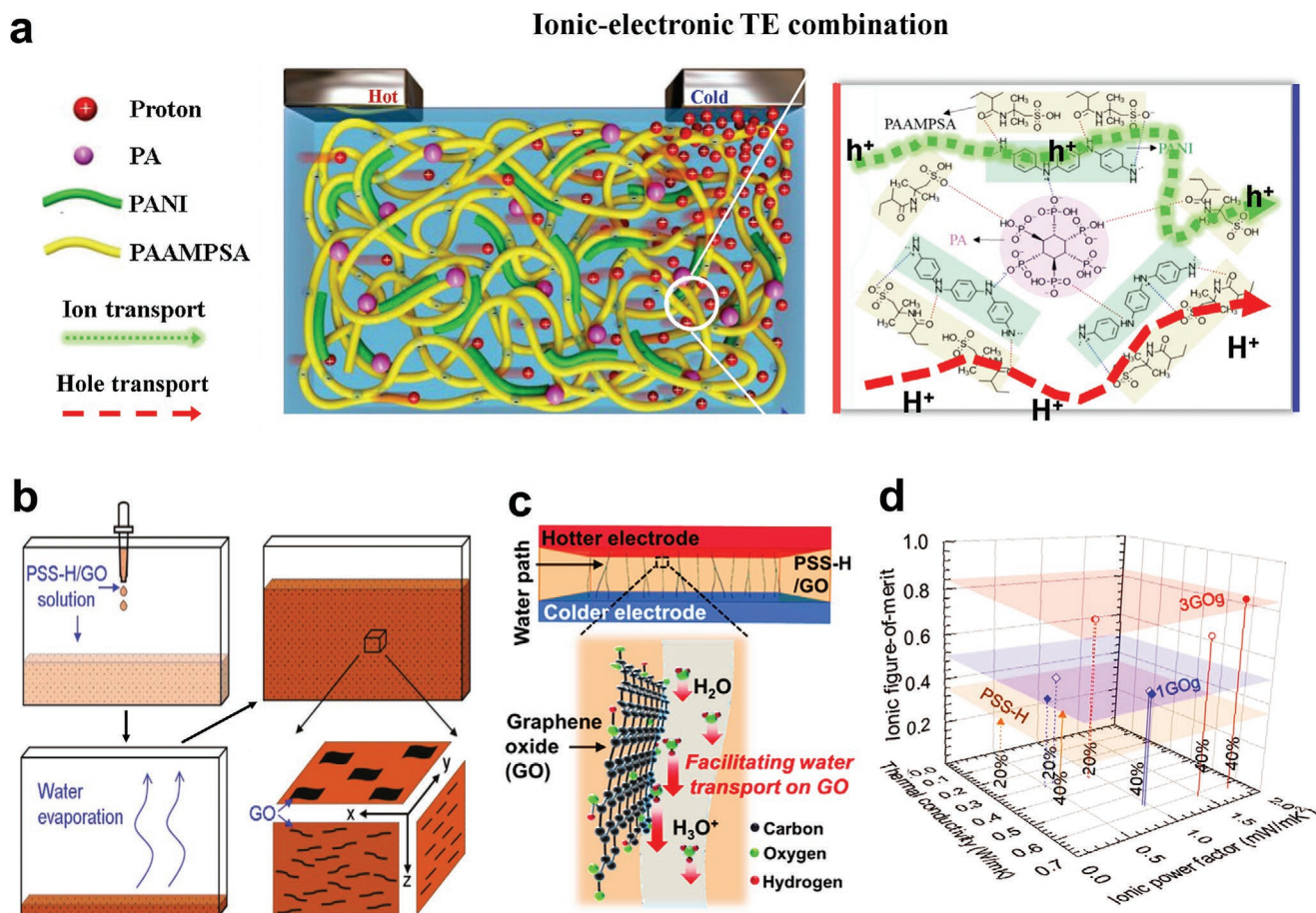


Figure 20. a) Schematic diagram of the composition and carrier pathways of the PANI/PAAMPSA/PA i-TE gels. Reproduced with permission.^[104] Copyright 2020, Royal Society of Chemistry. b) Schematic diagram showing the fabrication of the aligned GO/PSSH blending i-TE materials. c) Proton transport pathways provided by aligned GO. d) Stereogram showing ZT, κ , and $S^2\sigma$ for pure PSS-H (orange), PSS-H containing 1 wt% GO (blue), and PSS-H containing 3 wt% GO (red). Reproduced with permission.^[105] Copyright 2021, Wiley-VCH. Note: dotted and solid vertical lines represent 20 and 40 wt% water content, and hollow and solid icons indicate pure PSS-H/GO hybrid and PSS-H/GO/hydrogel hybrid, respectively. The synthesis of the hydrogel can be elaborated in the literature.^[105]

mixed ionic–electronic conducting effects in polymer/carbon TE materials were reported by other researchers.^[148]

5.2.4. Diffusion–Redox Combination

Unlike the ion–electron combination strategy which focuses on optimizing σ , the combination of ion diffusion and redox reactions mainly affects the S .^[15,21,81,149] According to the Onsager reciprocal relations,^[150] the synergistic S (S_T) can be expressed as the coupling of thermodiffusion and thermogalvanic factors^[21]

$$S_T = -\alpha_R + S_{td}(\text{redox couple}) + S_{td}(\text{ions}) + S_{td}(\text{matrix}) \quad (24)$$

where $-\alpha_R$ is the contribution of redox potential, S_{td} (redox couple) is the contribution of the thermodiffusion potential of the redox couples, S_{td} (ions) is the contribution of the thermodiffusion potential of the ionized ions, and S_{td} (matrix) is the contribution of the thermodiffusion potential of the matrix.

Recent efforts prepared a $\text{Fe}(\text{CN})^{4/3-}/\text{KCl}/\text{gelatin}$ i-TE system, as shown in Figure 21a.^[21] Figure 21b compares the S of the corresponding samples with individual TE effects and diffusion–redox combinations. Presumably, as-prepared $\text{Fe}(\text{CN})^{4/3-}/\text{KCl}/\text{gelatin}$ exhibits an overwhelming S in a range of 12.7–17 mV K⁻¹. The equivalent circuit diagram and fraction contribution to S_T is presented in Figure 21c. The S_T benefits maximally from the thermodiffusion of KCl (62.2%) while the redox potential of $\text{Fe}(\text{CN})^{4/3-}$ occupies a second proportion of 17.9%. Figure 21d–f explains the fundamental of the synergistic effect. At a given ΔT , KCl accumulates at the cold electrode to induce an electric field. This is caused by the thermodiffusion effect and the electric field is directional from the cold electrode to the hot electrode (Figure 21d). Regarding the thermogalvanic effect, oxidation reaction occurs at the hot end and a reduction reaction occurs at the cold end (Figure 21e). As a result, the hot electrode gains electrons to generate a lower chemical potential. The cold electrode loses electrons, and higher chemical potential is attained. Therefore, the thermogalvanic effect of the $\text{Fe}(\text{CN})^{4/3-}$ couple endows the same sign of electric field with

a Diffusion-redox TE combination

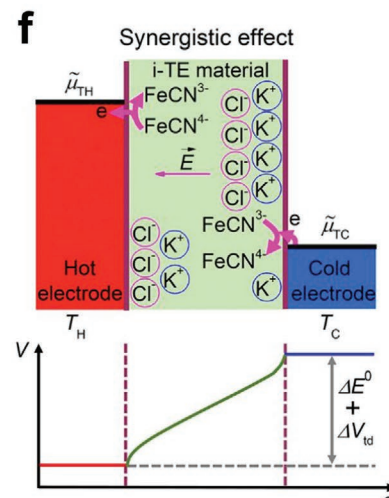
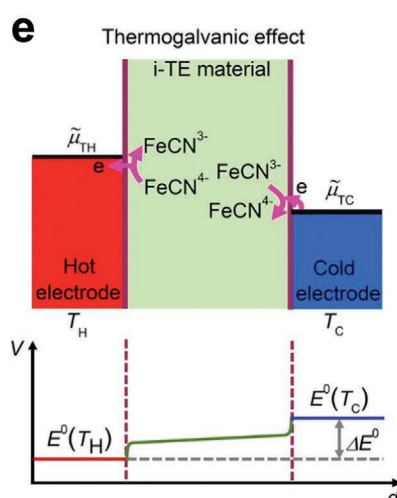
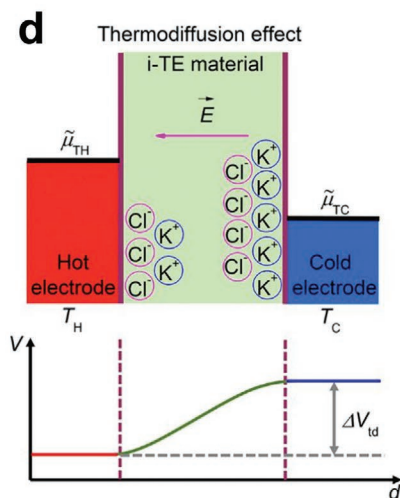
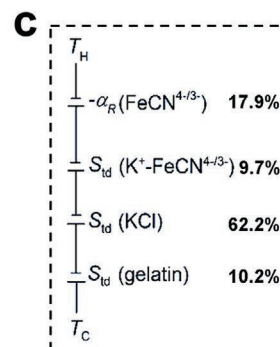
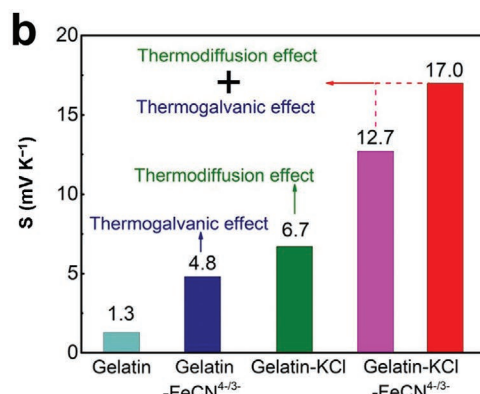
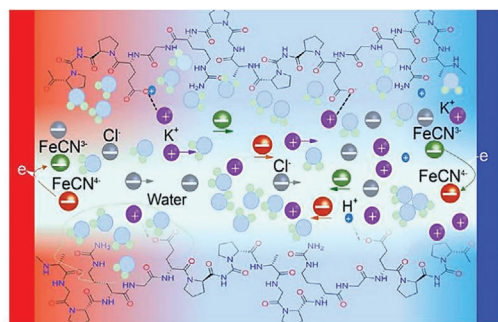


Figure 21. a) Schematic diagram of the thermodiffusion and thermogalvanic i-TE effects of a $\text{Fe(CN)}^{4-3-}/\text{KCl}/\text{gelatin}$ system. b) Comparison of the S of the pure gelatin, gelatin/ Fe(CN)^{4-3-} , gelatin/ KCl , and gelatin/ $\text{KCl}/\text{Fe(CN)}^{4-3-}$. c) The equivalent circuit diagram and the fraction contribution of every single part. Chemical potential (μ) diagrams of d) thermodiffusion effect of KCl , e) thermogalvanic effect of Fe(CN)^{4-3-} , and f) synergistic effect of the $\text{Fe(CN)}^{4-3-}/\text{KCl}/\text{gelatin}$ system. Reproduced with permission.^[21] Copyright 2020, American Association for the Advancement of Science.

that due to the thermodiffusion of the KCl ions (from the cold electrode to the hot electrode). Therefore, an increase of S can be achieved (Figure 21f).

5.3. Structural Optimization Approach

Structure engineering provides another scheme where i-TE performance can be effectively modified. Currently, structural engineering strategies include constructing ion channel, introducing dual layer structure, and modifying surface morphology, which will be discussed in detail.

5.3.1. Constructing Ion Channel

Artificially constructed ion transport channels can increase ion mobility, which has been verified in natural-wood-prepared cellulose matrix with intrinsically aligned structures as the ion carrier channels.^[151] As shown in the XRD spectrum of Figure 22a, the delignification treated cellulose exhibits excellent orientation alignments which is responsible for the clean elliptical pat-

tern. When electrolyte consisting of PEO, NaOH , and deionized water is added to the aligned cellulose, the ion transport channels are accordingly constructed, as illustrated in Figure 22b. The hydroxyl-rich PEO chains attached to the cellulose surface serve as an inner layer to promote the dissociation of NaOH . Meanwhile, the ionized OH^- anions from the salt link with plenty of hydroxyl groups via hydrogen bonds. In such a way, selective migration of Na^+ through the cellulose aisles can be realized, leading to an ultrahigh S of 24 mV K^{-1} .^[12] Saito et al. also reported a porous polypropylene membrane providing vertical linear channels for ion transfer.^[152] He et al. built ion pathways within the intervals of nanoparticle i-TE gels.^[20] Moriyasu et al. prepared a slide-ring cross-linked i-TE gel where the ions transport through non-networking regions.^[153] These cases imply that ion channel frames can effectively optimize i-TE performance.

5.3.2. Introducing Dual Layer Structure

A dual-layered structure composed of i-TE (PSS^-) and e-TE materials instead of the traditional one-layered mixture is

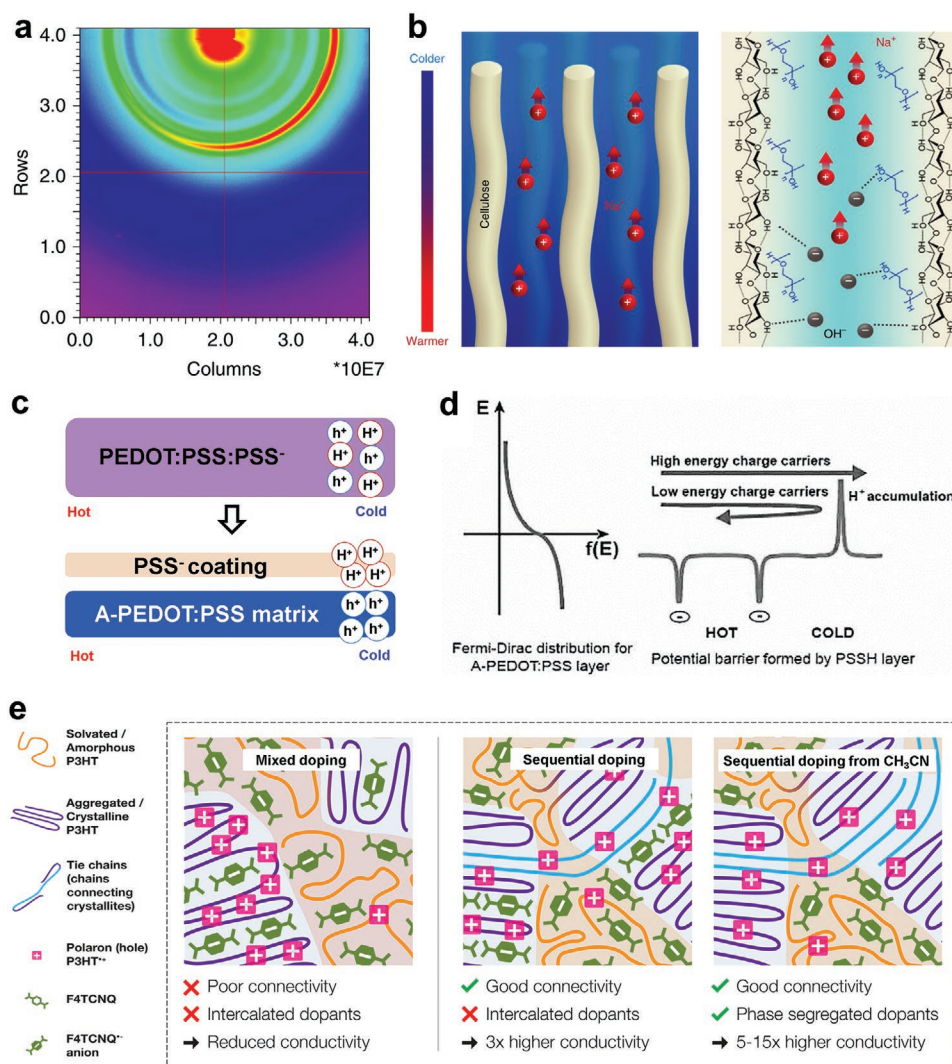
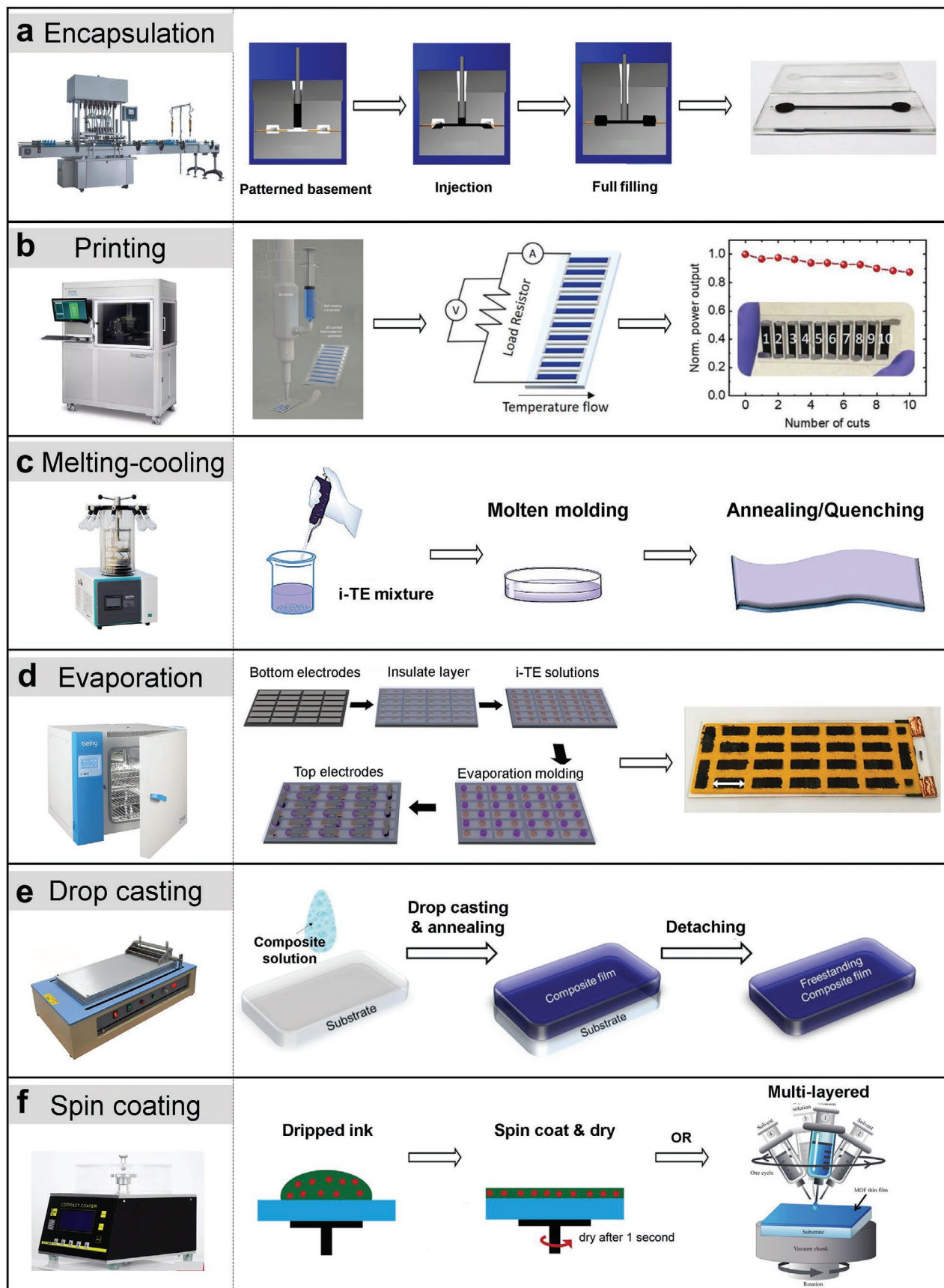


Figure 22. a) XRD pattern of the cellulose film infiltrated with NaOH. b) Schematic diagram of the aligned cellulose with selective ion transport and the corresponding chemical structures. Reproduced with permission.^[12] Copyright 2019, Springer Nature. c) Schematic diagram of carrier transports of PEDOT:PSS/PSS⁻ and PSS⁻ coated H₂SO₄ treated PEDOT:PSS (A-PEDOT:PSS) under a given ΔT . d) The demonstration of the energy filtering effects of PSSH/A-PEDOT:PSS (including the Fermi-Dirac distribution and the hole potential barrier at the A-PEDOT:PSS layer surface). Reproduced with permission.^[13] Copyright 2018, Royal Society of Chemistry. e) Dopant distribution and corresponding property characteristics of 2,3,5,6-tetrafluoro-7,7,8,8-tetracyanoquinodimethane (F4TCNQ) doped poly(3-hexylthiophene-2,5-diyl) (P3HT) film applying the sequential doping methods. Reproduced with permission.^[154] Copyright 2016, Royal Society of Chemistry.

shown in Figure 22c.^[13] The H₂SO₄-treated PEDOT:PSS (A-PEDOT:PSS) layer is the major component of the film and the PSSH layer was coated onto the A-PEDOT:PSS matrix as a functional layer. Ideally in this structure, protons flow along the PSS⁻ layer while holes flow along the A-PEDOT:PSS layer. However, as shown in Figure 22d, the accumulated protons in PSSH layer generate a same-sign potential with holes in the A-PEDOT:PSS layer. When the carriers pass through the interface between two layers, low-energy carriers can be filtered. As a result, the energy filtering effect based on the Soret effect is achieved by rational designation. A stable and continuous TE conversion can be obtained, and the measured $S^2\sigma$ of 401 $\mu\text{W m}^{-1} \text{K}^{-2}$ is several orders of magnitude higher than that of the monolayered PEDOT:PSS/PSS⁻ under 100% relative humidity.

5.3.3. Modifying Surface Morphology

Extensive results have been reported about the modification of film morphology via sequential doping.^[154] For instance, 2,3,5,6-tetrafluoro-7,7,8,8-tetracyanoquinodimethane (F4TCNQ)-doped poly(3-hexylthiophene-2,5-diyl) (P3HT) film, processed by a sequential solution, shows uniform nanoscale morphology and good connection between the amorphous phase and the crystalline phase (Figure 22e). Moreover, the method of selective sequential doping of acetonitrile (CH₃CN) leads to the exclusive distribution of F4TCNQ anions in amorphous domains. In this way, the resultant σ can be improved to 5–15 times higher (see Figure 22e). Although the article is not focused on the i-TE materials and the ionic conductivity, we noticed that the ion enrichment occurs by adopting sequential



doping, which provides a possible strategy for the ion pathway design. This is likely an inspiring reference for high-performance i-TE materials.

6. Molding

Although the materials design is essential that primarily determines the TE conversion efficiency, the subsequent molding process is also indispensable before TE device fabrications. In most cases, i-TE materials are pre-prepared into solutions and molding methods are analogous to the polymer e-TE materials including printing, drop casting, and spin-coating techniques.^[155] Besides, common methods of cooling and evaporation have been applied to shape the raw materials as well.^[156] In this section we will briefly introduce these molding methods in order.

6.1. Pretreatment

As has been discussed, i-TE materials can be classified into liquid state, quasi-solid state, and solid state. i) For i-TE liquids, encapsulations are directly applied for containment. ii) For quasi-solid gels, the existence of solvents permits satisfying fluxility and facile molding. Particularly, the chemical reaction of cross-linking often happens during gel forming as a unique process.^[156] iii) For solid state polyelectrolytes, solutions are commonly pre-prepared, where solvents can be removed after solution molding.

6.2. Molding Approach

Encapsulation approves the fixation of liquid and fragile i-TEs.^[157] As an important part to achieve encapsulation, materials of epoxy resin, organic silicon, glass tube, etc. have been used as the packaging basements to contain i-TE liquids.^[158] For instance, by predepositing electrodes and predesigning filling channels in the epoxy resin, ILs can be injected into the reserved channel via a needle tube. After full-filling, the injection cavity is sealed with glue or rubber. The encapsulated liquid i-TE materials are thus obtained for subsequent testing and device assembling, as shown in **Figure 23a**.

Printing process includes screen printing, 3D printing, inkjet printing, etc.^[78,90,99] Specifically, screen printing and inkjet printing are suitable for film manufacturing, while 3D printing can yield shaped bulks. In practice, the realization of printing extremely depends on the physical properties of the i-TE inks including melting point (T_m), viscosity, rheological behavior, density, solid particle size, and content.^[159] Regarding low T_m i-TE materials, 3D printing can be employed using pure i-TE inks. Whereas for dissolvable i-TE materials, screen printing and inkjet printing can be achieved by preparing i-TE solution inks. As shown in **Figure 23b**,

appropriately designed i-TE inks can be printed out as a target TE array according to the programmed pattern.^[90] Then, a preliminary i-TE device can be obtained after a simple electrode connecting process. The printing technique supports rapid and convenient fabrications, which enables scalable TE engineering at a low cost.

Melting-cooling technique can mold i-TE materials with thermoplastic matrix concisely and efficiently.^[160] For example, PEO, PEG, agarose, and gelatin gel are common matrix materials for i-TEs with a low T_m of around 87, -50 to 60, 70, and 25–35 °C, respectively.^[161] Notably, all of the above-mentioned T_m are lower than the boiling point of water (100 °C). Therefore, molding at a temperature higher than the matrix T_m cannot damage the component contents of the entire i-TE system containing water. As shown in **Figure 23c**, after the i-TE system is heated to a complete liquid state and defoamed, the resulted fluid can be poured into a mold with required shapes.^[94] Subsequently, both the annealing and quenching process can be employed for frozen settings. Possible postprocessing procedures can be applied afterward according to the material designation.

Evaporation is a low-cost and simple-operated molding technique, where the required equipment can be simplified to merely an oven.^[12,69,99] Pre-preparation of dilute solution or cosolution is necessary to provide sufficient fluidity. As shown in **Figure 23d**, certain molds are required for supporting or clamping the pre-prepared solutions. Then the excess solvent or cosolvent can be evaporated under gas blowing or heating conditions. Herein, the heating process and the corresponding temperature play an important role in the obtained i-TE structure. When the top and bottom electrodes are attached, a facile i-TE device can be obtained.

Drop casting technique has been widely applied in the molding of polyelectrolyte type i-TE materials.^[91,102] The methods of drop casting and evaporation are analogous, but the main difference exists where drop casting is more fitness for fabricating films. Furthermore, compared with spin-coating technology (which will be discussed afterward), drop casting technology can maintain the uniformity of solid particles contained i-TE materials. **Figure 23e** is a typical drop casting progress sketch. First, the i-TE solution is dropped onto the substrate such as silicon wafer, quartz, or release film, which is pre-cleaned by detergent, organic solvents, or plasma.^[162] Then vacuum drying at an inert gas atmosphere will be conducted to output aimed casting films. Freestanding i-TE films can be obtained after peeling off from the substrate. On some occasions, the i-TE film deposited substrates can be directly applied to assemble i-TE devices. Nevertheless, both evaporation and drop casting technology are relatively time-consuming due to the long-term drying process.

Spin-coating is another solution-based technique apart from evaporation and drop casting. As spin-coating technology relies on the centrifugal force for drying, the i-TE ink is required to be uniform without possible centrifugal force derived enrichments. As displayed in **Figure 23f**, i-TE inks are dropped

Figure 23. Schematic diagrams for i-TE molding processes. a) Encapsulation. Reproduced with permission.^[68] Copyright 2016, Wiley-VCH. b) Printing. Reproduced with permission.^[90] Copyright 2019, Wiley-VCH. c) Melting-cooling. Reproduced with permission.^[94] Copyright 2021, American Chemical Society. d) Evaporation. Reproduced with permission.^[99] Copyright 2019, Springer Nature. e) Drop casting. Reproduced with permission.^[90] Copyright 2019, Wiley-VCH. f) Spin-coating. Reproduced with permission.^[164] Copyright 2016, American Chemical Society.

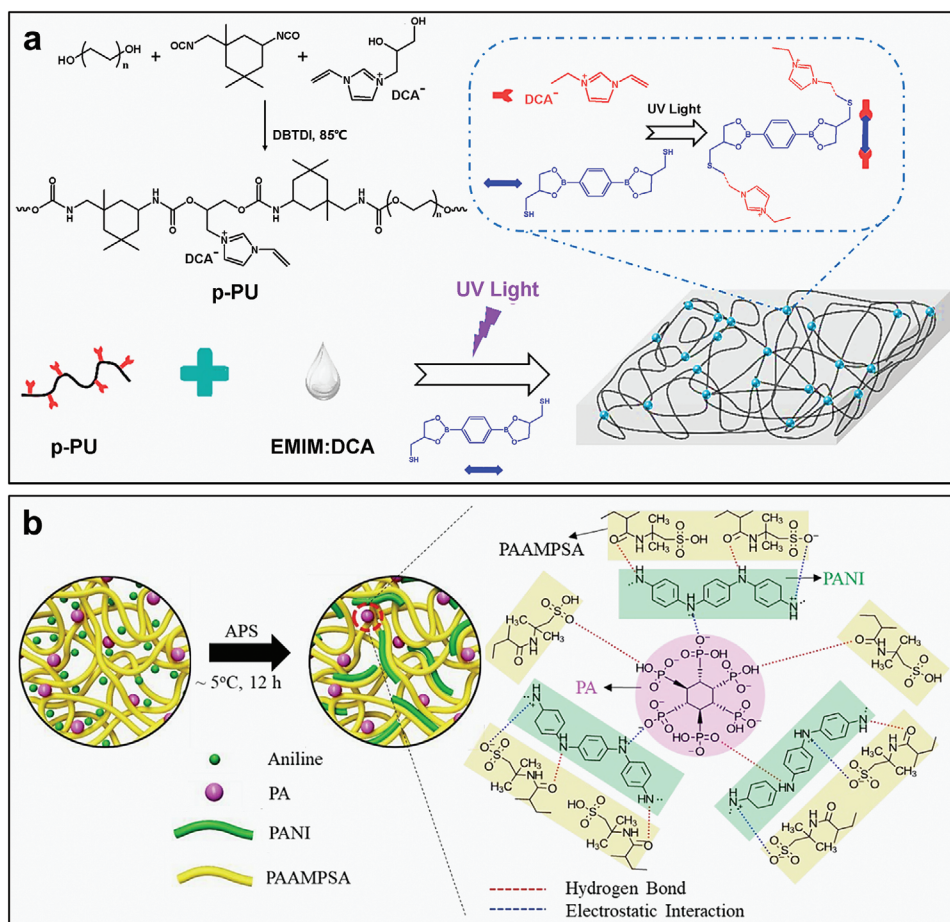


Figure 24. Schematic diagrams of a) preparation routine of cross-linked PU/[EMIM:DCA] ionogel. Reproduced with permission.^[94] Copyright 2021, American Chemical Society. b) The physical cross-links consisted of hydrogen bonds and electrostatic interactions within the PANI/PAAMPSA/PA ionogel. Reproduced with permission.^[104] Copyright 2020, Royal Society of Chemistry.

to the center of the platform (covered with substrate) with stationary or low speed spinning. Afterward the platform will be rotated rapidly to spread the i-TE drop and shake off the excessive solvents.^[163] Layered films can be obtained by repeated spin-coating whereas the amount of layer cannot be indefinitely increased. This is because each spin-coating process will introduce solvent to destroy the layer structure.^[19,94,131]

6.3. Potential Chemical Reaction during Molding–Cross-Linking

Unlike common molding processes, some i-TE materials, especially ionogels and hydrogels, exclusive chemical reactions of cross-linking are required to solidify the raw fluid materials. Practically, gels are a kind of network structured materials where polymer chains are cross-linked to each other.^[165] The cross-linking process ensures the solid form of the gels, which is also known as cure molding.^[166] There are mainly two kinds of cross-linking pathways: via chemical covalent bonds, or via physical supramolecular structures (including van der Waals forces, hydrogen bonds, and ionic bonds).^[167]

Figure 24a illustrates the synthesis of homopolymeric polyurethane p-PU.^[94] As can be seen, p-PU liner chains were

designed with side groups containing double bonds. Then these double bonds reacted with thiols under UV light where chemical cross-linking forms. During the UV irradiation, ILs were added to the solution, which brings more evenly dispersion. Experimental results verify the conclusion that chemical cross-linking promotes thermal/dimensional stability and prevents the leakage of ILs from the i-TE gels.^[94,132] **Figure 24b** demonstrates an example of multiple physical cross-linked i-TE gels.^[104] The whole system contained components of PANI, PAAMPSA, and PA. Abundant amino groups, carbonyl groups, organic acids, and inorganic acids in the system are assembled with hydrogen bonds and electrostatic interactions between each other. As a result, an integral network with regenerative dynamic characteristics was formed as the matrix. In this way, sufficient mechanical strength is endowed.

7. I-TE Device Design and Application

In this section, we examine the feasibility of making i-TE materials into applicable devices, with a highlight on basic design principles, key integration technologies, and performance optimization methods.^[168] Specifically, we start with a description

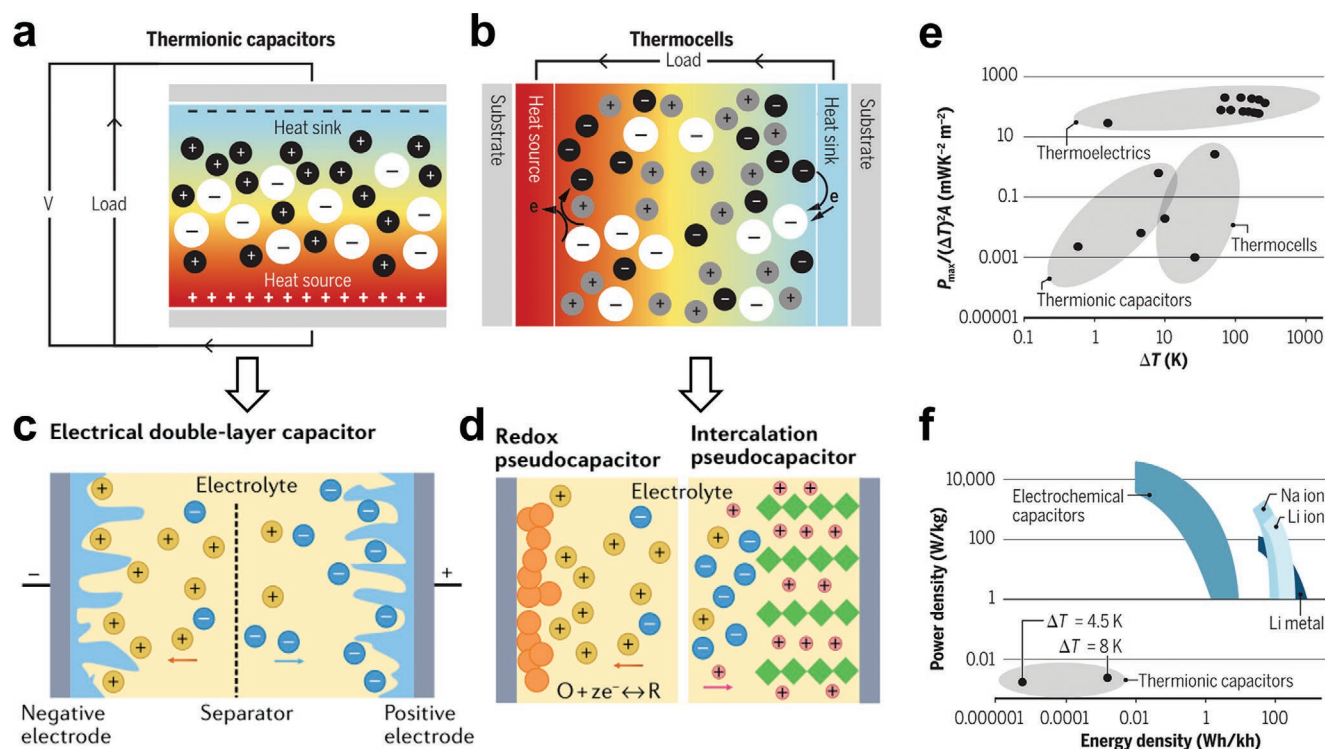


Figure 25. Schematic diagrams of the a) i-TE thermocapacitor, b) i-TE thermocell, c) typical electric double-layer supercapacitor, and d) typical pseudocapacitor. Reproduced with permission.^[26] Copyright 2021, American Association for the Advancement of Science. Reproduced with permission.^[172] Copyright 2022, Springer Nature. e) Comparison chart of the normalized maximum instantaneous power density $P_{\max}A^{-1}\Delta T^{-2}$ as a function of ΔT , and f) plots of power density versus energy density. Reproduced with permission.^[26] Copyright 2021, American Association for the Advancement of Science.

of comprehensive i-TE device characteristics and unique performance features. To fabricate i-TE modules, the structure and composition of typical devices are discussed. After that, several advanced electrode materials are introduced, which play significant roles in the capacitance of i-TEs. Subsequently, we summarize four prevalent working modes (i-TE capacitor mode based on the thermodiffusion effect, i-TE capacitor mode based on the thermogalvanic effect, i-TE generator mode based on the thermodiffusion effect, and i-TE generator mode based on the thermogalvanic effect) of the i-TE devices on the basis of distinguished power supply curves. In the end, practical examples of state-of-art i-TE capacitors, generators, and sensors are overviewed, respectively.

7.1. Comprehensive Characteristics and Performance Specialness

The most considerable advantage of i-TE materials is the large ionic S , which is commonly more than 50 times higher than that of commercial Bi_2Te_3 ($\approx 190 \mu\text{V K}^{-1}$).^[101] As a thermal-to-electrical conversion device, this is of great significance in recycling low-grade waste heat. On the one hand, i-TE devices generate higher thermovoltage under unit ΔT . On the other hand, owing to the low κ of i-TE materials, preferable ΔT can be established even across a film thickness of a few tens of micrometers.^[99] As a result, i-TE materials are usually featured with a high S/κ ratio which is more than 100 times compared

with that of e-TE materials, making i-TE devices capable for working as high-resolution temperature sensors,^[169] e-skin that directly powers the IoT.^[170]

As shown in **Figure 25a,b**, although all i-TE devices generally transform ΔT into ΔV under a power generation mode, the detailed working mode of thermodiffusive and thermogalvanic i-TE devices are different, where the former works as intermittent thermocapacitors, while the latter works as continuous thermocells.^[26,171] From the electronic capacitance perspective, thermocapacitors are analogous to the electric double-layer supercapacitor, while thermocells are analogous to the pseudocapacitive supercapacitor as shown in **Figure 25c,d**.^[172]

The performance of TE devices is usually evaluated by the parameter of normalized maximum instantaneous power density $P_{\max}A^{-1}\Delta T^{-2}$, where P_{\max} is the maximum output power and A is the cross-sectional area. Moreover, regular capacitors are assessed by the parameters of power density, which is apportioned performances over a period of time. As shown in **Figure 25e**, i-TE thermocells and thermocapacitors behave at much lower $P_{\max}A^{-1}\Delta T^{-2}$ compared with e-TE devices mainly due to large internal resistances. Whereas **Figure 25f** indicates that there are significant gaps for i-TE thermocapacitors to be comparable with commercial capacitors and batteries. These comparisons show the great potential of decreasing the internal resistance of i-TE devices. Nevertheless, the inferior energy/power density is roughly tolerable in the case of TE materials are exploited to utilize the waste heat which will otherwise be discarded to the surroundings.^[26]

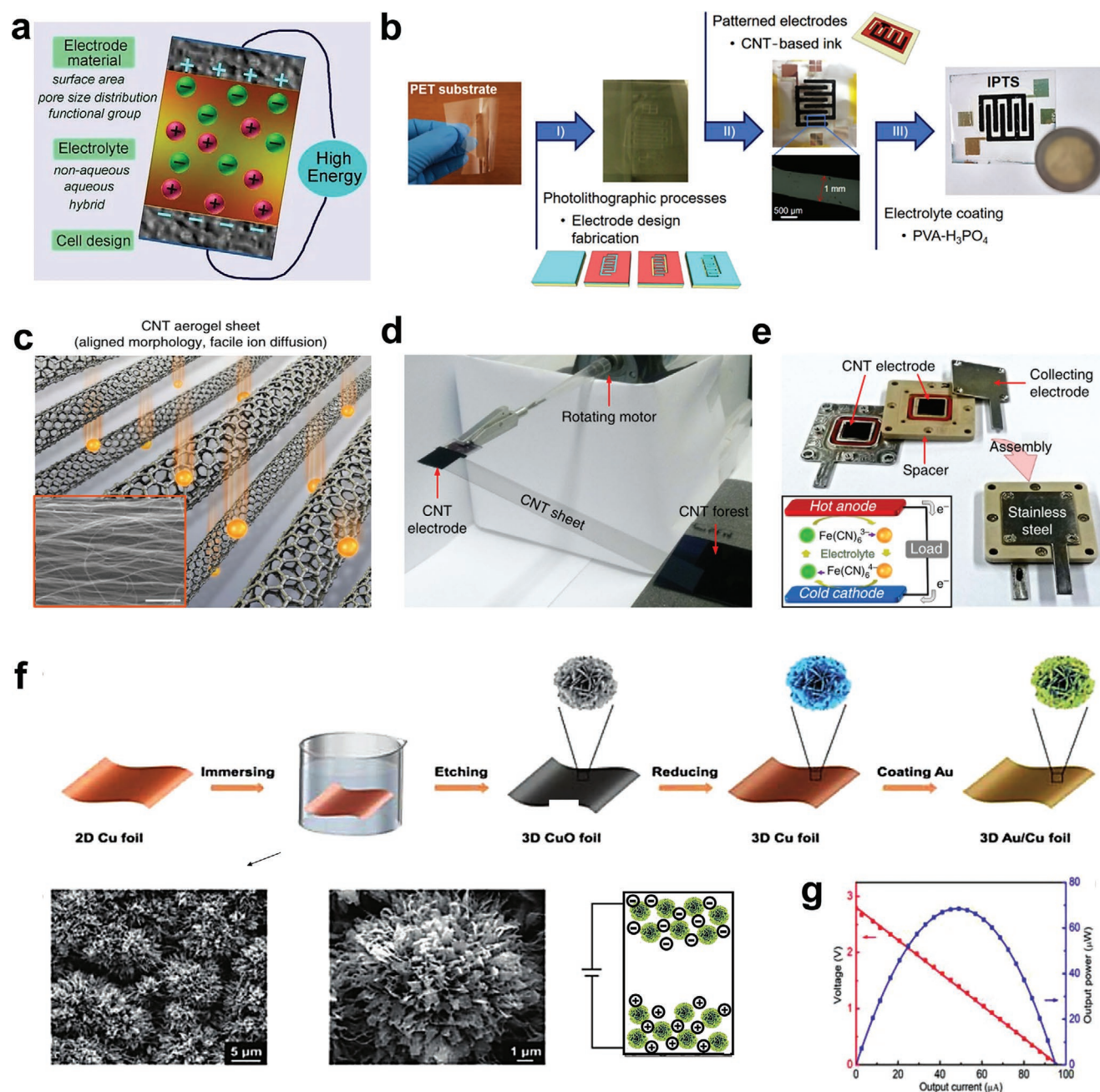


Figure 26. a) Typical i-TE device composition. b) Fabrication of the PVA/H₃PO₄ i-TE device with MWCNT electrodes: (I) photolithographic process of the designed electrode pattern, (II) electrode fabrication by fulfilling MWCNT inks to the designed pattern, and (III) device fabrication by depositing PVA/H₃PO₄ gel between two pieces of patterned electrodes. Reproduced with permission.^[175] Copyright 2021, American Chemical Society. c) SEM image of the aligned CNT aerogel. d) Process of continuous reeling off CNT aerogel sheets from a CNT forest, and wrapping it around a metal shaft to obtain planar electrodes. e) Photographs of a CNT sandwiched Fe(CN)₆³⁻/Fe(CN)₆⁴⁻ thermocell with the schematic drawing inset. Reproduced with permission.^[176] Copyright 2016, Springer Nature. f) Preparation process and morphology of the 3D hierarchical Au/Cu foil electrodes with microflower-like morphology. g) Voltage and output power as a function of the output current of the installed 24-united i-TE device by harvesting body heat. Reproduced with permission.^[160] Copyright 2022, Wiley-VCH.

7.2. Device Composition and High-Performance Electrode Materials

The necessary elements for i-TE devices include electrolyte, electrodes, and supporting substrates, as shown in **Figure 26a**. In addition, appropriate interconnection technology, contact

resistance optimization, device packaging, and wire collocation are also inescapable factors for high-performance i-TE devices.^[168c] Electrodes are one of the most prominent components where the accumulated ions will lay, attach, and deposit. Practically, the electrode behavior directly determines the maximum capacitance and the energy density. State-of-art

electrode materials have drawn intensive interest recently, such as carbon nanotubes, polymer composites, CNT forests, treated metals, and aerogels.^[12,70,84c,99,100,173] These promising electrodes are normally made with complicated microstructures to provide large specific surface areas for promoting ion accumulation.^[149,174]

As shown in Figure 26b, multiwalled carbon nanotubes (MWCNTs) were employed as the electrodes of a PVA/phosphoric acid (H₃PO₄) i-TE gel-based device with delicately designed electrode patterns.^[175] The MWCNT was predissolved as aqueous inks aided by sodium dodecylbenzenesulfonate surfactant, followed by deposited as patterned electrodes. After coating PVA/H₃PO₄ gel to bridge two patterned electrodes, a supercapacitor was successfully prepared, which achieved an energy density of 1.05 mW h cm⁻³. Figure 26c–e depicts CNT aerogel electrodes and the fabrication of the corresponding device.^[176] Aligned nanostructures (Figure 26c) can be obtained by the engineering method of continuous reeling off and wrapping CNT sheets (Figure 26d). The electrode optimization process involved removing low-activity carbon impurities, deposition of catalytic platinum nanoparticles, mechanical compressing to regulate porosity, and the gripping of the cylindrical device geometry. The obtained i-TE device (Figure 26e) can generate an output power density of 6.6 W m⁻² (ΔT = 51 °C), which is 3.95% of the Carnot efficiency. Moreover, the introduction of 3D hierarchical Au/Cu electrodes can greatly increase the electroactive surface area and lower the interface charge transfer resistance.^[160] As can be seen in Figure 26f, the double-layer metal electrode with microflower-like morphology contributes to a power density of 8.9 mW m⁻² K⁻², which is six times higher than that of 2D Au/Cu electrode devices. The developed 24-armed i-TE device harvests a remarkable output voltage of 2.8 V and output power of 68 μW at a ΔT of 10 °C (Figure 26g).

7.3. Device Types and Working Principle

i-TE capacitors based on thermodiffusion effect is the most common situation where the i-TE capacitor works barely following the Soret effect mechanisms. As shown in Figure 27a, the exact thermovoltage curve corresponds to the typical four-stage process discussed in Section 4.3. The potential raised from the thermodiffusive ion concentration difference (especially for the second stage in Figure 27a) can be estimated by the Nernst equation as^[98]

$$E_{\text{cell}} = E_{\text{cell}}^0 - \frac{RT}{nF} \ln \frac{c_{\text{hot}}}{c_{\text{cold}}} \quad (25)$$

where E_{cell} refers to the ion-diffusion derived potential difference (a single species of ion couple), E_{cell}^0 is the standard cell potential of the corresponding ion couple, c_{hot} and c_{cold} are the molar concentrations of the balanced ions at the surface of the hot and cold electrode, R , F , and n are the universal gas constant, Faraday constant, and the ionic charge, respectively. Moreover, we noticed that in this four-stage mode, the counter charge generated in stage III can be accumulated by repeatedly executing the step of heating–charging (stages I and

II). Since in stage I, the accumulated ions at the electrode surface are saturated mainly due to electrostatic repulsion. However in stage II, as the circuit is connected, the counter charges generated within the electrodes can neutralize the ionic charge at the electrode surface. Therefore, if the circuit is disconnected at this time and the ΔT is applied again, additional ions will migrate to the electrode surface and accumulate (a 2nd stage I). Then an expanded counter potential will be generated during the 2nd stage II via continue transporting electrons across the external circuit from the electrodes. This means that repeat operation of stages I and II can expand the capacitance before cooling in stage III. It is a viewpoint of our logical inference according to some analogous literature results which could develop inspirations for future experiments.^[18,92]

i-TE generators based on thermodiffusion effect is a simple two-stage process based on the thermodiffusion effect,^[51] as illustrated in Figure 27b. Different from e-TE generators, a prior voltage build-up step is required that consumes a certain time. When the external circuit is connected in the following power output step, a gradually decayed power supply occurs. This is principally analogous to stage II of the i-TE capacitor mode in Figure 27a. This type of generator is intermittent, and the resetting of the accumulated ions is demanded after every cycle. Practically, this generator mode is likely to be the capacitor mode in the condition of supplying power while charging (stages I and II).

i-TE capacitors based on thermogalvanic effect also conceive a four-stage process, as exhibited in Figure 27c.^[160,177] In stage I, the spontaneous oxidation/reduction reaction occurs initially at the hot end (taking the oxidation reaction as an example here). Therefore, electrons are continuously released to the hot electrode and accumulated to generate open-circuit thermovoltage. The reverse reaction (reduction here) will not take place at the cold electrode. In stage II, the accumulated electrons flow from the hot electrode to the cold electrode across the external circuit. As a result, the reduction reaction is motivated at the cold end, which continuously absorbs electrons. The hot-end electrons generated in stage I are thus circulated which triggers potential decay. It is noteworthy that the voltage will not decline to zero as a drain voltage generally maintains. Meanwhile, the oxidized ions gather nearby the hot electrode and the reduced ion clusters enrich around the cold electrode. In the following stage III, the external circuit is disconnected and the ΔT is removed. Besides, the redox couples remain localized surrounding the electrode because of the bulky dimension of ion clusters (such as Fe(CN)₆³⁻/Fe(CN)₆⁴⁻). As the cold electrode return to ambient temperature, a reverse oxidation reaction is triggered to transfer electrons to the cold electrode. An opposite open-circuit potential is formed gradually as depicted in Figure 27c. Finally, in stage IV, the device can be discharged by connecting to an external circuit. A reverse current generates in this period, which promotes the reverse reaction at the hot electrode surface. The redox couples return to the initial state.

i-TE generators based on thermogalvanic effect is no more than the combination of the above two modes, as shown in Figure 27d. The voltage build-up and power output process are equivalent to stages I and II of i-TE capacitors based on thermogalvanic effect. However, there is an

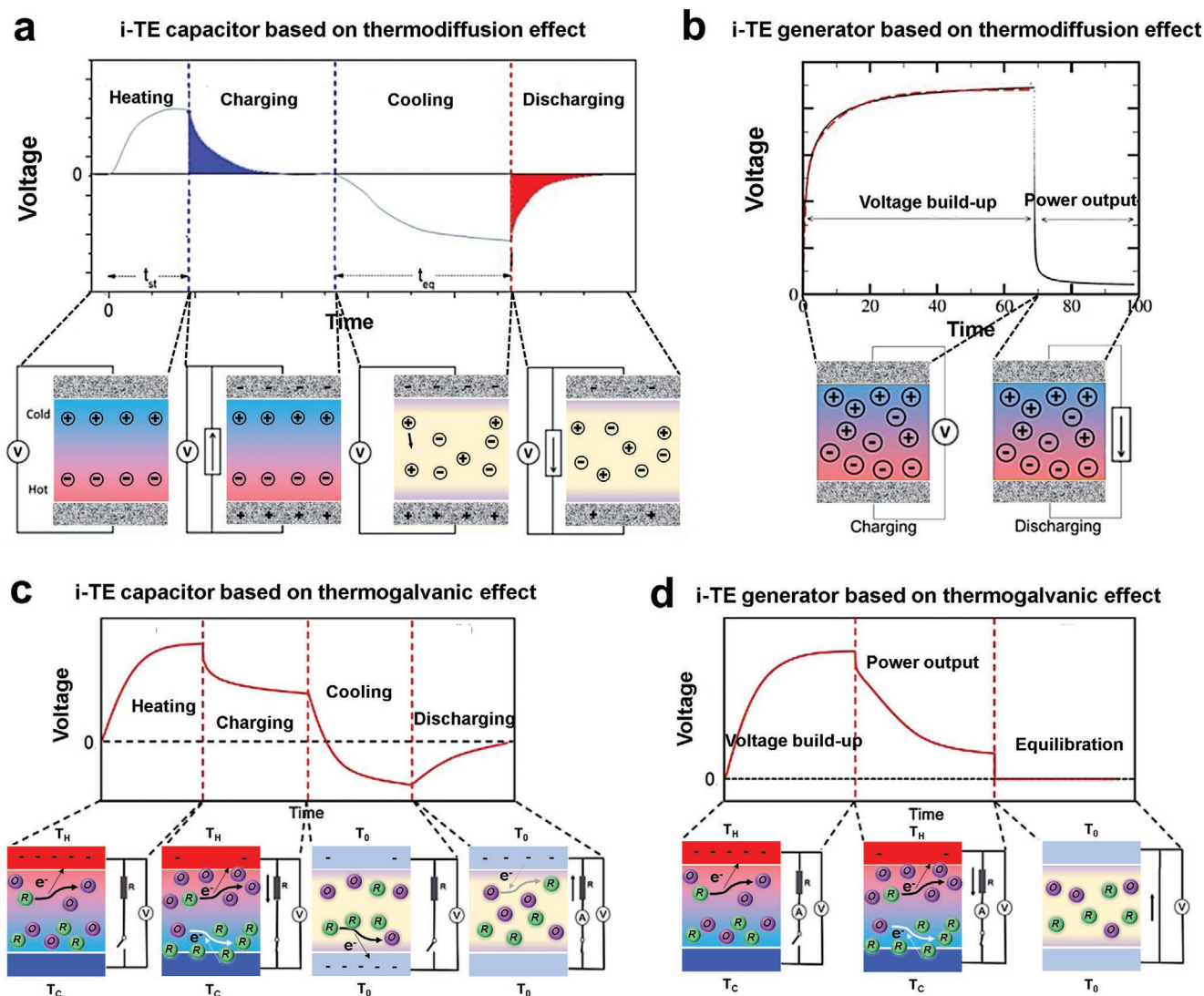


Figure 27. Voltage curve and mechanism of a) i-TE capacitors based on thermodiffusion effect, b) i-TE generators based on thermodiffusion effect, c) i-TE capacitors based on thermogalvanic effect, and d) i-TE generators based on thermogalvanic effect. Reproduced with permission.^[80] Copyright 2017, Wiley-VCH.

additional equilibration process where the external circuit is retained and the ΔT is revoked. The redox couples return to the initial state in this stage for repeat-cycle standby. This equals to a waiting step between power supply intervals, generators with rapid self-discharging will provide superior economic benefits.^[98]

7.4. Application of I-TE Capacitors

The i-TE devices are highly inadequate compared with traditional e-TE devices. At the same time, the specific device design theory has not been systematically established yet. Current mainstream fabrication strategies for i-TE devices are focused on the consulting of flexible e-TE devices. In the following three sections, we will provide several state-of-art examples of i-TE capacitors, generators, and sensors in order. **Figure 28a** dem-

onstrates an assembled thermobattery, with the top and bottom electrodes being polypyrrole (PPy)-coated graphite sheets, and inner layer being potassium ferricyanide/ferrocyanide $[K_3Fe(CN)_6/K_4Fe(CN)_6]$ aqueous, which showed an inherent S of around -1.4 mV K^{-1} .^[178] Composites of Cu foam/PEG1000 were filled into the bottom layer serving as the thermal storage and preservation module. As a result, the disturbing low-grade ΔT was exceptionally stabilized. An all-day electricity supply was achieved because of the heat reservation in the daytime. **Figure 28b** shows the working mechanisms in aspects of daytime heating (Model 1) and nighttime cooling (Model 2), respectively. In the daytime, sunlight heat was absorbed by the PPy broadband absorber layer via convection and conduction. Subsequently, the heat was absorbed by continued transferring down through the i-TE layer to the energy storage layer. This further cooled bottom electrode to yield a larger ΔT . While in the nighttime, the stored heat was released to build ΔT with

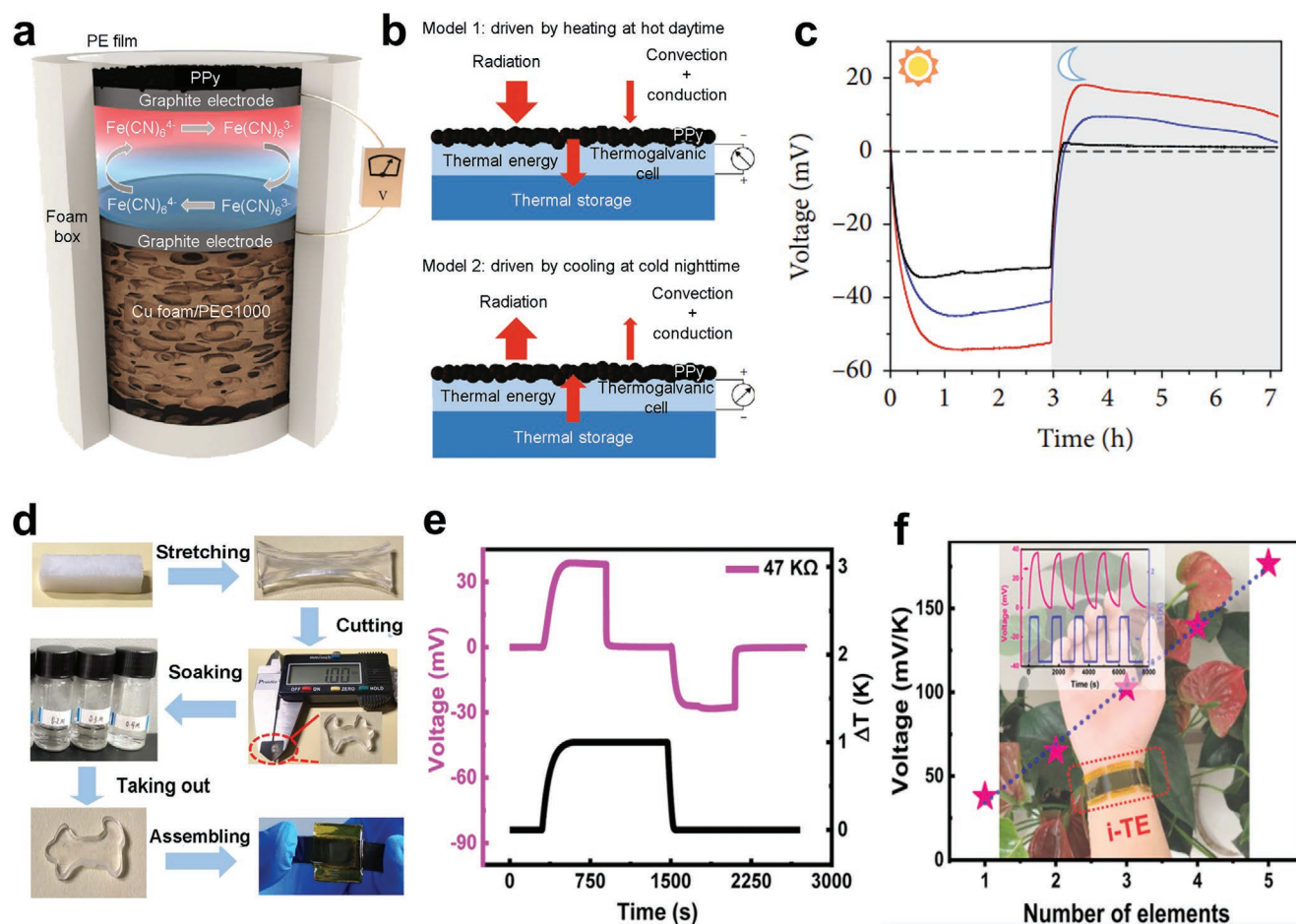


Figure 28. a) Schematic structure of the thermogalvanic i-TE battery designed for all-day energy supply. b) Working principle of the thermogalvanic i-TE battery where model 1 indicates the daytime energy flux and model 2 demonstrates the nighttime energy flux. c) The open-circuit voltage in an all-day long period, black curve for pristine graphite/[K₃Fe(CN)₆/K₄Fe(CN)₆] battery, blue curve for graphite/[K₃Fe(CN)₆/K₄Fe(CN)₆]/Cu foam/PEG1000 battery, red curve for PPy/graphite/[K₃Fe(CN)₆/K₄Fe(CN)₆]/Cu foam/PEG1000 battery. Reproduced with permission.^[178] Copyright 2019, American Association for the Advancement of Science. d) Fabrication process of the PVA/HCl hydrogel thermocapacitor unit. e) The four-stage voltage curve of the thermocapacitor with an external load of 47 kΩ. f) The open-circuit voltage of the tandem device with different i-TE elements where every element is cut into an identical dimension of 8 × 8 × 1 mm. Reproduced with permission.^[179] Copyright 2022, American Chemical Society.

an opposite sign, which sustainably powered the battery. As can be seen, the maximum device voltage reached −54.2 mV in the daytime and 18.2 mV in the nighttime (Figure 28c). The comparative experiment of innocent graphite/[K₃Fe(CN)₆/K₄Fe(CN)₆] thermobattery exhibited inferior daytime voltage of −34.1 mV and scarce nighttime voltage. Such a strategy indicates a proof-of-concept module to recycle TE conversion for all-day electricity furnishing.

As depicted in Figure 28d, a PVA/HCl hydrogel thermocapacitor was fabricated by the designed process, which introduced ion channels to optimize TE performance.^[179] In brief, the freeze-thawed PVA hydrogel was stretched repeatedly at room temperature to induce directed crystallization. Then the hydrogel was cut into the desired shape and soaked into the HCl solution along the stretching direction. After that, the PVA hydrogel was fully swollen with HCl filled in the gaps within aligned crystals, which was exactly the ion transport pattern. By installing and encapsulating the prepared i-TE hydrogel, a bracelet-like device was obtained. Figure 28e shows the voltage

curve of the i-TE device applying under the capacitor mode with an external load of 47 kΩ. Finally, this work achieved a superior *S* of 176.58 mV K^{−1} just employing five tandem pieces of 8 × 8 × 1 mm squared i-TE hydrogels (Figure 28f).

7.5. Application of I-TE Generators

Figure 29a shows a wearable i-TE generator fabricated through coating PEDOT:PSS/DMSO/[EMIM:DCA] (see Figure 29b) on fabrics.^[180] A continuous 8.78 μm ultrathin TE layer was formed on the surface of the cotton yarn, in contrast to the pristine PEDOT:PSS penetrated yarn which resulted in discontinuous structures. This is closely related to the higher viscosity and surface tension of the PEDOT:PSS/DMSO/[EMIM:DCA] composite solution. The yarn fibers were inaccessible to be wetted at the surface and penetrated the bulk. The surface-coated yarn showed significantly enhanced flexibility compared with pristine PEDOT:PSS. Besides, the maximum *S*² σ was optimized

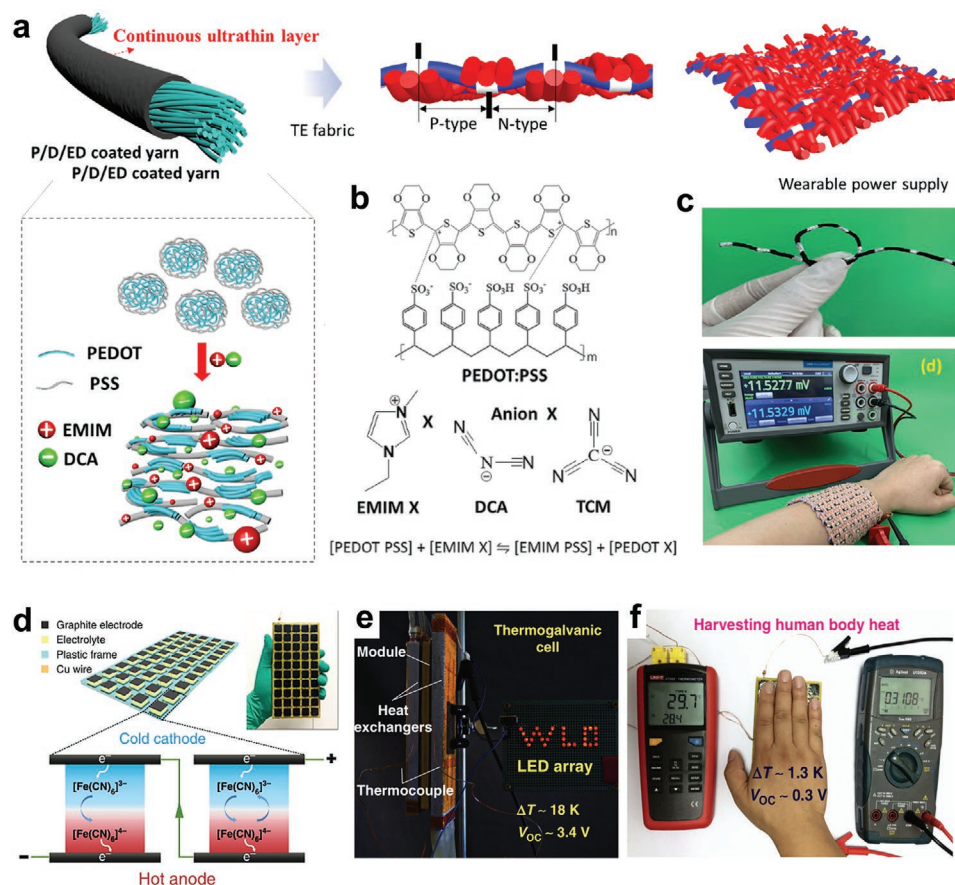


Figure 29. a) Schematic diagram of the fabrication and structure of the PEDOT:PSS/DMSO/[EMIM:DCA] (P/D/ED)-coated yarn. b) Chemical structures and interactions between PEDOT:PSS and [EMIM:DCA]. c) Photographs of the flexible P/D/ED-coated long yarn fabric and the voltage generated by the wrist TE wristband harvesting body heat. Reproduced with permission.^[180] Copyright 2021, American Chemical Society. d) Schematic diagram and photograph of the 50-unit integrated i-TE module. e) Photograph of the i-TE thermogenerator directly lights on an array of 29 red LED lamp beads (the module was sandwiched by two aluminum heat pipe exchangers with cold and hot water controlled at ≈ 278 and 333 K, respectively). f) Photograph of an i-TE generator attached to human body, with the temperature and open-circuit voltage were measured by a thermometer (left) and a multimeter (right), respectively. Reproduced with permission.^[34] Copyright 2018, Springer Nature.

to $24.7 \mu\text{W m}^{-1} \text{K}^{-2}$ in contrast to $0.00684 \mu\text{W m}^{-1} \text{K}^{-2}$ of pristine PEDOT:PSS. By preparing a 2 m long coated yarn as the weft yarn and pristine cotton yarn as the warp yarn, a flexible $15 \text{ cm} \times 6.5 \text{ cm}$ squired TE wrist containing 140 TE units was weaved (Figure 29c). The output power density reached 136.1 mW m^{-2} under a ΔT of 40.8 K . It is worth mentioning that although the addition of ILs induced PSS amount elimination, there are also ion/electron synergistic effects.^[181]

Another instance of i-TE generator can be referred to Figure 29d,e.^[34] The chaotropic cations guanidine chloride (GdmCl) and highly soluble urea enhanced $[\text{Fe}(\text{CN})_6]^{4-}/[\text{Fe}(\text{CN})_6]^{3-}$ electrolytes were employed to fabricate the i-TE material. A thermogalvanic i-TE module including 50 units was fabricated by utilizing a polyamide frame containing 50 holes with sizes of $10 \times 10 \times 5 \text{ mm}^3$ (Figure 29d). Then the prepared electrolyte was injected into the holes and sandwiched by two pieces of graphite electrodes. Finally, all these units were connected in series with Cu wires and sealed by epoxy resin glues. The as-assembled generator module was able to generate an open-circuit voltage of 3.4 V and a short-circuit current of 1.2 mA at a low-grade ΔT of 18 K . An LED array can be directly

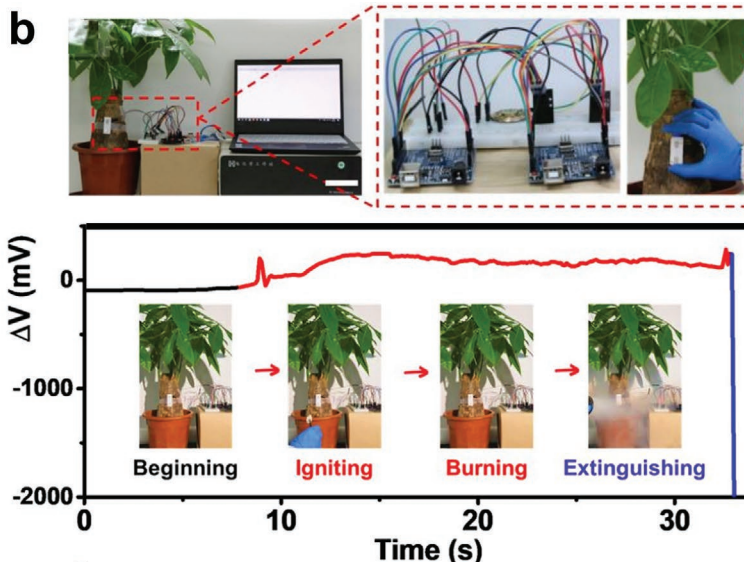
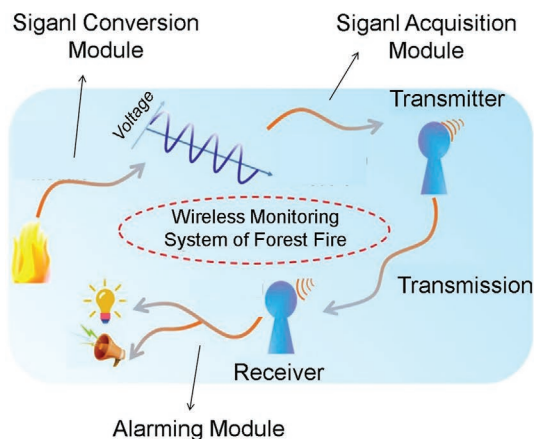
lighted on (Figure 29e). When harvesting heat from human skin, a practically considerable voltage over 0.3 V was stably transformed by a faint ΔT of 1.3 K , as shown in Figure 29f.

7.6. Application of I-TE Sensors

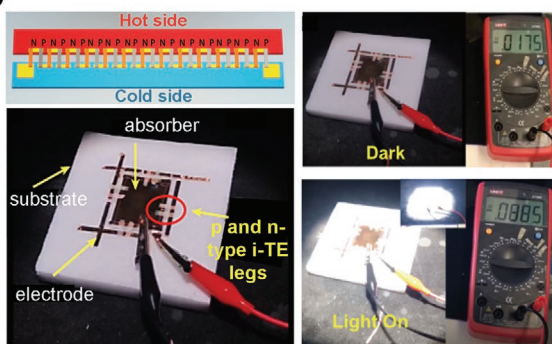
Traditional thermosensors such as thermopiles are composed of inorganic alloys based on the e-TE effect. However, there are still traits of insufficient thermovoltage, material brittleness, and large-scale production obstacles. These drawbacks of traditional TE sensors restrict the detection limits and sensitivities. Recently, i-TE devices have been proposed as TE detectors owing to the giant ionic S values, high flexibility, and scale-up feasibility.

Figure 30a,b illustrates a TE paper chip that is designed for remote alarming of early-stage forest fires.^[78] After collecting the signal of ΔT , the telecommunication signal is transferred through a loop of signal conversion module, signal acquisition module, transmitter, and receiver in sequence, as shown in Figure 30a. The whole system achieved signal transformation

a The fire monitoring system circuit



c



d

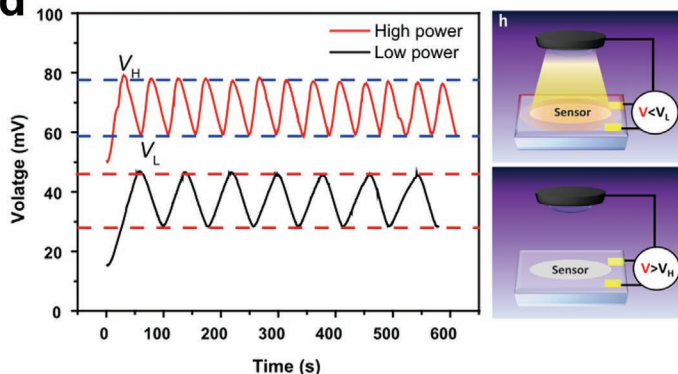


Figure 30. a) Schematic diagram of the communication system of the wireless remote fire alarm monitor. b) Images of the wireless remote fire alarm monitor and the offhand thermovoltage evolution in the process from the initial fire to the extinguishing. Reproduced with permission.^[78] Copyright 2020, American Chemical Society. c) Structure, composition, and real-time response of the i-TE thermal sensor. d) Thermovoltage performance of the light-induced thermal sensor with corresponding demonstrations of the automatic lamp controlling. Reproduced with permission.^[182] Copyright 2022, Springer Nature.

without relying on an additional power source, being low-cost ($\approx \$0.4$) and environment-friendly (paper matrix). As shown in Figure 30b, the TE paper chip can be bent freely into desirable shapes to fit the tree trunk. Once a burning fire source approached the trunk, ΔT would be established. Such a signal was grasped by the i-TE alarm module to generate a rapid sharp voltage signal. Upon the voltage reached the programmed threshold voltage, the alarming circuit was triggered with a flashing red LED. Simultaneously, the loudspeaker started broadcasting. At last, the fire was experimentally extinguished, which led to quieting of the voltage signal. This work makes a proof of concept that i-TE sensors can be applied for wireless real-time detections of abnormal temperature change.

Another interest i-TE research was reported where the light-derived heat change was monitored (Figure 30c,d).^[182] All-solid-state i-TE units of p-type PVDF-HFP/NaTFSI/propylene carbonate (PhNP) and n-type tris(pentafluorophenyl)borane incorporated PhNP (T-PhNP) were prepared. The S values were measured as $+20$ and -6 mV K⁻¹, respectively. A 13-leg p-n connected device generated a superior voltage of 2.6 V under a ΔT

of 10 K. In these regards, a self-powered 4-leg sensor was developed, which induced the lamp on/off by waved output voltages. By further connecting the sensor to a computer program, the automatic control of the lamp was achieved (Figure 30d). Specifically, during the light-on periods, the light-derived heat was absorbed to generate voltage. Once the voltage attained the upper stated limit, the light was automatically turned off via a designed electric circuit. Subsequently, the device surface was cooled down because the voltage drops accordingly. Once the voltage dropped to the lower stated limit, the light was automatically turned on. Presumably, the constant on-off cycle of the lamp appeared where higher lighting power promoted more rapid responses, as shown in Figure 30d. This will offer great promise in heat detection, power supply, gating elements.^[183]

8. Summary and Outlook

Last decade has witnessed the rapid development of i-TEs. Compared to traditional e-TE materials, the most significant

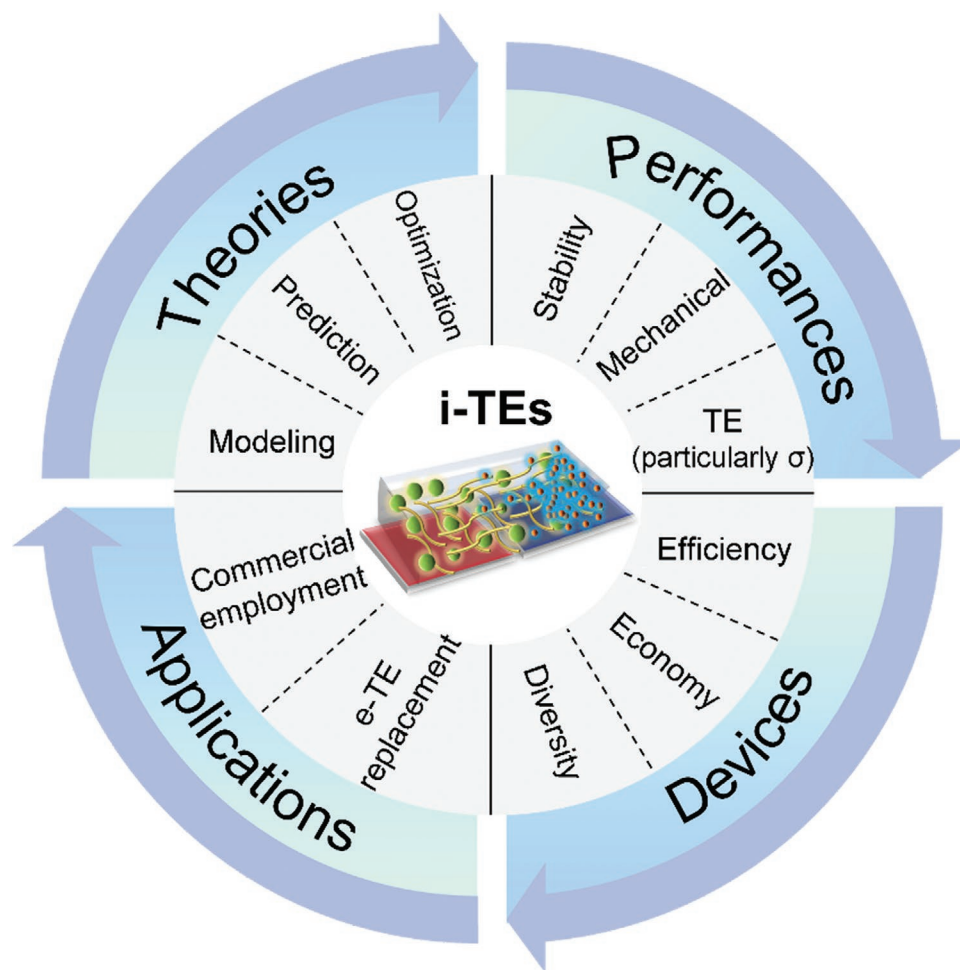


Figure 31. Prospects of i-TE technologies. Reproduced with permission.^[182] Copyright 2022, Springer Nature.

characteristic of i-TE materials is their ultrahigh S , which is highly desirable for collecting and cycling low-grade waste heat. I-TE materials are also flexible, economic, and eco-friendly. Compared with e-TE device, an additional thermal-powered capacitor mode is endowed in i-TE devices, which can be therefore used for continuously supplying energy in the condition of intermittent heat sources.

Despite of grand progresses, research on i-TEs is still in its infant stage, while in-depth understandings are still urgently required. Several main research gaps are hindering performance optimizations and practical applications. First, it is controversial to directly equate or compare i-TE parameters to e-TE parameters, which are derived from the electron/phonon transport characteristics in a single homogeneous material. In fact, i-TE effect is based on the accumulated ion concentration difference is determined by the whole system as well as the interaction between every single component. Second, i-TE materials are suffering from inferior σ because of the addition of nonconductive components. Besides, the dissociation and transfer of ions are also more time-consuming than electrons. The insufficient σ degrades the ultimate i-TE performance despite the ultrahigh S and normally low κ . Third, the i-TE performance is relatively unstable. On the one hand, ionic transport is sensitive

to the external environment, especially variation of temperature and humidity. On the other hand, the solvents will inevitably evaporate as time passed, which impedes long-term services. Although it can be minimized by replenishing hygroscopic agents or restricting the vapor pressures, the vaporization cannot be completely prevented. Last but not the least, there are risks of dissipation and leakage to the IL components in the process of device assembly and application. In terms of liquid state and quasi-solid state i-TE materials, the device fabrication engineering should consider encapsulation strategies.

In these regards, we summarize several prospects as below (Figure 31).

- i) Further shaping of i-TE theories. The exploration of novel TE materials is supported by appropriate theoretical guidance. However, the theoretical fundamentals of i-TE systems are completely different from e-TE fundamentals, which have been relatively maturely established. To predict the performance and design advanced i-TE systems, future research on i-TE theories is in urgent demand. The critical research directions include the digital modeling of the i-TE program, the logical prediction formula deduction, and the systematization of performance optimization philosophies.

- ii) Improvement of i-TE performances. Currently, high-performance i-TE materials are still under development. The promising designation targets involve the discovery of novel n-type and p-type i-TE systems, the balance between the TE and the mechanical behaviors (e.g., flexibility, self-healing ability, stretchability, etc.), and the enhancement of material stability. Herein, the improvement of σ values is the key point for optimizing TE behaviors. The combination of i-TE materials and other advanced TE components is another enlightenment that is an effective way to tap the performance potential.
- iii) Optimization of i-TE devices. Irrespective of serving as capacitors, generators, and sensors, high-efficiency of i-TE devices is prominent. Insightful understanding surrounding the high-efficient device, the large-scale feasibility, the low-cost material innovation, the creation of novel battery architecture, the material flitting for different application scenarios, and the organization of biocompatible/wearable human body electronics are needed. Additional efforts should be paid to companion research of the minimization of contact resistance and the fabrication/functional modification of electrode materials as well.
- iv) Extending practical applications. Unlike the commercialized e-TE materials, there have been technology gaps between experimental development and the practical application of i-TE systems. As the i-TE materials are lavish and interlock plenty of disciplines, the practical application of i-TE materials will also validate their prospects as a next-generation TE solution.

Acknowledgements

This work was financially supported by the Australian Research Council and HBIS-UQ Innovation Centre for Sustainable Steel project and QUT Capacity Building Professor Program.

Open access publishing facilitated by Queensland University of Technology, as part of the Wiley - Queensland University of Technology agreement via the Council of Australian University Librarians.

Conflict of Interest

The authors declare no conflict of interest.

Keywords

devices, ionic thermoelectrics, materials, thermo-electrochemical

Received: October 31, 2022
Revised: December 19, 2022
Published online: January 20, 2023

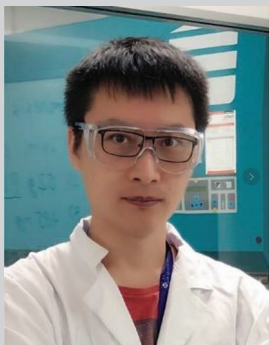
- [1] a) Y. Zhang, Q. Zeng, Y. Wu, J. Wu, S. Yuan, D. Tan, C. Hu, X. Wang, *Nano-Micro Lett.* **2020**, *12*, 175; b) S. Chu, A. Majumdar, *Nature* **2012**, *488*, 294.
- [2] a) X.-L. Shi, J. Zou, Z.-G. Chen, *Chem. Rev.* **2020**, *120*, 7399; b) J. M. Ding, W. R. Zhao, W. L. Jin, C.-A. Di, D. B. Zhu, *Adv. Funct. Mater.* **2021**, *31*, 2010695; c) X. Shi, L. Chen, *Nat. Mater.* **2016**, *15*, 691; d) Y. Xiao, L. D. Zhao, *Science* **2020**, *367*, 1196; e) D. Beretta, N. Neophytou, J. M. Hodges, M. G. Kanatzidis, D. Narducci, M. Martin-Gonzalez, M. Beekman, B. Balke, G. Cerretti, W. Tremel, A. Zevalkin, A. I. Hofmann, C. Müller, B. Döring, M. Campoy-Quiles, M. Caironi, *Mater. Sci. Eng., R* **2019**, *138*, 100501.
- [3] a) M. Bharti, A. Singh, S. Samanta, D. K. Aswal, *Prog. Mater. Sci.* **2018**, *93*, 270; b) S. Xu, X.-L. Shi, M. Dargusch, C. Di, J. Zou, Z.-G. Chen, *Prog. Mater. Sci.* **2021**, *121*, 100840; c) A. Mehdizadeh Dehkordi, M. Zebarjadi, J. He, T. M. Tritt, *Mater. Sci. Eng., R* **2015**, *97*, 1.
- [4] R. A. Kishore, A. Nozariasbmarz, B. Poudel, M. Sanghadasa, S. Priya, *Nat. Commun.* **2019**, *10*, 1765.
- [5] D. Beretta, A. Perego, G. Lanzani, M. Caironi, *Sustainable Energy Fuels* **2017**, *1*, 174.
- [6] a) G. Zuo, Z. Li, E. Wang, M. Kemerink, *Adv. Electron. Mater.* **2018**, *4*, 1700501; b) L. Yang, Z.-G. Chen, M. S. Dargusch, J. Zou, *Adv. Electron. Mater.* **2018**, *8*, 1701797.
- [7] R. Kita, P. Polyakov, S. Wiegand, *Macromolecules* **2007**, *40*, 1638.
- [8] S. Scott, T. Driesner, P. Weis, *Nat. Commun.* **2015**, *6*, 7837.
- [9] Z. Wang, S. Yun, H. Xu, C. Wang, Y. Zhang, J. Chen, B. Jia, *Biore-sour. Technol.* **2019**, *286*, 121394.
- [10] S. Zhang, C. Chen, Y. Zhou, Y. Qian, J. Ye, S. Xiong, Y. Zhao, X. Zhang, *ACS Appl. Mater. Interfaces* **2018**, *10*, 23048.
- [11] H. J. Tyrrell, D. A. Taylor, C. M. Williams, *Nature* **1956**, *177*, 668.
- [12] T. Li, X. Zhang, S. D. Lacey, R. Mi, X. Zhao, F. Jiang, J. Song, Z. Liu, G. Chen, J. Dai, Y. Yao, S. Das, R. Yang, R. M. Briber, L. Hu, *Nat. Mater.* **2019**, *18*, 608.
- [13] a) Y. Li, Y. Yang, X. Liu, Y. Yang, Y. Wu, L. Han, Q. Han, *Colloids Surf., A* **2022**, *648*, 129254; b) Y. Chen, C. Shi, J. Zhang, Y. Dai, Y. Su, B. Liao, M. Zhang, X. Tao, W. Zeng, *Energy Technol.* **2022**, *10*, 2200070.
- [14] H. Cheng, X. He, Z. Fan, J. Ouyang, *Adv. Energy Mater.* **2019**, *9*, 1901085.
- [15] T. J. Abraham, D. R. MacFarlane, J. M. Pringle, *Energy Environ. Sci.* **2013**, *6*, 2639.
- [16] S. L. Kim, J.-H. Hsu, C. Yu, *Org. Electron.* **2018**, *54*, 231.
- [17] H. Wang, J. H. Hsu, S. I. Yi, S. L. Kim, K. Choi, G. Yang, C. Yu, *Adv. Mater.* **2015**, *27*, 6855.
- [18] B. Kim, J. Na, H. Lim, Y. Kim, J. Kim, E. Kim, *Adv. Funct. Mater.* **2019**, *29*, 1807549.
- [19] Z. Liu, H. Cheng, H. He, J. Li, J. Ouyang, *Adv. Funct. Mater.* **2021**, *32*, 2109772.
- [20] X. He, H. Cheng, S. Yue, J. Ouyang, *J. Mater. Chem. A* **2020**, *8*, 10813.
- [21] C. G. Han, X. Qian, Q. Li, B. Deng, W. Liu, *Science* **2020**, *368*, 1091.
- [22] B. Kim, J. U. Hwang, E. Kim, *Energy Environ. Sci.* **2020**, *13*, 859.
- [23] a) M. Massetti, F. Jiao, A. J. Ferguson, D. Zhao, K. Wijeratne, A. Wurger, J. L. Blackburn, X. Crispin, S. Fabiano, *Chem. Rev.* **2021**, *121*, 12465; b) M. F. Dupont, D. R. MacFarlane, J. M. Pringle, *Chem. Commun.* **2017**, *53*, 6288; c) M. Li, M. Hong, M. Dargusch, J. Zou, Z.-G. Chen, *Trends Chem.* **2021**, *3*, 561.
- [24] Y. Jia, Q. Jiang, H. Sun, P. Liu, D. Hu, Y. Pei, W. Liu, X. Crispin, S. Fabiano, Y. Ma, Y. Cao, *Adv. Mater.* **2021**, *33*, 2102990.
- [25] J. Chipman, *J. Am. Chem. Soc.* **1926**, *48*, 2577.
- [26] X. Shi, J. He, *Science* **2021**, *371*, 343.
- [27] a) C. Soret, *Arch. Sci. Phys. Nat.* **1879**, *2*, 48; b) C. Ludwig, *Sitzber. Akad. Wiss. Wien, Math-naturw. Kl.* **1856**, *20*, 539.
- [28] E. Laux, S. Uhl, T. Journot, J. Brossard, L. Jeandupeux, H. Keppner, *J. Electron. Mater.* **2016**, *45*, 3383.
- [29] X. Wu, N. Gao, H. Jia, Y. Wang, *Chem. - Asian J.* **2021**, *16*, 129.
- [30] M. Li, L. Dai, Y. Hu, *ACS Energy Lett.* **2022**, *7*, 3204.
- [31] H. Zhu, C. Xiao, Y. Xie, *Adv. Mater.* **2018**, *30*, 1802000.
- [32] a) A. Al-zubaidi, X. Ji, J. Yu, *Sustainable Energy Fuels* **2017**, *1*, 1457; b) C. Cheng, Y. Dai, J. Yu, C. Liu, S. Wang, S. P. Feng, M. Ni, *Energy Fuels* **2021**, *35*, 161.
- [33] M. A. M. Hasan, H. Wu, Y. Yang, *J. Mater. Chem. A* **2021**, *9*, 19116.
- [34] J. Duan, G. Feng, B. Yu, J. Li, M. Chen, P. Yang, J. Feng, K. Liu, J. Zhou, *Nat. Commun.* **2018**, *9*, 5146.

- [35] T. Kim, J. S. Lee, G. Lee, H. Yoon, J. Yoon, T. J. Kang, Y. H. Kim, *Nano Energy* **2017**, *31*, 160.
- [36] a) A. Würger, *Phys. Rev. Lett.* **2008**, *101*, 108302; b) S. A. Putnam, D. G. Cahill, *Langmuir* **2005**, *21*, 5317; c) K. A. Esfahian, A. Majee, M. Maskos, A. Würger, *Soft Matter* **2014**, *10*, 1931; d) D. Vigolo, S. Buzzaccaro, R. Piazza, *Langmuir* **2010**, *26*, 7792; e) M. Reichl, M. Herzog, A. Götz, D. Braun, *Phys. Rev. Lett.* **2014**, *112*, 198101.
- [37] a) M. Eslamian, F. Sabzi, M. Z. Saghir, *Phys. Chem. Chem. Phys.* **2010**, *12*, 13835; b) A. Sosnowska, E. Laux, H. Keppner, T. Puzyn, M. Bobrowski, *J. Mol. Liq.* **2020**, *316*, 113871; c) W. Zhang, J. Zhang, X. Liu, H. Li, Y. Guo, C. Geng, Y. Tao, Q.-H. Yang, *Adv. Funct. Mater.* **2022**, *32*, 2201205; d) F. Chen, *Curr. Opin. Electrochem.* **2022**, *35*, 101086; e) A. Boruń, *J. Mol. Liq.* **2019**, *276*, 214; f) A. Kumar, V. P. Mohandas, V. R. K. S. Susarla, P. K. Ghosh, *J. Solution Chem.* **2004**, *33*, 995; g) K. Dong, X. Liu, H. Dong, X. Zhang, S. Zhang, *Chem. Rev.* **2017**, *117*, 6636; h) M. Meot-Ner, *Chem. Rev.* **2005**, *105*, 213.
- [38] a) L. Onsager, *Phys. Rev.* **1931**, *38*, 2265; b) L. Onsager, *Phys. Rev.* **1931**, *37*, 405.
- [39] J. N. Agar, J. C. R. Turner, *Proc. R. Soc. A* **1960**, *255*, 307.
- [40] A. Würger, *Phys. Rev. Res.* **2020**, *2*, 042030(R).
- [41] B. E. Conway, E. Ayranci, *J. Solution Chem.* **1999**, *28*, 163.
- [42] J. Meixner, S. R. De Groot, P. Mazur, North-Holland Publishing Company, Amsterdam **1962**.
- [43] A. Würger, *Rep. Prog. Phys.* **2010**, *73*, 126601.
- [44] E. D. Eastman, *J. Am. Chem. Soc.* **1926**, *48*, 1482.
- [45] M. Born, *Z. Phys.* **1920**, *1*, 45.
- [46] a) M. Bonetti, S. Nakamae, M. Roger, P. Guenoun, *J. Chem. Phys.* **2011**, *134*, 114513; b) E. D. Eastman, *J. Am. Chem. Soc.* **1928**, *50*, 283.
- [47] J. Y. Cho, Y. S. Lim, S. M. Choi, K. H. Kim, W. S. Seo, H. H. Park, *J. Electron. Mater.* **2011**, *40*, 1024.
- [48] Z. Lei, B. Chen, C. Li, H. Liu, *Chem. Rev.* **2008**, *108*, 1419.
- [49] J. N. Agar, C. Y. Mou, J. L. Lin, *J. Phys. Chem.* **1989**, *93*, 2079.
- [50] J. Morthomas, A. Würger, *Eur. Phys. J. E* **2008**, *27*, 425.
- [51] D. Zhao, A. Würger, X. Crispin, *J. Energy Chem.* **2021**, *61*, 88.
- [52] J. M. Rubi, S. Kjelstrup, *J. Phys. Chem. B* **2003**, *107*, 13471.
- [53] X. Qian, J. Shin, Y. Tu, J. H. Zhang, G. Chen, *Phys. Chem. Chem. Phys.* **2021**, *23*, 22501.
- [54] a) A. Campero, J. A. Díaz Ponce, *ACS Omega* **2020**, *5*, 12046; b) X. Ji, X. Liu, M. Li, S. Shao, J. Chang, J. Du, X. Ma, X. Feng, L. Zhu, X. Yu, W. Hu, *J. Chem. Educ.* **2021**, *98*, 3019.
- [55] a) Y. Matsubara, D. C. Grills, Y. Koide, *ACS Omega* **2016**, *1*, 1393; b) P. Zhang, Y. Zhao, X. Zhang, *Chem. Soc. Rev.* **2018**, *47*, 2921.
- [56] a) M. T. Agne, R. Hanus, G. J. Snyder, *Energy Environ. Sci.* **2018**, *11*, 609; b) R. Hanus, J. George, M. Wood, A. Bonkowski, Y. Cheng, D. L. Abernathy, M. E. Manley, G. Hautier, G. J. Snyder, R. P. Hermann, *Mater. Today Phys.* **2021**, *18*, 100344.
- [57] a) H. Liu, X. Shi, F. Xu, L. Zhang, W. Zhang, L. Chen, Q. Li, C. Uher, T. Day, G. J. Snyder, *Nat. Mater.* **2012**, *11*, 422; b) B. Li, H. Wang, Y. Kawakita, Q. Zhang, M. Feyngenson, H. L. Yu, D. Wu, K. Ohara, T. Kikuchi, K. Shibata, T. Yamada, X. K. Ning, Y. Chen, J. Q. He, D. Vaknin, R. Q. Wu, K. Nakajima, M. G. Kanatzidis, *Nat. Mater.* **2018**, *17*, 226.
- [58] E. S. Toberer, A. Zevalkink, G. J. Snyder, *J. Mater. Chem.* **2011**, *21*, 15843.
- [59] S. Lin, W. Li, Y. Pei, *Mater. Today* **2021**, *48*, 198.
- [60] a) T. Bernges, T. Böger, O. Maus, P. S. Till, M. T. Agne, W. G. Zeier, *ACS Mater. Lett.* **2022**, *4*, 2491; b) T. Bernges, R. Hanus, B. Wankmiller, K. Imasato, S. Lin, M. Ghidui, M. Gerlitz, M. Peterlechner, S. Graham, G. Hautier, Y. Pei, M. R. Hansen, G. Wilde, G. J. Snyder, J. George, M. T. Agne, W. G. Zeier, *Adv. Energy Mater.* **2022**, *12*, 2200717.
- [61] a) H. Zhou, Z.-Y. Ong, G. Zhang, Y.-W. Zhang, *Nanoscale* **2022**, *14*, 9209; b) J. T. Gaskins, G. Kotsonis, A. Giri, S. Ju, A. Rohskopf, Y. Wang, T. Bai, E. Sachet, C. T. Shelton, Z. Liu, Z. Cheng, B. M. Foley, S. Graham, T. Luo, A. Henry, M. S. Goorsky, J. Shiomi, J.-P. Maria, P. E. Hopkins, *Nano Lett.* **2018**, *18*, 7469.
- [62] a) G. Tan, S. Hao, R. Hanus, X. Zhang, S. Anand, T. P. Bailey, A. Rettie, X. Su, C. Uher, V. P. Dravid, *ACS Energy Lett.* **2018**, *3*, 705; b) R. Hanus, R. Gurunathan, L. Lindsay, M. T. Agne, J. Shi, S. Graham, G. Jeffrey Snyder, *Appl. Phys. Rev.* **2021**, *8*, 031311.
- [63] A. Würger, *Phys. Rev. Lett.* **2021**, *126*, 068001.
- [64] a) A. W. Omta, M. F. Kropman, S. Woutersen, H. J. Bakker, *J. Chem. Phys.* **2003**, *119*, 12457; b) Y. Marcus, *Pure Appl. Chem.* **2009**, *62*, 899.
- [65] D. Song, C. Chi, M. An, Y. Du, W. Ma, K. Wang, X. Zhang, *Cell Rep. Phys. Sci.* **2022**, *3*, 101018.
- [66] S.-M. Chen, H.-L. Gao, X.-H. Sun, Z.-Y. Ma, T. Ma, J. Xia, Y.-B. Zhu, R. Zhao, H.-B. Yao, H.-A. Wu, S.-H. Yu, *Matter* **2019**, *1*, 412.
- [67] J. Duan, B. Yu, K. Liu, J. Li, P. Yang, W. Xie, G. Xue, R. Liu, H. Wang, J. Zhou, *Nano Energy* **2019**, *57*, 473.
- [68] H. Jia, X. Tao, Y. Wang, *Adv. Electron. Mater.* **2016**, *2*, 1600136.
- [69] K. Liu, J. Lv, G. Fan, B. Wang, Z. Mao, X. Sui, X. Feng, *Adv. Funct. Mater.* **2021**, *32*, 2107105.
- [70] W. B. Chang, C. M. Evans, B. C. Popere, B. M. Russ, J. Liu, J. Newman, R. A. Segalman, *ACS Macro Lett.* **2016**, *5*, 94.
- [71] L. Li, W. D. Liu, Q. Liu, Z. G. Chen, *Adv. Funct. Mater.* **2022**, *32*, 2200548.
- [72] Y. Yu, J. Nassar, C. Xu, J. Min, W. Gao, *Sci. Rob.* **2020**, *5*, 7946.
- [73] Y. Wang, L. Yang, X.-L. Shi, X. Shi, L. Chen, M. S. Dargusch, J. Zou, Z.-G. Chen, *Adv. Mater.* **2019**, *31*, 1807916.
- [74] Y. Liu, H. Zhou, W. Zhou, S. Meng, C. Qi, Z. Liu, T. Kong, *Adv. Energy Mater.* **2021**, *11*, 2101329.
- [75] a) M. Anouti, J. Jacquemin, P. Porion, *J. Phys. Chem. B* **2012**, *116*, 4228; b) J. Vila, P. Ginés, E. Rilo, O. Cabeza, L. M. Varela, *Fluid Phase Equilib.* **2006**, *247*, 32.
- [76] E. Laux, L. Jeandupeux, S. Uhl, H. Keppner, P. Pérez López, P. Sanglard, E. Vanoli, R. Marti, *Mater. Today Phys.* **2019**, *8*, 672.
- [77] a) H. Cheng, Q. Le, Z. Liu, Q. Qian, Y. Zhao, J. Ouyang, *J. Mater. Chem. C* **2022**, *10*, 433; b) P. Pérez, S. Uhl, E. Laux, P. Sanglard, R. Marti, H. Keppner, E. Vanoli, *Mater. Today Phys.* **2018**, *5*, 10298.
- [78] X. Wu, N. Gao, X. Zheng, X. Tao, Y. He, Z. Liu, Y. Wang, *ACS Appl. Mater. Interfaces* **2020**, *12*, 27691.
- [79] a) E. N. Durmaz, S. Sahin, E. Virga, S. de Beer, L. C. P. M. de Smet, W. M. de Vos, *ACS Appl. Polym. Mater.* **2021**, *3*, 4347; b) B. Yang, G. Portale, *Colloid Polym. Sci.* **2021**, *299*, 465.
- [80] H. Wang, D. Zhao, Z. U. Khan, S. Puzinas, M. P. Jonsson, M. Berggren, X. Crispin, *Adv. Electron Mater.* **2017**, *3*, 1700013.
- [81] A. Sohn, C. Yu, *Mater. Today Phys.* **2021**, *19*, 100433.
- [82] a) A. Yang, F. Yan, *ACS Appl. Electron Mater.* **2021**, *3*, 53; b) A. Shukla, T. P. Kumar, *Isr. J. Chem.* **2020**, *61*, 120.
- [83] a) H. Zhou, T. Yamada, N. Kimizuka, *J. Am. Chem. Soc.* **2016**, *138*, 10502; b) J. H. Kim, Y. Han, G. Shin, J. G. Jeon, H. J. Kim, B. J. So, S. Yun, T. J. Kang, *ACS Appl. Energy Mater.* **2022**, *5*, 13053; c) Y. Liu, H. Wang, P. C. Sherrell, L. Liu, Y. Wang, J. Chen, *Adv. Sci.* **2021**, *8*, 2100669.
- [84] a) G. Wu, Y. Xue, L. Wang, X. Wang, G. Chen, *J. Mater. Chem. A* **2018**, *6*, 3376; b) T. J. Abraham, D. R. Macfarlane, J. M. Pringle, *Chem. Comm.* **2011**, *47*, 6260; c) P. Yang, K. Liu, Q. Chen, X. Mo, Y. Zhou, S. Li, G. Feng, J. Zhou, *Angew. Chem., Int. Ed.* **2016**, *55*, 12050; d) T. J. Kang, S. Fang, M. E. Kozlov, C. S. Haines, N. Li, Y. H. Kim, Y. Chen, R. H. Baughman, *Adv. Funct. Mater.* **2012**, *22*, 477; e) E. Nightingale, *Biochim. Biophys. Acta* **1959**, *63*, 566; f) Burrows, Brian, *J. Electrochem. Soc.* **1976**, *123*, 154.
- [85] A. J. deBethune, T. S. Licht, N. Swendeman, *J. Electrochem. Soc.* **1959**, *106*, 616.

- [86] R. Hu, B. A. Cola, N. Haram, J. N. Barisci, S. Lee, S. Stoughton, G. Wallace, C. Too, M. Thomas, A. Gestos, *Nano Lett.* **2010**, *10*, 838.
- [87] E. H. Anari, M. Romano, W. X. Teh, J. J. Black, E. Jiang, J. Chen, T. Q. To, J. Panchompoo, L. Aldous, *Chem. Commun.* **2016**, *52*, 745.
- [88] V. Zinovyeva, S. Nakamae, M. Bonetti, M. Roger, *ChemElectroChem* **2014**, *1*, 426.
- [89] T. Zhu, C. Jiang, M. Wang, C. Zhu, N. Zhao, J. Xu, *Adv. Funct. Mater.* **2021**, *31*, 2102433.
- [90] S. Kee, M. A. Haque, D. Corzo, H. N. Alshareef, D. Baran, *Adv. Funct. Mater.* **2019**, *29*, 1905426.
- [91] Y. Zhao, H. Cheng, Y. Li, J. Rao, S. Yue, Q. Le, Q. Qian, Z. Liu, J. Ouyang, *J. Mater. Chem. A* **2022**, *10*, 4222.
- [92] B. Chen, Q. Chen, S. Xiao, J. Feng, X. Zhang, T. Wang, *Sci. Adv.* **2021**, *7*, 7233.
- [93] F. Jiao, A. Naderi, D. Zhao, J. Schlueter, M. Shahi, J. Sundström, H. Granberg, J. Edberg, U. Ail, J. Brill, T. Lindström, M. Berggren, X. Crispin, *J. Mater. Chem. A* **2017**, *5*, 16883.
- [94] J. Xu, H. Wang, X. Du, X. Cheng, Z. Du, H. Wang, *ACS Appl. Mater. Interfaces* **2021**, *13*, 20427.
- [95] M. Dietzel, S. Hardt, *Phys. Rev. Lett.* **2016**, *116*, 225901.
- [96] J. Le Bideau, L. Viau, A. Vioux, *Chem. Soc. Rev.* **2011**, *40*, 907.
- [97] Y. He, Q. Zhang, H. Cheng, Y. Liu, Y. Shu, Y. Geng, Y. Zheng, B. Qin, Y. Zhou, S. Chen, J. Li, M. Li, G. O. Odunmbaku, C. Li, T. Shumilova, J. Ouyang, K. Sun, *J. Phys. Chem. Lett.* **2022**, *13*, 4621.
- [98] S. L. Kim, H. T. Lin, C. Yu, *Adv. Energy Mater.* **2016**, *6*, 1600546.
- [99] D. Zhao, A. Martinelli, A. Willfahrt, T. Fischer, D. Bernin, Z. U. Khan, M. Shahi, J. Brill, M. P. Jonsson, S. Fabiano, X. Crispin, *Nat. Commun.* **2019**, *10*, 1093.
- [100] S. L. Kim, J.-H. Hsu, C. Yu, *Nano Energy* **2018**, *48*, 582.
- [101] D. Zhao, H. Wang, Z. U. Khan, J. C. Chen, R. Gabrielsson, M. P. Jonsson, M. Berggren, X. Crispin, *Energy Environ. Sci.* **2016**, *9*, 1450.
- [102] Y. Fang, H. Cheng, H. He, S. Wang, J. Li, S. Yue, L. Zhang, Z. Du, J. Ouyang, *Adv. Funct. Mater.* **2020**, *30*, 2004699.
- [103] W. Zhao, T. Sun, Y. Zheng, Q. Zhang, A. Huang, L. Wang, W. Jiang, *Adv. Sci.* **2022**, *9*, 2201075.
- [104] Z. A. Akbar, J.-W. Jeon, S.-Y. Jang, *Energy Environ. Sci.* **2020**, *13*, 2915.
- [105] M. Jeong, J. Noh, M. Z. Islam, K. Kim, A. Sohn, W. Kim, C. Yu, *Adv. Funct. Mater.* **2021**, *31*, 2011016.
- [106] W. Gao, Z. Lei, W. Chen, Y. Chen, *ACS Nano* **2022**, *16*, 8347.
- [107] a) J. K. G. Dhont, S. Wiegand, S. Duhr, D. Braun, *Langmuir* **2007**, *23*, 1674; b) G. Qian, Z. Li, R. Huang, J. Chen, X. Yu, *Energy Rep.* **2021**, *7*, 4895.
- [108] M. Scholer, S. Matsukiyo, *Ann. Geophys.* **2004**, *22*, 2345.
- [109] a) X. Yang, C. Wang, R. Lu, Y. Shen, H. Zhao, J. Li, R. Li, L. Zhang, H. Chen, T. Zhang, X. Zheng, *Nano Energy* **2022**, *101*, 107553; b) Q. Zhang, Y. Sun, W. Xu, D. Zhu, *Adv. Mater.* **2014**, *26*, 6829.
- [110] S. Inceoglu, A. A. Rojas, D. Devaux, X. C. Chen, G. M. Stone, N. P. Balsara, *ACS Macro Lett.* **2014**, *3*, 510.
- [111] B.-A. Mei, O. Munteshari, J. Lau, B. Dunn, L. Pilon, *J. Phys. Chem. C* **2018**, *122*, 194.
- [112] H. Wang, U. Ail, R. Gabrielsson, M. Berggren, X. Crispin, *Adv. Energy Mater.* **2015**, *5*, 1500044.
- [113] a) S. Verma, B. Padha, S. Arya, *ACS Appl. Energy Mater.* **2022**, *5*, 9090; b) G. L. Grocke, B. X. Dong, A. D. Taggart, A. B. F. Martinson, J. Niklas, O. G. Poluektov, J. W. Strzalka, S. N. Patel, *ACS Polym. Au* **2022**, *2*, 275.
- [114] a) M. Sezen-Edmonds, A. M. Glauzell, W. B. Chang, R. A. Segalman, M. L. Chabiny, Y.-L. Loo, *J. Phys. Chem. C* **2021**, *125*, 12289; b) M. Chen, Y. Wang, W. Ma, Y. Huang, Z. Zhao, *ACS Appl. Mater. Interfaces* **2020**, *12*, 28510; c) I. H. Sajid, N. Aslfattahi, M. F. Mohd Sabri, S. M. Said, R. Saidur, M. F. Mohd Salleh, N. N. Nik Ghazali, S. W. Hasan, *Electrochim. Acta* **2019**, *320*, 134575.
- [115] a) A. Sheskin, T. Schwarz, Y. Yu, S. Zhang, L. Abdellaoui, B. Gault, O. Cojocaru-Mirédin, C. Scheu, D. Raabe, M. Wuttig, Y. Amouyal, ACS Appl. Mater. Interfaces **2018**, *10*, 38994; b) M. R. Burton, C. A. Boyle, T. Liu, J. McGettrick, I. Nandhakumar, O. Fenwick, M. J. Carnie, *ACS Appl. Mater. Interfaces* **2020**, *12*, 28232.
- [116] W. Zhao, J. Ding, Y. Zou, C. A. Di, D. Zhu, *Chem. Soc. Rev.* **2020**, *49*, 7210.
- [117] a) N. Mateeva, H. Niculescu, J. Schlenoff, L. R. Testardi, *J. Appl. Phys.* **1998**, *83*, 3111; b) C. Wood, *Rep. Prog. Phys.* **1988**, *51*, 459.
- [118] a) S. Fleischmann, J. B. Mitchell, R. Wang, C. Zhan, D.-e. Jiang, V. Presser, V. Augustyn, *Chem. Rev.* **2020**, *120*, 6738; b) H. Mahon, D. O'Connor, D. Friedrich, B. Hughes, *Energy* **2022**, *239*, 122207; c) P. Rohland, E. Schröter, O. Nolte, G. R. Newkome, M. D. Hager, U. S. Schubert, *Prog. Polym. Sci.* **2022**, *125*, 101474; d) W. Zhang, P. Feng, J. Chen, Z. Sun, B. Zhao, *Prog. Polym. Sci.* **2019**, *88*, 220; e) J. Wei, L. Zhu, *Prog. Polym. Sci.* **2020**, *106*, 101254.
- [119] A. Härtel, M. Janssen, D. Weingarth, V. Presser, R. van Rooij, *Energy Environ. Sci.* **2015**, *8*, 2396.
- [120] a) C. S. Kim, H. M. Yang, J. Lee, G. S. Lee, H. Choi, Y. J. Kim, S. H. Lim, S. H. Cho, B. J. Cho, *ACS Energy Lett.* **2018**, *3*, 501; b) M. N. Hasan, N. Nayan, M. Nafea, A. G. A. Muthalif, M. S. Mohamed Ali, *Energy* **2022**, *259*, 125032; c) G. Prunet, F. Pawula, G. Fleury, E. Cloutet, A. J. Robinson, G. Hadziioannou, A. Pakdel, *Mater. Today Phys.* **2021**, *18*, 100402.
- [121] a) W. Gao, Z. Lei, C. Zhang, X. Liu, Y. Chen, *Adv. Funct. Mater.* **2021**, *31*, 2104071; b) J. Chen, C. Shi, L. Wu, Y. Deng, Y. Wang, L. Zhang, Q. Zhang, F. Peng, X.-M. Tao, M. Zhang, W. Zeng, *ACS Appl. Mater. Interfaces* **2022**, *14*, 34714; c) V. Arumugam, M. Naresh, R. Sanjeevi, *J. Biosci.* **1994**, *19*, 307; d) A. Chortos, Z. Bao, *Mater. Today* **2014**, *17*, 321.
- [122] a) N. Tanaka, *Polymer* **1978**, *19*, 770; b) D. Cangialosi, A. Alegría, J. Colmenero, *Prog. Polym. Sci.* **2016**, *54–55*, 128; c) M. Philipp, C. Nies, M. Ostermeyer, W. Possart, J. K. Krüger, *Soft Matter* **2018**, *14*, 3601.
- [123] a) D. Ji, T. Li, W. Hu, H. Fuchs, *Adv. Mater.* **2019**, *31*, 1806070; b) M. Ibanez, Z. Luo, A. Genc, L. Piveteau, S. Ortega, D. Cadavid, O. Dobrozhan, Y. Liu, M. Nachttegaal, M. Zebajadi, J. Arbiol, M. V. Kovalenko, A. Cabot, *Nat. Commun.* **2016**, *7*, 10766.
- [124] Z. Lei, W. Gao, P. Wu, *Joule* **2021**, *5*, 2211.
- [125] a) J. Li, C. Dong, J. Hu, J. Liu, Y. Liu, *ACS Appl. Electron. Mater.* **2021**, *3*, 3641; b) H. Sadeghi, S. Sangtarash, C. J. Lambert, *Nano Lett.* **2015**, *15*, 7467; c) M. Zeng, D. Zavanelli, J. Chen, M. Saeidi-Javash, Y. Du, S. LeBlanc, G. J. Snyder, Y. Zhang, *Chem. Soc. Rev.* **2022**, *51*, 485.
- [126] a) Z. Li, Y. Lu, Q. Su, M. Wu, X. Que, H. Liu, *ACS Appl. Mater. Interfaces* **2022**, *14*, 5402; b) L. Zhang, K. Jia, J. Wang, J. Zhao, J. Tang, J. Hu, *Mater. Horiz.* **2022**, *9*, 1911; c) Z. Yu, P. Wu, *Mater. Horiz.* **2021**, *8*, 2057.
- [127] a) F. Ni, P. Xiao, C. Zhang, W. Zhou, D. Liu, S. W. Kuo, T. Chen, *Adv. Mater.* **2021**, *33*, 2103937; b) J. Mo, Y. Dai, C. Zhang, Y. Zhou, W. Li, Y. Song, C. Wu, Z. Wang, *Mater. Horiz.* **2021**, *8*, 3409; c) Q. Pang, H. Hu, H. Zhang, B. Qiao, L. Ma, *ACS Appl. Mater. Interfaces* **2022**, *14*, 26536.
- [128] D. Gan, T. Shuai, X. Wang, Z. Huang, F. Ren, L. Fang, K. Wang, C. Xie, X. Lu, *Nanomicro Lett.* **2020**, *12*, 169.
- [129] a) R. Freer, A. V. Powell, *J. Mater. Chem. C* **2020**, *8*, 441; b) W. Shi, D. Wang, Z. Shuai, *Adv. Electron. Mater.* **2019**, *5*, 1800882; c) J. Yang, H.-L. Yip, A. K.-Y. Jen, *Adv. Energy Mater.* **2013**, *3*, 549.
- [130] a) Z. Huang, Y. Zhang, H. Wu, S. J. Pennycook, L.-D. Zhao, *ACS Appl. Energy Mater.* **2019**, *2*, 8236; b) J. Zeng, X. He, S.-J. Liang, E. Liu, Y. Sun, C. Pan, Y. Wang, T. Cao, X. Liu, C. Wang, L. Zhang, S. Yan, G. Su, Z. Wang, K. Watanabe, T. Taniguchi, D. J. Singh, L. Zhang, F. Miao, *Nano Lett.* **2018**, *18*, 7538.

- [131] X. Guan, H. Cheng, J. Ouyang, *J. Mater. Chem. A* **2018**, *6*, 19347.
- [132] I. H. Sajid, M. F. M. Sabri, S. M. Said, M. F. M. Salleh, N. N. N. Ghazali, R. Saidur, B. Subramaniam, S. W. Hasan, H. A. Jaffery, *Energy Convers. Manage.* **2019**, *198*, 111813.
- [133] E. Helfand, J. G. Kirkwood, *J. Chem. Phys.* **1960**, *32*, 857.
- [134] a) R. Kroon, D. A. Mengistie, D. Kiefer, J. Hynynen, J. D. Ryan, L. Yu, C. Müller, *Chem. Soc. Rev.* **2016**, *45*, 6147; b) Y. Yang, H. Deng, Q. Fu, *Mater. Chem. Front.* **2020**, *4*, 3130.
- [135] a) S. Kim, M. M. Mench, *J. Electrochem. Soc.* **2009**, *156*, B353; b) M. Tasaka, T. Mizuta, O. Sekiguchi, *J. Membr. Sci.* **1990**, *54*, 191; c) J. P. G. Villaluenga, B. Seoane, V. M. Barragán, C. Ruiz-Bauzá, *J. Membr. Sci.* **2006**, *274*, 116.
- [136] H. Kim, S. Yang, S. R. Rao, S. Narayanan, E. A. Kapustin, H. Furukawa, A. S. Umans, U. M. Yaghi, E. N. Wang, *Science* **2017**, *358*, 430.
- [137] a) B. G. Sumpter, D. W. Noid, M. D. Barnes, *Polymer* **2003**, *44*, 4389; b) J. Yang, H. Zhang, Q. Zhou, H. Qu, T. Dong, M. Zhang, B. Tang, J. Zhang, G. Cui, *ACS Appl. Mater. Interfaces* **2019**, *11*, 17109; c) T. Gaillard, M. George, E. Gastaldi, F. Nallet, P. Fabre, *Soft Matter* **2019**, *15*, 8302.
- [138] a) Z. Li, J.-F. Dong, F.-H. Sun, S. Hirono, J.-F. Li, *Chem. Mater.* **2017**, *29*, 7378; b) P.-A. Zong, J. Liang, P. Zhang, C. Wan, Y. Wang, K. Koumoto, *ACS Appl. Energy Mater.* **2020**, *3*, 2224; c) X. Jiang, J. Hoffman, C. C. Stoumpos, M. G. Kanatzidis, E. Harel, *ACS Energy Lett.* **2019**, *4*, 1741.
- [139] C. Huang, X. Qian, R. Yang, *Mater. Sci. Eng., R* **2018**, *132*, 1.
- [140] a) Q. Long, J. Xin, S. Li, A. Basit, S. Li, A. Luo, T. Xu, B. Xiao, J. Yang, Q. Jiang, X. Han, *ACS Appl. Energy Mater.* **2019**, *2*, 7490; b) S. Li, Z. Huang, W. Zhao, J. Luo, Y. Xiao, F. Pan, R. Wang, *ACS Appl. Mater. Interfaces* **2021**, *13*, 51018; c) D. Tan, J. Zhao, C. Gao, H. Wang, G. Chen, D. Shi, *ACS Appl. Mater. Interfaces* **2017**, *9*, 21820; d) Y. Zheng, T. J. Slade, L. Hu, X. Y. Tan, Y. Luo, Z.-Z. Luo, J. Xu, Q. Yan, M. G. Kanatzidis, *Chem. Soc. Rev.* **2021**, *50*, 9022.
- [141] W. D. Liu, L. Yang, Z. G. Chen, J. Zou, *Adv. Mater.* **2020**, *32*, 1905703.
- [142] a) C. Liu, D.-L. Shan, Z.-H. Shen, G.-K. Ren, W. Yue, Z.-F. Zhou, J.-Y. Li, D. Yi, J.-L. Lan, L.-Q. Chen, G. J. Snyder, Y.-H. Lin, C.-W. Nan, *Nano Energy* **2021**, *89*, 106380; b) Y. Sargolzaeiaval, V. Padmanabhan Ramesh, T. V. Neumann, V. Misra, D. Vashae, M. D. Dickey, M. C. Öztürk, *Appl. Energy* **2020**, *262*, 114370; c) S. J. Kim, J. H. We, B. J. Cho, *Energy Environ. Sci.* **2014**, *7*, 1959; d) V. Padmanabhan Ramesh, Y. Sargolzaeiaval, T. Neumann, V. Misra, D. Vashae, M. D. Dickey, M. C. Öztürk, *npj Flexible Electron.* **2021**, *5*, 5.
- [143] S. Horike, Q. Wei, K. Kirihara, M. Mukaida, T. Sasaki, Y. Koshiba, T. Fukushima, K. Ishida, *ACS Appl. Mater. Interfaces* **2020**, *12*, 43674.
- [144] a) X. Yang, G. Zhou, W.-Y. Wong, *Chem. Soc. Rev.* **2015**, *44*, 8484; b) A. X. Wu, J. A. Drayton, K. M. Rodriguez, Q. Qian, S. Lin, Z. P. Smith, *Macromolecules* **2020**, *53*, 5085.
- [145] a) R. Wang, L. Mu, Y. Bao, H. Lin, T. Ji, Y. Shi, J. Zhu, W. Wu, *Adv. Mater.* **2020**, *32*, 2002878; b) K. K. Kiran, M. Ravi, Y. Pavani, S. Bhavani, A. K. Sharma, V. V. R. Narasimha Rao, *J. Non-Cryst. Solids* **2012**, *358*, 3205.
- [146] a) W. Zhou, Q. Fan, Q. Zhang, L. Cai, K. Li, X. Gu, F. Yang, N. Zhang, Y. Wang, H. Liu, *Nat. Commun.* **2017**, *8*, 14886; b) Y. Wang, M. Hong, W. Liu, X. L. Shi, Z. G. Chen, *Chem. Eng. J.* **2020**, *397*, 125360; c) Z. Fan, P. Li, D. Du, J. Ouyang, *Adv. Energy Mater.* **2017**, *7*, 1602116.
- [147] a) H. Yan, N. Sada, N. Tushima, *J. Therm. Anal. Calorim.* **2002**, *69*, 881; b) L. Wang, Q. Yao, H. Bi, F. Huang, Q. Wang, L. Chen, *J. Mater. Chem. A* **2014**, *2*, 11107.
- [148] K. Choi, S. L. Kim, S. I. Yi, J. H. Hsu, C. Yu, *ACS Appl. Mater. Interfaces* **2018**, *10*, 23891.
- [149] H. Im, H. G. Moon, J. S. Lee, I. Y. Chung, T. J. Kang, Y. H. Kim, *Nano Res.* **2014**, *7*, 443.
- [150] H. B. Callen, *Phys. Rev.* **1948**, *73*, 1349.
- [151] K. Chen, L. Yao, B. Su, *J. Am. Chem. Soc.* **2019**, *141*, 8608.
- [152] a) Y. Saito, S. Takeda, S. Yamagami, J. Nakadate, T. Sasaki, T. Cho, *J. Phys. Chem. C* **2018**, *122*, 18311; b) Y. Saito, *Membranes* **2021**, *11*, 277.
- [153] T. Moriyasu, T. Sakamoto, N. Sugihara, Y. Sasa, Y. Ota, T. Shimomura, Y. Sakai, K. Ito, *Polymer* **2013**, *54*, 1490.
- [154] I. E. Jacobs, E. W. Aasen, J. L. Oliveira, T. N. Fonseca, J. D. Roehling, J. Li, G. Zhang, M. P. Augustine, M. Mascal, A. J. Moulé, *J. Mater. Chem. C* **2016**, *4*, 3454.
- [155] a) H. Yuk, B. Lu, S. Lin, K. Qu, J. Xu, J. Luo, X. Zhao, *Nat. Commun.* **2020**, *11*, 1604; b) S. Xu, M. Hong, X.-L. Shi, Y. Wang, L. Ge, Y. Bai, L. Wang, M. Dargusch, J. Zou, Z.-G. Chen, *Chem. Mater.* **2019**, *31*, 5238; c) M. Pichumani, P. Bagheri, K. M. Poduska, W. González-Viñas, A. Yethiraj, *Soft Matter* **2013**, *9*, 3220.
- [156] a) J. Wu, G. Xia, S. Li, L. Wang, J. Ma, *Ind. Eng. Chem. Res.* **2020**, *59*, 22509; b) S. Guo, K. Zhao, Z. Feng, Y. Hou, H. Li, J. Zhao, Y. Tian, H. Song, *Appl. Surf. Sci.* **2018**, *455*, 599.
- [157] a) F. Schüth, *Chem. Mater.* **2014**, *26*, 423; b) M. Giannouli, V. M. Drakonakis, A. Savva, P. Eleftheriou, G. Florides, S. A. Choulis, *ChemPhysChem* **2015**, *16*, 1134.
- [158] a) F. Ahangaran, A. H. Navarchian, F. Picchioni, *J. Appl. Polym. Sci.* **2019**, *136*, 48039; b) S. Karumuri, S. Hiziroglu, A. K. Kalkan, *ACS Appl. Mater. Interfaces* **2015**, *7*, 6596; c) J. Zhu, X. Wang, X. Wang, Y. Lei, Y. Li, *Compos. Sci. Technol.* **2021**, *214*, 108960; d) K. Zhu, Y. Yu, Y. Cheng, C. Tian, G. Zhao, Y. Zhao, *ACS Appl. Mater. Interfaces* **2019**, *11*, 4826; e) M. Darbandi, W. Lu, J. Fang, T. Nann, *Langmuir* **2006**, *22*, 4371.
- [159] a) D. Tian, Y. Song, L. Jiang, *Chem. Soc. Rev.* **2013**, *42*, 5184; b) H. Yuk, X. Zhao, *Adv. Mater.* **2018**, *30*, 1704028.
- [160] Y. Li, Q. Li, X. Zhang, B. Deng, C. Han, W. Liu, *Adv. Energy Mater.* **2022**, *12*, 2103666.
- [161] a) M. A. Johnson, J. Iyer, P. T. Hammond, *Macromolecules* **2004**, *37*, 2490; b) T. J. Trivedi, D. N. Srivastava, R. D. Rogers, A. Kumar, *Green Chem.* **2012**, *14*, 2831; c) F. Bode, M. A. da Silva, P. Smith, C. D. Lorenz, S. McCullen, M. M. Stevens, C. A. Dreiss, *Soft Matter* **2013**, *9*, 6986.
- [162] Z. Li, G. Ma, R. Ge, F. Qin, X. Dong, W. Meng, T. Liu, J. Tong, F. Jiang, Y. Zhou, K. Li, X. Min, K. Huo, Y. Zhou, *Angew. Chem., Int. Ed.* **2016**, *55*, 979.
- [163] Y. Son, A. Liao, R. L. Peterson, *J. Mater. Chem. C* **2017**, *5*, 8071.
- [164] V. Chernikova, O. Shekhah, M. Eddaoudi, *ACS Appl. Mater. Interfaces* **2016**, *8*, 20459.
- [165] a) Y. Huang, I. Szeleifer, N. A. Peppas, *Macromolecules* **2002**, *35*, 1373; b) T. Yamakado, S. Saito, *J. Am. Chem. Soc.* **2022**, *144*, 2804.
- [166] Y. Tan, Z.-B. Shao, X.-F. Chen, J.-W. Long, L. Chen, Y.-Z. Wang, *ACS Appl. Mater. Interfaces* **2015**, *7*, 17919.
- [167] a) Y. P. Neo, C. O. Perera, M. K. Nieuwoudt, Z. Zujovic, J. Jin, S. Ray, M. Gizdavic-Nikolaidis, *J. Agric. Food Chem.* **2014**, *62*, 5163; b) M. Yang, S. Li, S. Zhang, B. Gao, Z. Tong, D. Cheng, D. Chen, R. Huang, Y. Yang, *J. Mater. Chem. A* **2022**, *10*, 18834; c) K. Li, T. Ping, H. Zhang, J. Zhang, J. Cheng, F. Gao, *RSC Adv.* **2021**, *11*, 3740.
- [168] a) J. S. Teixeira, R. S. Costa, A. L. Pires, A. M. Pereira, C. Pereira, *Dalton Trans.* **2021**, *50*, 9983; b) Z. Wu, S. Zhang, Z. Liu, E. Mu, Z. Hu, *Nano Energy* **2022**, *91*, 106692; c) T. Cao, X.-L. Shi, Z.-G. Chen, *Prog. Mater. Sci.* **2023**, *131*, 101003.
- [169] R. Lin, H. J. Kim, S. Achavananthadith, S. A. Kurt, S. C. C. Tan, H. Yao, B. C. K. Tee, J. K. W. Lee, J. S. Ho, *Nat. Commun.* **2020**, *11*, 444; b) S. Mannsfeld, B. Tee, R. Stoltenberg, C. Chen, S. Barman, B. Muir, A. Sokolov, C. Reese, Z. Bao, *Nat. Mater.* **2010**, *9*, 859; c) J. Huang, J. Zhou, Y. Luo, G. Yan, H. Duan, *ACS Appl.*

- Mater. Interfaces* **2020**, *12*, 43009; d) C. Zhang, J. Chen, W. Xuan, S. Huang, B. You, W. Li, L. Sun, H. Jin, X. Wang, S. Dong, *Nat. Commun.* **2020**, *11*, 58.
- [170] a) H. Huang, L. Tao, F. Liu, L. Ji, Y. Hu, M. C. Cheng, P. Y. Chen, D. Akinwande, *Microsyst. Technol.* **2016**, *2*, 9; b) A. Aslam, U. Mehmood, M. H. Arshad, A. Ishfaq, M. Sufyan, *Sol. Energy* **2020**, *207*, 874; c) A. Saleem, H. Najam, J. Ju, L. Kyung-Geun, *Sensors* **2016**, *16*, 460; d) T. C. Huang, Y. G. Leu, C. W. Huang, *Energy* **2017**, *133*, 879.
- [171] a) J. Wu, J. J. Black, L. Aldous, *Electrochim. Acta* **2017**, *225*, 482; b) L. Zhang, T. Kim, N. Li, T. J. Kang, J. Chen, J. M. Pringle, M. Zhang, A. H. Kazim, S. Fang, C. Haines, D. Al-Masri, B. A. Cola, J. M. Razal, J. Di, S. Beirne, D. R. MacFarlane, A. Gonzalez-Martin, S. Mathew, Y. H. Kim, G. Wallace, R. H. Baughman, *Adv. Mater.* **2017**, *29*, 1605652.
- [172] R. Liu, Z. L. Wang, K. Fukuda, T. Someya, *Nat. Rev. Mater.* **2022**, *7*, 870.
- [173] A. M. Abdul Mageeth, S. Park, M. Jeong, W. Kim, C. Yu, *Appl. Energy* **2020**, *268*, 114975.
- [174] G. Li, D. Dong, G. Hong, L. Yan, X. Zhang, W. Song, *Adv. Mater.* **2019**, *31*, 1901403.
- [175] A. L. Pires, R. S. Costa, C. Pereira, A. M. Pereira, *ACS Appl. Electron. Mater.* **2021**, *3*, 696.
- [176] H. Im, T. Kim, H. Song, J. Choi, J. S. Park, R. Ovalle-Robles, H. D. Yang, K. D. Kihm, R. H. Baughman, H. H. Lee, T. J. Kang, Y. H. Kim, *Nat. Commun.* **2016**, *7*, 10600.
- [177] A. Kundu, T. S. Fisher, *Electrochim. Acta* **2018**, *281*, 357.
- [178] B. Yu, J. Duan, J. Li, W. Xie, H. Jin, R. Liu, H. Wang, L. Huang, B. Hu, J. Zhou, *Research* **2019**, *1*, 2460953.
- [179] Q. Chen, B. Chen, S. Xiao, J. Feng, J. Yang, Q. Yue, X. Zhang, T. Wang, *ACS Appl. Mater. Interfaces* **2022**, *14*, 19304.
- [180] M. Li, F. Zeng, M. Luo, X. Qing, W. Wang, Y. Lu, W. Zhong, L. Yang, Q. Liu, Y. Wang, J. Luo, D. Wang, *ACS Appl. Mater. Interfaces* **2021**, *13*, 50430.
- [181] M. Du, X. Chen, K. Zhang, *ACS Appl. Energy Mater.* **2021**, *4*, 4070.
- [182] C. Chi, M. An, X. Qi, Y. Li, R. Zhang, G. Liu, C. Lin, H. Huang, H. Dang, B. Demir, Y. Wang, W. Ma, B. Huang, X. Zhang, *Nat. Commun.* **2022**, *13*, 221.
- [183] E. Miyako, H. Nagata, R. Funahashi, K. Hirano, T. Hirotsu, *ChemSusChem* **2009**, *2*, 419.



Xiao-Lei Shi is currently a Research Fellow at Queensland University of Technology. He received his Ph.D. degree in 2019 from the University of Queensland under the supervision of Prof. Zhi-Gang Chen with a research focus on the development of high-performance thermoelectrics and underlying physics and chemistry.



Zhi-Gang Chen is currently a Capacity Building Professor of Energy Materials in Queensland University of Technology (QUT). He received his Ph.D. in materials science and engineering from the Institute of Metal Research, Chinese Academy of Science, in 2008. His research concentrates on smart functional materials for thermoelectrics and nanoelectronics from synthesizing materials to understanding their underlying physics and chemistry.